UNIVERSITY OF CALIFORNIA,
IRVINE

Modeling the Field Population of Cold Dark Matter Halos for Lensing Studies

DISSERTATION

submitted in partial satisfaction of the requirements
for the degree of

DOCTOR OF PHILOSOPHY

in Physics

by

Alexander Andres Lazar

Dissertation Committee:
Professor James S. Bullock, Chair
Professor Manoj Kaplinghat
Professor Michael Cooper

2023

DEDICATION

To my parents David and Pamela Lazar, for their never-ending love and support.

TABLE OF CONTENTS

LIST OF FIGURES

LIST OF TABLES

Page

ACKNOWLEDGMENTS

First and foremost, I would like to first acknowledge my thesis advisor, Dr. James S. Bullock. James S. Bullock directed and supervised research which forms the basis for the dissertation. Believe it or not, I was not accepted to any another institution's Ph.D. program (including UCI) during the application cycle in 2018 based on how I looked on paper (test scores, GPA, etc.). Thankfully, Dr. Michael Boylan-Kolchin reached out during that time to James to consider me as a potential candidate, to which James happily accepted me into his group and into the Doctorate program, regardless of my apparent shortcomings. I would not have wanted anyone else to be my doctoral advisor, as James saw great potential in me as a scientist; he provided enormous support during my tenure as an astrophysicist, seeded excitement and wonder in exploring new scientific endeavours, and also hosted outstanding computational facilities to operate with. James, thank you for everything.

Moreover, I express my thanks to Dr. Michael Boylan-Kolchin, who was my research advisor during my undergraduate studies at the University of Texas at Austin (UT). As a new faculty within the Astronomy department, I couldn't imagine what was going through your head when you saw some young man reaching out to look for research experience when just transferring out of community college. Thank for taking that risk and providing the necessary fundamentals to succeed as a scientist.

I also want to thank Dr. Leonidas Moustakas for hosting me as my technical advisor during my time at JPL. You facilitated scientific wonder there while also provided excellent cat care advise for my mischievous kitten.

Graduate school has proven to be the several best years of my life. This is all thanks to my friends I have grown so close with and became so fond of in my astronomy cohort on the second floor of FRH. I learned to nerd out on the most obscure and niche topics, increased my drinking tolerance to ten-folds compared to undergrad, and I have most likely met the love of my life during my time here.

The content within Chapter 2 of this dissertation is a reprint of the material as it appears in the Monthly Notices of the Royal Astronomical Society,Volume 502, Issue 4, April 2021, Pages 6064–6079, doi.org:10.1093/mnras/stab448, used with permission from Oxford Academic. The co-authors listed in this publication are James Bullock, Michael Boylan-Kolchin, Robert Feldmann, Onur Catmabacak, and Leonidas Moustakas.

The content within Chapter 3 of this dissertation is a reprint of the material submitted to the Monthly Notices of the Royal Astronomical Society and is currently under review. The co-authors listed in this publication are James Bullock, Anna Nierenberg, Michael Boylan-Kolchin, and Leonidas Moustakas.

This work has been supported by the MUREP NASA Graduate Research Fellowship Program; Grant 80NSSSC20K1469. Additional support came from the NSF grant AST-1910965. Analysis of simulation data was primarily performed on the *Green Planet* computing cluster at the University

of California, Irvine.

The analysis in this dissertation, while also done on pen and paper, made extensive use of the python packages COLOSSUS (Diemer 2018), NumPy (van der Walt et al. 2011), SciPy (Oliphant 2007), and Matplotlib (Oliphant 2007). I am thankful to the developers of these tools. This research has made all intensive use of NASA's Astrophysics Data System (http://ui.adsabs.harvard.edu/) and the arXiv eprint service (http://arxiv.org).

VITA

Alexander Andres Lazar

EDUCATION

Doctor of Philosophy in Physics — **2023**
University of California, Irvine — *Irvine, California*

Master of Science in Physics — **2021**
University of California, Irvine — *Irvine, California*

Bachelor of Science in Physics — **2018**
University of Texas, Austin — *Austin, Texas*

Bachelor of Science in Astronomy — **2018**
University of Texas, Austin — *Austin, Texas*

RESEARCH EXPERIENCE

NASA Research Fellow — **2020–2023**
NASA Jet Propulsion Laboratory (JPL) — *Pasadena, California*

Graduate Research Assistant — **2018–2023**
University of California, Irvine — *Irvine, California*

TEACHING EXPERIENCE

Teaching Assistant — **2018–2019**
University of California, Irvine — *Irvine, California*

REFEREED JOURNAL PUBLICATIONS

Probing the initial mass function of the first stars with transients **2022**
Monthly Notices Royal Astronomical Society

Galaxies lacking dark matter produced by close encounters in a cosmological simulation **2022**
Nature Astronomy

Out of sight, out of mind? The impact of correlated clustering in substructure lensing **2021**
Monthly Notices Royal Astronomical Society

The time-scales probed by star formation rate indicators for realistic, bursty star formation histories from the FIRE simulations **2021**
Monthly Notices Royal Astronomical Society

A dark matter profile to model diverse feedback-induced core sizes of ΛCDM haloes **2020**
Monthly Notices Royal Astronomical Society

Accurate mass estimates from the proper motions of dispersion-supported galaxies **2020**
Monthly Notices Royal Astronomical Society

Dark and luminous satellites of LMC-mass galaxies in the FIRE simulations **2019**
Monthly Notices Royal Astronomical Society

ABSTRACT OF THE DISSERTATION

Modeling the Field Population of Cold Dark Matter Halos for Lensing Studies

By

Alexander Andres Lazar

Doctor of Philosophy in Physics

University of California, Irvine, 2023

Professor James S. Bullock, Chair

The Universe's mass is predominately comprised of dark matter, yet its exact particle nature remain elusive. The dark energy (Λ) plus Cold Dark Matter (ΛCDM) model of cosmology reigns as the prevalent model of our Universe, as it matches the observed large-scale structure. The formation mechanism of these so-called dark matter halos introduces many possible particle candidates for CDM models and further manifests attributes in the global abundance and the underlying mass distribution. Precise detection of these objects in the low-mass regime could further pave way to revealing the particle nature of dark matter. An exciting route to reveal the existence of dark matter structures within our Universe that have mass scales smaller than the faintest galaxies (i.e., Ultra-faint Dwarfs) is based on their lingering presence on strong gravitational lensed systems.

The contents within this thesis provides, for the first time, in depth analysis of crucial lensing quantities derived from numerical simulations of dark matter halos and galaxies within the ΛCDM paradigm. Importantly, we explore models pertaining to the "line-of-sight" (LOS; i.e., field) perturbers, as these are one of most contributing population of dark matter halos to significantly impact the lensing signal, as compared to the subhalo population. We demonstrate that clustering in the vicinity of the lens host halo is an important component in any lensing configuration, as it produces a clear enhancement to the lensing signal relative to an assumption of unclustered halos with substructure. We also introduce an analytical surface density profile for low-mass dark

matter halos that are parameterized by the so-called "projected concentration", making it useful for modeling LOS perturbers in strong gravitational lensing models. Finally, we then extend this surface density model using a statistical sample of simulated dark matter halos to infer the median evolution of the projected concentration and the scatter as a function of mass.

The framework developed here inevitably broadens the scope of strong-lensing analyses for probing dark matter in a ΛCDM universe, thus demonstrating the power of strong gravitational lensing as a unique probe of dark matter physics.

Chapter 1

Preliminaries

1.1 Historical context

The standard cosmological paradigm — ΛCDM (dark energy + cold dark matter) model — is the apotheosis of physics characterizing the formation of structure within the framework of Einastien's Theory of General Relativity (Blumenthal et al. 1984). What is more is that this framework is a culmination of a century of work that marriages the fields of particle physics and astrophysics from the past several decades; analysis through microlensing has ruled out dark matter to not be large compact objects, e.g. black holes, but instead some new particle that is yet to be detected (e.g., Tisserand et al. 2007). In the current picture of the standard model of cosmology, cold (non-relativist) dark matter particles, as the Universe evolves, lump together into gravitationally bound halos, which then go on to host the galaxies that we know of today (White and Rees 1978, Blumenthal et al. 1984). However, little evidence on the very nature of dark matter is known, only that that it interacts gravitationally with the fundamental particles found in the Standard Model of Particle Physics and is entirely decoupled to the electromagnetic spectrum (see Bertone and Tait 2018, for overview).

The era of the *Hubble Space Telescope* (*HST*) has been revolutionary in our understanding of the Universe we reside in and has provided beautiful, resolved images of astrophysical objects. One such peculiar *HST* image showed multiple copies of one extremely luminous source at various positions on the sky. It turned out that the gravitational field of a galaxy, mostly surround by dark matter, was perfectly aligned between Earth and a extremely bright quasar named WFI 2033-4723 (Morgan et al. 2004, Eigenbrod et al. 2006, Vuissoz et al. 2008). The gravitational field generated by the galaxy was so extreme, that it warped space-time surrounding it and bent the geodesic of the photons emitted from the luminous quasar. This phenomenon is strictly referred to as *strong gravitational lensing*.

If the prevalent ΛCDM model is in fact correct, then the Universe should be inhabited by countless gravitationally-bound structures, i.e. *dark matter halos*, and should produce a significant gravitational lensing effect to lens images via *substructure lensing*. If these objects are detected through lensing, ΛCDM would undoubtedly reign as the standard model of cosmology. If not detected, then alternative cosmological models would hold greater merit, e.g. Warm Dark Matter (WDM), as halos do not exist below a certain mass scale, which in tandem is dependent on the attributes of the dark matter particle. Any false or positive detection would ultimately improve our understanding of the Universe and might solve a long-standing problem in modern astrophysics. Our current knowledge regarding the nature of dark matter is that it only gravitationally interacts with the fundamental particles found in the Standard Model. Efforts in detecting dark matter non-gravitationally, via dark matter particle production from collisions, have not found success in producing results of how dark matter behaves (Bertone and Tait 2018). While direct and indirect detection methods has held some grounds of probing dark matter, *gravitational studies could be the only proven method of measuring the properties of dark matter*.

The following sections within this introductory chapter provides the reader the necessary background context for the remaining contents of this dissertation, which discusses my developments, implementations, and predictive aspects of substructure lensing using cosmological N-body simu-

lations with only dark matter and full galaxy formation physics. In the next sections, a primer on structure formation within the Universe (particularly in ΛCDM) is discussed, as well as what aspects of structure formation strong gravitational lensing can constrain and the formalism connecting lensing observables to dark matter halo populations.

1.2 Dark matter halos

Here we briefly discuss dark matter halos in the context of ΛCDM. A more thorough review is provided in Bullock and Boylan-Kolchin (2017), but enough content is presented here to provide further context to the main body of the dissertation. Herein and so forth, unless otherwise specified, lower case r denotes the physical, (de-projected) three-dimensional radius. In two-dimensions, the projected physical radius is denoted by an upper case R. The specific radii used to define a halo mass will usually be denoted by capital R with some over-density definition.

1.2.1 Structure formation

A more detailed discussion of structure formation can be found in Mo et al. (2010), but this section will provide a brief, yet necessary, context for dark matter halos, starting from the beginning. Cosmic structure is initialized by the primordial (and adiabatic) quantum fluctuations in the infant stages of the Universe and is encoded within the shape of the (scale-free) primordial power spectrum as a function of wave number k. Thereafter, these fluctuations grow by gravitational instability in an ever expanding background. The primordial power spectrum, as well as the growth of density fluctuations that were seeded during the early Universe, are influenced by the particle nature of dark matter and therefore, leave clues to be deduced by the resulting structure on both large- and small-scales. Scales of k during the epoch of radiation domination in the ΛCDM model grow relatively slowly until the epoch of matter domination, where the primordial power spectrum

becomes scale dependent. The transfer function encodes this suppression and is typically defined as the ratio between the amplitude of density perturbations between the era of post-recombination and the value of the primordial amplitude (e.g., Eisenstein and Hu 1998). Combining this machinery gives the linear power spectrum, which for ΛCDM, spans to scales that predict the mass cutoff at $M \sim 10^{-6}\, M_{\odot}$ for typical 100 GeV WIMP candidates (Green et al. 2004).[1] The Universe will eventually evolve to a point where scales become non-linear, which provide the regions that enable the collapse of virialized objects.

1.2.2 Global properties

By the time the over-dense regions of the Universe evolve to become non-linear, the regions stop expanding, they turn around, and collapse under their own gravity, converting potential energy into kinetic energy via the virial theorem. Dark matter halos are defined to be these spherical over-densities with mass, M_{Δ}, contained within a radius, R_{Δ}, that encloses some density contrast, Δ, relative to a reference background density at a particular redshift, $\rho_{\rm ref}(z)$, such that the interior density for the halo is $\rho_{\Delta} := \Delta\, \rho_{\rm ref}(z)$, i.e.,

$$M_{\Delta} = \frac{4\pi}{3} R_{\Delta}^3 \rho_{\Delta}(z)\,. \tag{1.1}$$

$\rho_{\rm ref}(z)$ can be set as the critical density of the universe or the mean matter density of the universe. Similarly, the *virial velocity* is

$$V_{\Delta} := \sqrt{\frac{G M_{\Delta}}{R_{\Delta}}}\,. \tag{1.2}$$

The parameters M_{Δ}, R_{Δ}, and V_{Δ} are equivalent mass labels, such that any one of these values determines the other two values, given a specified overdensity parameter Δ. Their are other more

[1] WIMPs stands for Weakly Interacting Massive Particles and are a CDM particle candidate, though not the only candidate (see Bertone and Tait 2018)

meaningful ways of modeling the mass of dark matter halos, such as the maximum circular velocity definition, $V_{\rm max}$ and equivalently $r_{\rm max}$, or such as the "splashback-radius" introduced by (More et al. 2015). For this dissertation we will solely use the overdensity definition in parameterizing dark matter halos in ΛCDM.[2]

The value for Δ is chosen to match the overdensity that predicts the virialized dark matter region that has undergone an idealized spherical collapse (Bryan and Norman 1998). Throughout this dissertation, we primarily define the dark matter halos by their virial mass, $M_{\rm vir}$, which are spherical systems with virial radius, $R_{\rm vir}$, inside of which the average density is equal to the virial density, $\rho_{\rm vir}(z)$, i.e.,

$$M_{\rm vir} = \frac{4\pi}{3} R_{\rm vir}^3 \, \rho_{\rm vir}(z) \, . \tag{1.3}$$

Here, the virial density is redshift evolving and is defined from Bryan and Norman (1998):

$$\rho_{\rm vir}(z) = \left(18\pi^2 + 82\xi - 39\xi^2\right) \, \rho_{\rm c}(z) \, , \tag{1.4}$$

where

$$\rho_{\rm c}(z) = \frac{3H^2(z)}{8\pi G} \tag{1.5}$$

is the critical density of the universe at redshift z. The evolving Hubble factor at redshift z is

$$H(z) = 100\, h \, \sqrt{\Omega_{\rm m}(1+z)^3 + \Omega_\Lambda} \, {\rm km\, s^{-1}\, Mpc^{-1}} \tag{1.6}$$

[2]Note that this overdensity mass are how dark matter halos *in the field*, i.e., isolated halos that are not located within a much larger halo, are defined. Subhalos, on the other hand, cannot be defined this way, as they experience tidal forces from orbiting the potential well of their host halo, which renders an a defined outer radius (dependent on a background reference density) ill defined. Subhalos are not the focus of this dissertation and their precise mass definition is beyond the scope.

with h being the cosmological Hubble factor, and $\xi := \widetilde{\Omega}_{\rm m}(z) - 1$, such that

$$\widetilde{\Omega}_{\rm m}(z) := \frac{\Omega_{\rm m}(1+z)^3}{\Omega_{\rm m}(1+z)^3 + \Omega_\Lambda} \,. \tag{1.7}$$

The Bryan and Norman (1998) definition is used for the most halo finding software and is one of the most commonly adopted definition of the halo mass within the literature. Dark matter halos can also be simply defined with a constant overdensity $\Delta = 200$ with either critical or mean-matter background densities. Other halo mass definitions can be explored with two other commonly adopted overdensity definitions, first being the critical density of the universe as a background reference, i.e.,

$$M_{\rm 200c} = \frac{4\pi}{3} R^3_{\rm 200c}\, \rho_{\rm 200c}(z) \,, \tag{1.8}$$

where $\rho_{\rm 200c}(z) := 200 \times \rho_{\rm c}(z)$, and a second based on the mean matter density of the universe, i.e.,

$$M_{\rm 200m} = \frac{4\pi}{3} R^3_{\rm 200m}\, \rho_{\rm 200m}(z) \,, \tag{1.9}$$

where $\rho_{\rm 200m}(z) := 200 \times \rho_{\rm m}(z)$, such that the mean matter density field is defined to evolve as

$$\rho_{\rm m}(z) = \Omega_{\rm m} \times \rho_{\rm c}(z=0)\,(1+z)^3 \,. \tag{1.10}$$

A benefit of the halo mass defined by Equation 1.8 is that it less dependent on the underlying cosmology, at least compared to the favored Bryan and Norman (1998) definition, whereas the halo mass defined with an evolving mean matter density, i.e., Equation 1.9, corresponds more closely to the so-called "splashback" boundary of the halo (e.g., Diemer and Kravtsov 2014, More et al. 2015). Note that the precise choice of the mass definition usually does not matter as long as one definition is consistent with the definition of halo mass throughout an analysis; Counting statistics is mainly preserved, as every halo has the same center, but the outer radius (i.e., the mass contained

within that radius) changes depending on the definition chosen.

1.2.3 Abundance

How do these spherically-overdense objects populate the universe? Remarkably, the mass spectrum of dark matter halos can be modeled with a few simple assumptions. It was first assumed that the mass spectrum of collapsed objects could be calculated by extrapolating the overdensity field using linear theory, even out into the highly non-linear regime, and utilizing a spherical collapse model. First prostulated by Press and Schechter (1974), the abundance of dark matter halos per unit mass, M, per unit volume, V, at redshift z, i.e., the dark matter *halo mass function*:

$$n(M, z) \simeq \frac{\mathrm{d}n}{\mathrm{d}\log_{10} M}\,, \tag{1.11}$$

depends only on the root-mean-square (rms) amplitude of the linear dark matter power spectrum, smoothed using a filter function (e.g., spherical top-hat) in real space and then extrapolated to redshift z using linear theory.

Furthermore, this model has been improved more rigorously in recent years within the literature (e.g., Sheth and Tormen 2002, Tinker et al. 2008). This accuracy has been tested thoroughly using numerical simulations with large-scale structure in ΛCDM. Figure 1.1 demonstrates this by comparing simulated mass functions at different redshifts (colored curves) with comparable analytical predictions via Sheth and Tormen (2002) (black-dashed curves). A key aspect on what this dissertation tackles is how low-mass halos $M_{\rm halo} < 10^8\,M_\odot$ are predicted to be highly abundant within the ΛCDM paradigm for a lensing configuration.

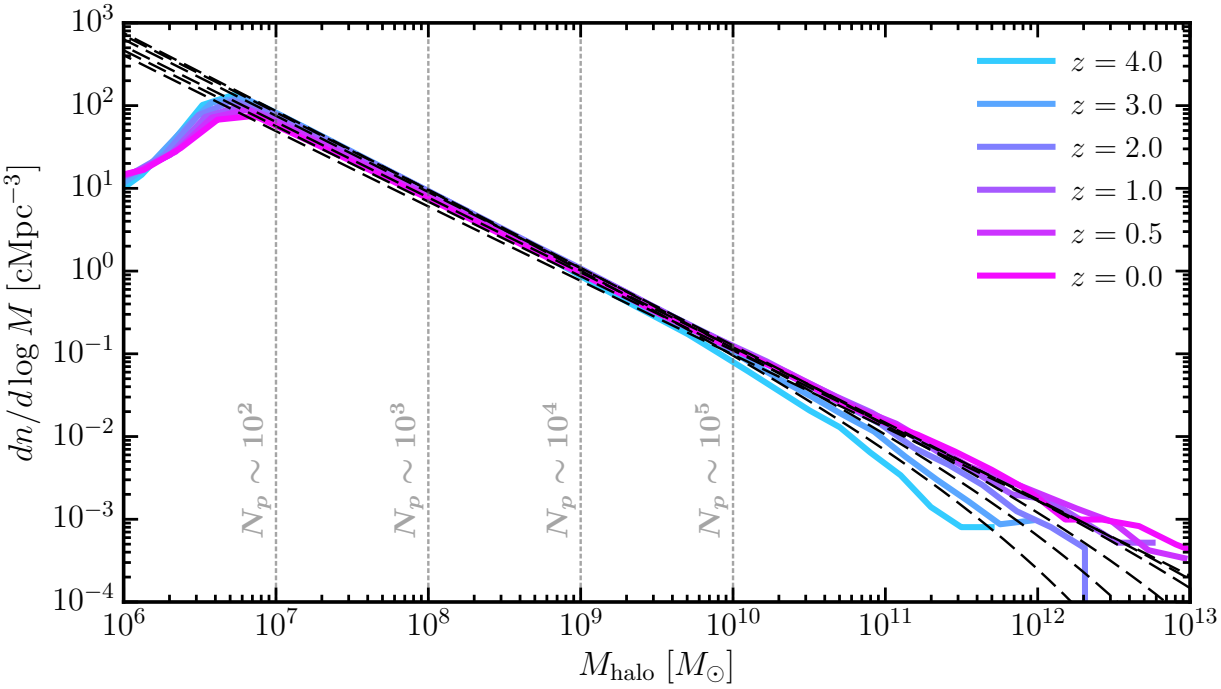

Figure 1.1: The abundance of cold dark matter halos within a confined (comoving) volume of the Universe. The black dashed lines shows the dark matters halo mass function at different redshifts for the full population of halos in the Universe as approximated by Sheth and Tormen (2002) while the colored lines are generated from a cosmological simulation of only collisionless dark matter.

1.2.4 Density structure

The spherically average three-dimensional density profiles of dark matter halos in the field, ρ, have been historically described by a nearly universal form over all masses, with a mildly divergent cusp ($\rho \propto r^{-1}$) towards the center of the halo transitions to a steep fall-off at large radii ($\rho \propto r^{-3}$). Dark matter halos in ΛCDM are commonly modeled by the Navarro, Frank, and White (NFW) density profile (Navarro et al. 1997).

$$\rho_{\rm NFW}(r) = \rho_s \left(\frac{r}{r_s}\right)^{-1} \left(1 + \frac{r}{r_s}\right)^{-2} , \tag{1.12}$$

where r_s is the scale radius and ρ_s is the scale density. The structure of a NFW halo is primarily parameterized by the concentration ($\overline{c}$) of a dark matter halo, which is formally defined as the ratio between the size of the halo, R_Δ, and the scale radius, r_s:

$$\overline{c}_\Delta := r_\Delta / r_s \, . \tag{1.13}$$

For dark matter only simulations pushed to much higher particle resolution than that studied in Navarro et al. (1997), dark matter halos are demonstrated in the literature to be even better described by the Einasto (1965) profile (Navarro et al. 2004, Gao et al. 2008, Navarro et al. 2010) for around 20 decades of halo masses (Wang et al. 2020):

$$\rho_\epsilon(r) = \rho_{-2} \exp\left\{ -\frac{2}{\alpha_\epsilon}\left[\left(\frac{r}{r_{-2}}\right)^{\alpha_\epsilon} - 1\right]\right\} . \tag{1.14}$$

Here, r_{-2} is the scale radius at which the log-slope profile is equal to -2, the scale density is $\rho_{-2} := \rho(r_{-2})$, and α_ϵ is the shape parameter. Usually α_ϵ can be fixed to eliminate its dependencies on values of r_{-2}. The internal structure from the Einasto profile can be parameterized by the

analogous dimensionless concentration parameter:

$$c_\Delta := r_\Delta / r_{-2}\,. \tag{1.15}$$

Note that r_s in the NFW profile is also the radius where the log slope of the NFW form is -2, so typically the Einasto concentration and NFW concentration are similar for any individual halo, i.e., $\overline{c}_\Delta \simeq c_\Delta$.

For a given system that has a spherically-averaged local density profile in three-dimensions, $\rho(r)$, the *local mean surface density* profile, $\Sigma_\rho(R)$ is quantified by integrating along the line of sight, ℓ, of a spherically symmetric lens:

$$\Sigma_\rho(R) = \int_{-\infty}^{\infty} d\ell\, \rho(R,\ell) \tag{1.16}$$

$$= 2\int_R^{\infty} dr\, \frac{r\rho(r)}{\sqrt{r^2 - R^2}}\,, \tag{1.17}$$

where R denotes the projected radius relative to the center of the halo and the last line is written as an Abel transformation (Binney and Tremaine 2008). For the NFW profile, the radial dependence of a NFW lens is inferred from integrating the above equation (Wright and Brainerd 2000):

$$\Sigma_{\rm NFW}(x) = \begin{cases} \frac{2\rho_s r_s}{(x^2-1)}\left[1 - \frac{2}{\sqrt{x^2-1}}\arctan\sqrt{\frac{x-1}{1+x}}\right] & x > 1 \\ \frac{2\rho_s r_s}{3} & x = 1 \\ \frac{2\rho_s r_s}{(x^2-1)}\left[1 - \frac{2}{\sqrt{1-x^2}}\mathrm{arctanh}\sqrt{\frac{1-x}{1+x}}\right] & x < 1 \end{cases}, \tag{1.18}$$

where $x = R/r_s$. While the Einasto profile describes the spherically averaged distribution of high-resolution dark matter halos to better accuracy (see comparison made in Chapter 3), the analytical lens properties tend to be more complicated to work with (see Retana-Montenegro et al. 2012),

e.g.,

$$\Sigma_\epsilon(y) = 2n\sqrt{\pi}\rho_0\, h\, y\, H^{2,0}_{1,2}\left[\begin{matrix}(0,1)\\(0,2n),(-\frac{1}{2},1)\end{matrix};y^2\right], \tag{1.19}$$

where $y := R/h$, $h := r_{-2}/(2/\alpha_\epsilon)^{1/\alpha_\epsilon}$, $\rho_0 := \rho_{-2}\, e^{2/\alpha_\epsilon}$, and H is the Fox H function. While the Einasto profile is accurate in modeling the three-dimensional distribution of dark matter, determining key properties for lensing, such as the deflection potential, leads to more complex forms of that quantity.

1.3 The importance of substructure lensing for constraining dark matter physics

One of the several predictions for Einstein's General Theory of Relativity associates the *deflection angle*, $\vec{\alpha}$, of a light ray to the mass distribution of a (dark or luminous) massive structure. The effect of a massive deflector, i.e., a *perturber*, can be approximated as a singularly sharp deflection in the plane of the lens via the "thin lens" approximation: where the distances scales found between the observer, lens, and source are exceedingly greater than the physical extent of the lensing mass distribution in question. Let us define projection of a perturber's local, three-dimensional density profile as $\Sigma(\vec{\xi})$, where $\vec{\xi}$ is the coordinate onto the plane of the lens, such that the deflection angle is given by (Blandford and Narayan 1986):

$$\vec{\alpha}(\vec{\xi}) = \frac{4G}{c}\int \mathrm{d}^2\xi' \frac{\left(\vec{\xi}-\vec{\xi}'\right)\Sigma(\vec{\xi}')}{|\vec{\xi}-\vec{\xi}'|^2}, \tag{1.20}$$

where c is the speed of light constant and G is the gravitational constant. Note that the cumulative effect for multiple perturbers in a lens system is a linear superposition of their individual deflection

angles.

As better detailed in the next subsection (see Figure 1.2 for visual reference), the configuration for a strong lens system includes both subhalos associated with the host dark matter halo of the lensing galaxy, i.e., *the main lens*, and the contribution from the *line-of-sight* (LOS) population, which is populated by the field halos. Field halos are incorporated by using the *multi-plane ray tracing equation*, which determines where images appear to the observer. The ray tracing equation maps an angular coordinate on the sky, $\vec{\theta}$ to an angular coordinate on the source plane, $\vec{\theta}_{\rm s}$, and is dependent on the net deflection angle from all halos within the lens plane (Blandford and Narayan 1986), i.e.,

$$\vec{\theta}_{\rm s}(\vec{\theta}) = \vec{\theta} - \frac{1}{D_{\rm s}} \sum_{i=1}^{\rm s-1} D_{i{\rm s}} \vec{\alpha}_i \left(D_i \vec{\theta}_i \right) \tag{1.21}$$

where D_{ij} is the angular diameter distance from the ith lens plane to the jth lens plane and $D_{\rm s}$ is the angular diameter distance to the source lens plane. The above equation couples deflections produced by objects at different distances, as it is recursive for the position of deflected light rays at each lens plane.

Lastly, the magnification of the lensed images are to be proportional to the ratio of areas in the source and image planes due to the surface brightness of the source remaining conserved in gravitational lensing phenomena. This magnification factor is quantified by the inverse determinant of the Jacobian,

$$\left(\det \left| \frac{\partial \vec{\theta}_{\rm s}}{\partial \vec{\theta}_{\rm o}} \right| \right)^{-1} , \tag{1.22}$$

which is notoriously complex in a multi-plane lens system in which the image magnification is non-linearly dependent on derivatives of the lensing deflection angle (Blandford and Narayan 1986).

Dark matter halos frequently perturbing image magnifications of strong lensing phenomena was

conjectured by Mao and Schneider (1998). Now, in the current literature, strong gravitational lensing has been shown to be a promising technique for detecting and characterizing small dark matter halos via lensing *flux anomalies*: smoothly-parameterized mass distributions fail to reproduce the magnifications ratios observed in quadruple lens systems (Dalal and Kochanek 2002, Moustakas and Metcalf 2003, Vegetti et al. 2010, Hezaveh et al. 2016, Li et al. 2017). More importantly, gravitational studies of low-mass dark matter substructures will deliver the necessary information for both astrophysicists and particle physicists looking to understand dark matter. In the standard ΛCDM model, the smallest halos ($M \leq 10^7 M_\odot$) are predicted to contain no stars and be virtually free of baryons. A dark matter halo as small as this near a lensed image (while also dependent on the size of the background source, the image's relative position to the critical curve, and the mass of the main lens), could induce *measurable* perturbations on image magnifications for background sources of orders around 10 pc. Gravitational detection of these structures, which are purely composed of dark matter, would be revolutionary in the field of theoretical physics, as it would confidently exclude all gravitational models that explain observed mass differences via modifications of Newtonian (or Einsteinian) gravity.

In order to take advantage of the expected advances in instruments to be deployed for future lensing surveys, there is a need for solid predictions of the *abundance* and and *density structure* of these low-mass dark matter halos. However, predictions at this high caliber requires high resolution, cosmological volumes, and inclusion of baryonic physics to properly account for the realistic processes found in galaxy formation: subhalo disruption, baryonic mass loss at reionization, and other dynamical feedback on the small halos of interest. The contents of this dissertation mostly focuses on modeling the abundance and structure of the LOS population using dark matter only (DMO) simulations, as the low-mass halos of interests are not likely to be affect by baryonic feedback (e.g., Lazar et al. 2020). The next section brings together the information detailed in the previous sections and provides a clear and concise presentation of the machinery that the dissertation provides for the scientific community.

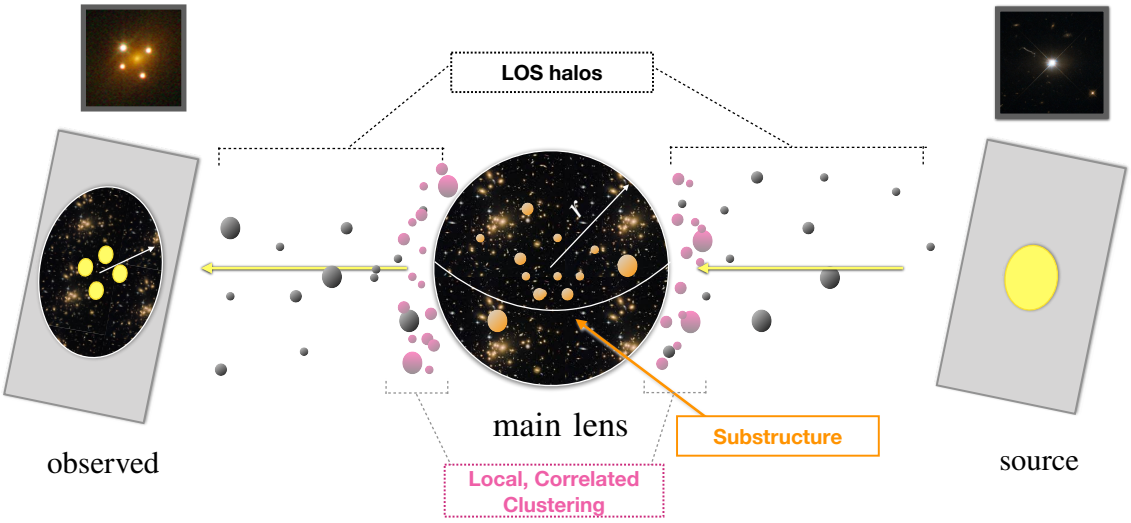

Figure 1.2: Low-mass halos along the line of sight to a lens galaxy act to perturb the image. They may be categorized in three regions: average line-of-sight (LOS) perturbers far from the lens (black circles); halos outside the lens virial radius but within a correlation length (pink circles), and subhalos within the virial radius (orange circles).

1.4 Substructure lensing configuration

Consider the illustration provided by Figure 1.2. Starting from the far right of the figure and following the yellow arrows all the way to the left, a source (e.g., a quasar) emits photons from a source redshift, z_s. These photons propagate through space and, if aligned just right, pass through a very large and very dense mass system dubbed the "main lens" at the lens redshift, z_l. With perfect alignment, the mass field at the center of the main lens is able to bend the geodesic paths of the emitted photons, and create multiple images that someone on Earth can observe. Now populate the entire path the photons takes between the source and observer with low-mass, dense halos. Low-mass halos along the line of sight to a lens galaxy act to perturb the source image and they can be partitioned into three classifications:

- *Average, LOS perturbers*: Far from the main lens and populate regions between the source and the observer.
- *Correlated structure*: Halos outside the lens virial radius but within a correlation length, which is expected to have a non-trivial effect.
- *Substructure*: Halos' centers within the main len's virial radius, impacted by tidal forces.

When considering lens perturbations, it is expected that low-mass halos in the field, i.e., along the line-of-sight to a lensed galaxy, contribute more than the subhalos of the main lens. Again, this dissertation explores more accurate ways in improving the way of modeling LOS halos, within ΛCDM, for substructure lensing studies.

As a starting baseline, these are the two quantities that are tackled within the main body of this document, as well as how they are currently implemented within substructure studies:

1. ***Abundance***: *It is essiential to accurately model how many of the LOS population of dark matter halos, with a given mass, $M_{\rm halo}$, populate a given (comoving) volume, V*, i.e.,

$$\left.\frac{\mathrm{d}N}{\mathrm{d}V\,\mathrm{d}M_{\rm halo}}\right|_{\rm LOS} . \tag{1.23}$$

   Note that the population of LOS halos within the volume of a lens configuration are inherently a piece of the field population of dark matter halos, which the number of field halos within a volumetric portion of the Universe has been sufficiently modeled in the literature as by halo mass function (see discussion in Section 1.2.3). This will at times be referred to as the *averaged* or *smooth* background population within the literature. We expected the contribution to the LOS mass function to be proportional to the average background, i.e.,

$$\left.\frac{\mathrm{d}N}{\mathrm{d}V\,\mathrm{d}M_{\rm halo}}\right|_{\rm LOS} \propto \frac{\mathrm{d}N_{\rm smooth}}{\mathrm{d}V\,\mathrm{d}M_{\rm halo}} . \tag{1.24}$$

Again, the mass function has been heavily modeled to numerical simulations within the literature (e.g., Press and Schechter 1974, Sheth and Tormen 1999, Tinker et al. 2008) and can be easily implemented within numerical software to sample LOS halos within a lens configuration. Figure 1.1 again shows an example of such model (in this case, the Sheth and Tormen 2002 mass function) compares to predicted simulation outputs.

The next order of contribution to Equation 1.23 is how correlated structure, i.e., the structure congregating the vicinity of the main lens (see Figure 1.2 for visual), is modeled within a lens configuration. Analysis performed by Gilman et al. (2018, 2019, 2020a,b) attempts to model this component, which assumed that a factor of the two-halo term and is proportional to the halo bias (quantifies the excess clustering of halos over the clustering of dark matter, e.g., Sheth and Tormen 1999), that amplifies the abundance at a given distance until averaging out to the smooth background density, i.e.,

$$\left.\frac{\mathrm{d}N}{\mathrm{d}V\,\mathrm{d}M_{\mathrm{halo}}}\right|_{\mathrm{LOS}} \propto \left[1 + \xi_{\mathrm{2halo}}\left(r, M_{\mathrm{lens}}\right)\right] \frac{\mathrm{d}N_{\mathrm{smooth}}}{\mathrm{d}V\,\mathrm{d}M_{\mathrm{halo}}}\,. \tag{1.25}$$

where ξ_{2halo} is the analytical two-halo term and is a function of the three-dimensional distance and main lens mass, r and M_{lens}, respectively. In Chapter 2, we fully explore this contribution of local, correlated structure of lens mass halos of interest by using, for the first time, a suite of cosmological simulations. There, we provide an analytical functions that considers not just the two-halo term, but also the back-splash population of halos which have yet to be taken into consideration.

2. ***Halo Density Structure***: *It is essential to accurately model the distribution of dark matter for LOS halos, for a given halo mass.* By far the most straightforward approach is to model dark matter halos within the field as having a NFW profile (Equation 1.12). Moreover, the structure of a NFW halo is can parameterized by the concentration. Having the three-dimensional structure, it is straightforward to integrate along the line-of-sight to acquire the surface density profile (Equation 1.18). Historically, the concentration of dark matter halos have been related

to the mass of the halo and can be modeled analytically as a function of mass, $M_{\rm halo}$, and redshift, z, i.e., the *halo concentration-mass relation*: $c(M_{\rm halo}, z)$. In addition, at fixed $M_{\rm halo}$, the scatter in concentration is log-normal for mass scales of interest (e.g. Bullock et al. 2000, Dutton and Macciò 2014). Combining these facts allows one to statistically sample from the concentration-mass relation for a given mass and infer the perturbations induced by the LOS population.

Their are possible shortcomings to this approach however, as the spherical-symmetric density definition only computes the average density and might bias the inferred mass upon projection, i.e., dark matter halos are elongated and will have different surface density profiles based on their orientation for a fixed halo mass. In Chapter 3, we explore these nuances and propose a more accurate model by directly modeling the results of projected dark matter distributions of simulated, high-resolution dark matter halos down to $M_{\rm halo} \simeq 10^7\,M_\odot$. In Chapter 4, we further extend this new model and compile statistical functions using a DMO cosmological box of sufficient resolution.

1.5 Other work

It has been said that a dissertation that goes exactly as planned is a boring dissertation. I'm happy to say that this one was not exactly boring, as I have tackled, on several occasions, other subfields across astrophysics and cosmology. Those that have come into fruition and later published ranged from other creative ways of modeling the structure of dwarf galaxies and exploring the early universe with the near-field and from transients of the first stars. A bibliography of papers I've been a part of during my time as a Ph.D. student that are not included in this thesis are below:

1. **Lazar, A.** and Bromm, V., 2022, "Probing the initial mass function of the first stars with transients", arXiv:2110.11956 , MNRAS, 511, 2505.

2. Moreno, J., Danieli, S., Bullock, James S., Feldmann, R., Hopkins, P., Çatmabacak, O., Gurvich, A., **Lazar, A.**, Klein, C., Hummels, C., Hafen, Z., Mercado, F.. Yu, S., Jiang, F., Wheeler, C., Wetzel, A., Anglés-Alcázar, D., Boylan-Kolchin, M., Quataert, Eliot, Faucher-Giguère, C.-A., Kereš, D., 2021, "Galaxies lacking dark matter produced by close encounters in a cosmological simulation", arXiv:2202.05836, Nature Astronomy, 6, 496.

3. Velàzquez, J. F., Gurvich, A. B., Faucher-Giguère, C.-A., Bullock, J. S., Starken-burg, T. K., Moreno, J., **Lazar, A.**, Mercado, F. J., Stern, J., Sparre, M., Hayward, C., Wetzel, A., El-Badry, K., 2020 "The time-scales probed by star formation rate indicators for realistic, bursty star formation histories from the FIRE simulations", arXiv:2008.08582, MNRAS, 501, 4812.

4. **Lazar, A.**, Bullock, J. S., Boylan-Kolchin, M., Chan, T.-K., Hopkins, P. F., Graus, A., Wetzel, A., El-Badry, K., Wheeler, C., Straight, M. C., Kereš, D., Fauche-Giguère, C.-A., Fitts, A., Garrison-Kimmel, S., 2020, "A dark matter profile to model diverse feedback-induced core sizes of ΛCDM haloes", arXiv:2004.10817, MNRAS, 497, 2393.

5. **Lazar, A.** and Bullock, S., 2020, "Accurate mass estimates from the proper motions of dispersion-supported galaxies", arXiv:1907.08841, MNRAS, 493, 5825.

6. Jahn, E. D., Sales, L. V., Wetzel, A., Boylan-Kolchin, M., Chan, T.K., El-Badry, K., **Lazar, A.**, Bullock, J. S., 2019, "Dark and luminous satellites of LMC-mass galaxies in the FIRE simulations", MNRAS, 489, 5348.

Chapter 2

The impact of correlated clustering in substructure lensing

A promising route for revealing the existence of dark matter structures on mass scales smaller than the faintest galaxies is through their effect on strong gravitational lenses. This chapter examines the role of local, lens-proximate clustering in boosting the lensing probability relative to contributions from substructure and unclustered line-of-sight (LOS) halos. Using two cosmological simulations that can resolve halo masses of $M_{\rm halo} \simeq 10^9\ M_\odot$ (in a simulation box of length $L_{\rm box}$~100 Mpc) and $10^7\ M_\odot$ ($L_{\rm box} \sim 20$ Mpc), we demonstrate that clustering in the vicinity of the lens host produces a clear enhancement relative to an assumption of unclustered halos that persists to $> 20\,R_{\rm vir}$. This enhancement exceeds estimates that use a two-halo term to account for clustering, particularly within $2 - 5\,R_{\rm vir}$. We provide an analytic expression for this excess, clustered contribution. We find that local clustering boosts the expected count of $10^9\ M_\odot$ perturbing halos by ~35% compared to substructure alone, a result that will significantly enhance expected signals for low-redshift ($z_l \simeq 0.2$) lenses, where substructure contributes substantially compared to LOS halos. We also find that the orientation of the lens with respect to the line of sight (e.g., whether the line of sight passes through the major axis of the lens) can also have a significant effect on the lensing

signal, boosting counts by an additional $\sim 50\%$ compared to a random orientations. This could be important if discovered lenses are biased to be oriented along their principal axis.

2.1 Chapter context

The large-scale clustering of galaxies provides important constraints on the makeup and evolution of the Universe (e.g. Geller and Huchra 1989, Bond et al. 1996, Tegmark et al. 2004, Sánchez et al. 2006). The dark energy plus cold dark matter (CDM) paradigm, ΛCDM, is entrenched as the benchmark model for the theory of galaxy formation based largely on its success in matching observed large-scale structure. For years, cosmological N-body simulations that incorporate only gravitational dynamics (dark matter only, DMO, simulations) have served as crucial tools for understanding the ΛCDM model, and have been used to understand the detailed clustering of galaxies. When introducing full galaxy formation physics, cosmological simulations are able to match observed clustering statistics as a function of galaxy type as well (e.g. Vogelsberger et al. 2014a, Genel et al. 2014, Schaye et al. 2015, Khandai et al. 2015, Dubois et al. 2016, Dolag et al. 2016, Springel et al. 2018, Vogelsberger et al. 2020) however some discrepancies on smaller scales exist and motivate the exploration of alternative models (Bullock and Boylan-Kolchin 2017, Meneghetti et al. 2020).

A feature of CDM that profoundly separates it from many other dark matter models is that CDM predicts a rich abundance of low-mass dark matter halos $M_{\rm halo} < 10^6\ M_\odot$ (Press and Schechter 1974, Bullock and Boylan-Kolchin 2017). In cosmologies that include warm dark matter (WDM), for example, the power spectrum is suppressed on scales smaller than a value set by the WDM particle mass (Bode et al. 2001, Bozek et al. 2016). For a thermal WDM particle of mass $m_{\rm thm} \lesssim 5$ kev, the formation of halos $< 10^7\ M_\odot$ (e.g. Schneider et al. 2013, Horiuchi et al. 2016) is suppressed. Therefore, if halos below $\simeq 10^7\ M_\odot$ are detected, this would impose significant constraints on both the dark matter power spectrum and the particle nature of dark matter (see Bertone and Tait 2018).

Dark matter halos of sufficiently low mass are expected to be unable to form stars or retain baryons in the presence of a cosmological photoionizing background (e.g. Efstathiou 1992, Bullock et al. 2000). The detection of these starless halos, *with the abundance and density structure predicted by simulations*, would be triumphant for the CDM model. One way of inferring the presence of these low-mass objects is by their influence on cold, low-velocity stellar streams in the Milky Way (Ibata et al. 2002, Carlberg 2009, Yoon et al. 2011). Recently Banik et al. (2019) argued that the observed perturbations of the MW's stellar streams can only be explained by a population of subhalos in CDM. They set constraints to alternative dark matter models for halos down the mass function, notably setting a lower limit on the mass of warm dark matter thermal relics $m_{\rm thm} \gtrsim [4.6-6.3]$ keV. In order to provide tighter constraints for substructure down to $M_{\rm halo} \simeq 10^{5-6} M_{\odot}$ populating the MW, a larger sample cold streams would be needed. Another proposed approach to detecting these low-mass halos could be through the kinematics of stars in the Milky Way's disk (Feldmann and Spolyar 2015).

Currently, the field of strong gravitational lensing offers to be another tool for the indirect detection of low-mass, starless halos of masses $\simeq 10^{6-8}\ M_{\odot}$ (Dalal and Kochanek 2002, Koopmans 2005, Vegetti et al. 2010, 2014, Li et al. 2016, Nierenberg et al. 2017). Lensing perturbations can arise from both subhalos within the lens host and from small halos found outside of the virial radius that perturb the light from source to the observer (dubbed "line-of-sight" (LOS) halos; Li et al. 2017, Despali et al. 2018). Notably, the field of substructure lensing offers tantalizing prospects, as in the near future, we expect both a gross increase in the number of lenses as well as a boost in resolution for instrument sensitivity. Forecasts suggest that the Dark Energy Survey (*DES*), The *Large Synoptic Space Telescope* (*LSST*), and *EUCLID* should discover hundreds of thousands of galaxy-galaxy lensing systems (Collett 2015). The *Nancy Grace Roman Space Telescope* (*RST*) also has the potential of providing complementary catalogs of lens images (Weiner et al. 2020). Additionally, the detection of halos with $M_{\rm halo} \sim 10^{7-8}\ M_{\odot}$ might be possible with *JWST* via quasar flux ratio anomalies (MacLeod et al. 2013). As of now, reported detections using *ALMA* reach the mass scale of classical Milky Way satellites ($M_{\rm halo} \sim 10^{10} M_{\odot}$), with constraints on subhalos

an order of magnitude smaller. In the future, further observations and improved constraints may significantly improve these limits (Hezaveh et al. 2016) and offer tighter constraints on the warm dark matter mass (He et al. 2020), especially when combined with Milky Way satellite constraints (Nadler et al. 2021).

The expected count of subhalos that exist within the virial radius of the lens system has been studied rigorously. Studies of subhalo populations and their effect on lensing have previously relied on DMO simulations (e.g. Bradač et al. 2002, Xu et al. 2009, 2012, Metcalf and Amara 2012, Vegetti et al. 2014). More recently, however, simulations that implement full galaxy formation physics show that small subhalos are actually depleted with respect to DMO simulations, owing to interactions with the central galaxy (Brooks and Zolotov 2014, Wetzel et al. 2016, Zhu et al. 2016, Graus et al. 2018, Kelley et al. 2019, Richings et al. 2021). Notably, Garrison-Kimmel et al. (2017) showed that it is the central galaxy potential itself, not feedback, that drives most of the factor of ~ 2 difference in subhalo counts between DMO and full physics simulations for Milky Way-mass halos ($M_{\rm vir} \simeq 10^{12}\ M_{\odot}$). For lens-mass halos of interest ($M_{\rm vir} \simeq 10^{13}\ M_{\odot}$), Despali and Vegetti (2017) used both DMO and full physics from the EAGLE (Schaye et al. 2015) and Illustris (Vogelsberger et al. 2014b) simulations to investigate predictions for subhalo lensing and found that simulations with full galaxy formation physics reduces the average expected substructure counts. The substructure analysis done in Graus et al. (2018) using Illustris found similar results.

Given the expected depletion in subhalo counts seen in full-physics simulations, the contribution of lensing signals from LOS halos has been recognized as ever more important. If LOS halos dominate the signal from a given lens, then uncertainties are reduced substantially because the contribution of the LOS halos can be accurately calculated, independent of the effect of baryonic physics, for a variety of cosmologies. Efforts have been made to understand the contribution of the LOS structure on the flux-ratio anomalies in lensed quasars (e.g. Metcalf 2005, Metcalf and Amara 2012, Xu et al. 2012, Inoue and Takahashi 2012, Inoue et al. 2015, Xu et al. 2015, Inoue 2016, Gilman et al. 2018, 2019). It has become increasingly apparent that LOS halos should dominate the signal for more

distant lenses ($z_l \sim 0.5$) while the contribution from subhalos should be non-negligible for more local lenses ($z_l \sim 0.2$; Despali and Vegetti 2017).

The objective in this chapter is to understand and quantify an effect not discussed in most previous work: how does local, correlated structure, in the vicinity of the lens host halo, impact the expected lensing signal? While such an effect has been discussed before in the context of weak lensing (D'Aloisio et al. 2014), its impact in strong lensing remains elusive. This effect will be most important for low-redshift lenses, where subhalos are known to contribute non-trivially compared to the LOS count. We use a suite cosmological simulations, including those that include both DMO and and full galaxy formation physics, to explore this question. Specifically, we quantify correlated structure in lens-centered projections of targets lens halos of $M_{\rm vir} \simeq 10^{13}\,M_{\odot}$ at redshift $z = 0.2$, corresponding with the benchmark sample discussed in Vegetti et al. (2014). This is done using two simulation projects: The first, from the public IllustrisTNG project (Nelson et al. 2018), includes both DMO and full-physics versions and resolves halos down to $M_{\rm halo} = 10^{9}\,M_{\odot}$ in a fairly large cosmological volume. The second is a DMO simulation evolved in much a smaller cosmological volume that is able resolve dark matter halos down to $M_{\rm halo} = 10^{7}\,M_{\odot}$.

This chapter is structured as follows. Section 2.2 introduces our set of simulations, provides a description of the selected sample of halos, and outlines our methodology for counting structures along projected line-of-sights in the simulations. Section 2.4 provides results on structure and explores how the lens-host orientation can boost the amount of structure expected along lens-centered projections. Finally, we summarize our results in Section 2.7.

2.2 Numerical methodology

Our ΛCDM predictions rely on two sets of simulations. The primary set comes from the public catalogs of the IllustrisTNG project[1] (Nelson et al. 2018, Marinacci et al. 2018, Springel et al. 2018, Naiman et al. 2018, Pillepich et al. 2018). As described in Section 2.2.1, these simulations allow us to identify halo populations robustly to masses greater than 10^9 $M_\odot$ for a *large-scale* environment both with gravitational physics alone and with full galaxy formation physics. The second simulation, introduced in Section 2.2.2, is a DMO version of a new simulation suite called FIREbox, which is part of the Feedback in Realistic Environments (FIRE) project.[2] The mass functions of these simulations are presented in Figure 2.1. Both simulations assume a Planck 2015 cosmology (Planck Collaboration et al. 2016a): $\Omega_\mathrm{m} = 0.3089$, $\Omega_\Lambda = 0.6911$, $\Omega_\mathrm{b} = 0.0486$, $\sigma_8 = 0.8159$, and $h = 0.6774$.

Our analysis relies on halo catalogs at redshift $z = 0.2$, which coincides with a typical redshift of the lens-host sample explored in Vegetti et al. (2014). Dark matter halos are defined to be spherical systems with a virial radius, R_vir, inside which the density is equal to the average density of $\rho_\mathrm{vir}(z) = \Delta_\mathrm{vir}(z)\rho_\mathrm{crit}(z)$, where $\Delta_\mathrm{vir}(z)$ is the virial overdensity defined in Equation 1.4 and $\rho_\mathrm{crit}(z)$ is the critical density of the Universe, i.e., Equation 1.5. The virial mass, M_vir, is then the total mass enclosed in a sphere of radius R_vir, Equation 1.3.

In what follows, we discuss two types of halos: First, we have massive *target* halos, chosen to mimic lens-galaxy hosts: $M_\mathrm{vir} \in [0.8 - 2] \times 10^{13}$ $M_\odot$. Second, we have low-mass perturber halos, which can either be subhalos or small halos that exist somewhere outside of the host's virial radius and along the LOS from the observer. We quote their masses (taken from the halo catalogs) using the symbol M_halo, since for subhalos M_vir is not physically relevant.

[1]The Illustris data is publicly available at https://www.tng-project.org/
[2]The FIRE project website: http://fire.northwestern.edu

2.2.1 The IllustrisTNG simulations

The IllustrisTNG (TNG) suite of cosmological simulations was run using the moving-mesh code Arepo (Springel 2010). The runs with full galaxy formation physics use an updated version of the Illustris model (Weinberger et al. 2017, Pillepich et al. 2018). We use the high resolution set of publicly-available simulations,[3] TNG100-1, which has a comoving box of side length $L_{\rm box}^{\rm TNG} = 75\,h^{-1}{\rm cMpc} = 110.7\,{\rm cMpc}$. The full physics run, TNG100, has a dark matter particle mass of $m_{\rm dm} = 7.5 \times 10^6\ M_\odot$ and a gas particle mass of $m_{\rm gas} = 1.4 \times 10^6\ M_\odot$. The high-resolution simulation that uses dark matter only (DMO) physics, TNG100$_{\rm DM}$, has the same box size, but treats baryonic matter as collisionless particles, in which gives the simulation a particles mass is $m_{\rm dm} = 8.9 \times 10^6\ M_\odot$. When comparing between TNG100 and TNG100$_{\rm DM}$, we account for the excess baryonic mass in the DMO simulation by introducing a factor $m_{\rm dm} \to (1 - f_{\rm b})m_{\rm dm}$, where $f_{\rm b} := \Omega_{\rm b}/\Omega_{\rm m}$ is the cosmic baryon fraction.

For both TNG100 and TNG100$_{\rm DM}$, the dark matter halo catalogs were constructed using a friends-of-friends (FOF) algorithm (Davis et al. 1985) with a linking length 0.2 times the mean inter-particle spacing. Gravitationally bound substructures are identified through the SUBFIND halo finder (Springel et al. 2001). These subhalos have a dark matter mass that is gravitationally bound to itself but not to any other subhalos found in the same FOF host or the host itself. As shown in Figure 2.1, the $z = 0.2$ mass functions of the TNG100 (magenta) and TNG100$_{\rm DM}$ (cyan) SUBFIND subhalos match well with the analytical Sheth and Tormen (2002) mass function (dotted dashed) at that redshift. Both simulations become incomplete just below $M_{\rm halo} \simeq 10^{8.6}\ M_\odot$. In order to be conservative, we restrict our analysis to subhalos and field halos with resolved masses $M_{\rm halo} > 10^9\ M_\odot$. These halos contain at least 134 dark matter particles. TNG100 and TNG100$_{\rm DM}$ have 166 and 168 lens-target halos, respectively, where in TNG100, these halos typically host galaxies with $M_\star \simeq 10^{11}\ M_\odot$, which is consistent with the benchmark sample in Vegetti et al.

[3]The highest resolution box is actually TNG50-1, but was not publicly available by the time this chapter was submitted previously for publication.

(2014).

The public SUBFIND catalogs in TNG100 include several baryon-dominated "subhalos," many of which contain no dark matter. Most of these baryon-dominated objects exist within ~20 kpc of host galaxies and appear to be baryonic fragments numerically identified by SUBFIND rather than galaxies associated with dark matter subhalos. While baryonic clumps could induce perturbations detectable in lens images (Gilman et al. 2017, Hsueh et al. 2017, 2018, He et al. 2018), this type of object is not the focus of our analysis; we are interested in the search for low-mass *dark matter* structures. For this reason, we exclude systems with a ratio of total baryonic mass to dark matter mass that is more that twice the cosmic baryon fraction, ($M_{\rm bar}/M_{\rm halo} > 2 \times f_{\rm b}$) in the substructure analysis that follows.

2.2.2 The FIREbox DMO simulation

FIREBox is a new effort within the FIRE collaboration to simulate cosmological volumes of $L_{\rm box}^{\rm FIRE} = 15\ h^{-1}$cMpc = 22.14 cMpc at the resolution of FIRE zoom-in simulations (Feldmann et al. 2022). Our analysis uses the results from a DMO version of the FIREbox initial conditions, ran with 2048^3 particles, which we dub FIRE$\rm box_{DM}$ in this chapter. FIRE$\rm box_{DM}$ has a dark matter particle mass of $m_{\rm DM} = 5.0 \times 10^4\ M_\odot$ and was run with a Plummer softening length of $\epsilon_{\rm DM} = 40$ pc. Since we will work with a DMO simulation to complement the analysis done in the two TNG simulations, we again account for baryonic mass by multiplying a by conversion factor of $(1 - f_{\rm b})$, as we do for TNG$100_{\rm DM}$.These simulations are complete, conservatively, to halo masses down to $10^7\ M_\odot$ (see Figure 2.1).

The halo catalog for FIRE$\rm box_{DM}$ was generated using ROCKSTAR (Behroozi et al. 2013). This method finds dark matter halos using a hierarchically adaptive refinement of FOF in a 6-dimensional phase-space and one time dimension. We set our ROCKSTAR halo finding parameters to be comparable to those use in the TNG catalogs generated by SUBFIND. Specifically, we use a FOF linking

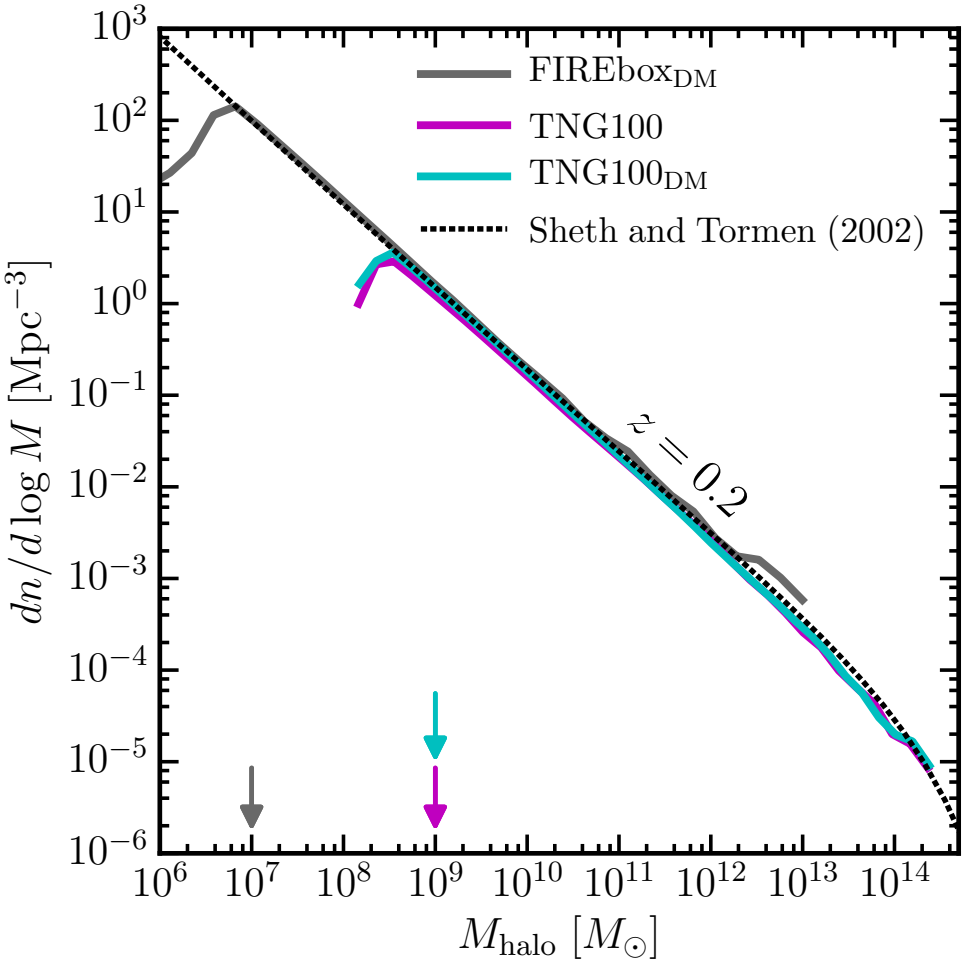

Figure 2.1: Shown are the halo mass functions of the simulations at $z = 0.2$. Results from all three simulation are in agreement with the analytical prediction of Sheth and Tormen (2002). The arrows pointing to the x-axis designate the minimally resolved mass considered in each simulation, indicated by the color coding.

length of $b = 0.20$ and include only halos that have at least 100 dark matter particles. We also set the criteria for unbound particle fraction rejection to 70% instead of the default 50%, as explored in the Appendix of Graus et al. (2018). Doing so minimizes ambiguities associated with using different halo finders for computing halo masses.[4] With these choices, FIREbox contains three target halos with mass $M_{\rm vir} \in [0.8 - 2] \times 10^{13}\ M_\odot$.

Returning to Figure 2.1, the mass function of FIREbox$_{\rm DM}$ at $z = 0.2$ is shown as the solid gray curve and agrees well with the analytical mass function down to halo masses with $10^{7-8}\ M_\odot$. With this in mind, the use of FIREbox$_{\rm DM}$ in our analysis will be restricted to two sets of subhalo masses: a sample of halo masses down to $10^7\ M_\odot$ ($\sim 10^2$ particles) and a sample of down to $10^8\ M_\odot$ ($\sim 10^3$ particles). For a more stringent check, Seciton 2.3 briefly compares the subhalo mass function and the subhalo $V_{\rm max}$ function of the three target-lens halos of FIREbox$_{\rm DM}$ to the same mass target-lens halos in TNG100$_{\rm DM}$. We find excellent agreement between substructure statistics between our halo samples.

2.2.3 Counting within lens-centered cylinders

We quantify perturber counts by enumerating small halos that sit within randomly-oriented *lens-centered cylinders* of length ℓ and radius $\mathcal{R}$, where ℓ can extend over the length of the simulation box and $\mathcal{R}$ will be set to a value close to an expected Einstein radius ($\sim$ 10 kpc). As illustrated in Figure 2.2, each cylinder is centered on a target halo in the simulation box. The volume of the cylinder is increased by lengthening $\ell \rightarrow \ell + \Delta\ell$ with the radius $\mathcal{R}$ fixed. In practice, $\mathcal{R} \ll R_{\rm vir}$. For a discrete increment variation of $\Delta\ell$, both ends of the cylinder are increased by $(\Delta\ell)/2$, which captures both structures whose positions are found in the foreground and background of the target halo. Doing so allows us to qualitatively compare counts as function of radius r from the halo

[4]We have also experimented with higher unbound fractions of 90% and 95% with a fixed value of $b = 0.20$. We chose the unbound fraction of 70% and a FOF linking of $b = 0.20$ because they provide the best match with TNG100$_{\rm DM}$ catalogs for $M_{\rm halo} > 10^9\ M_\odot$.

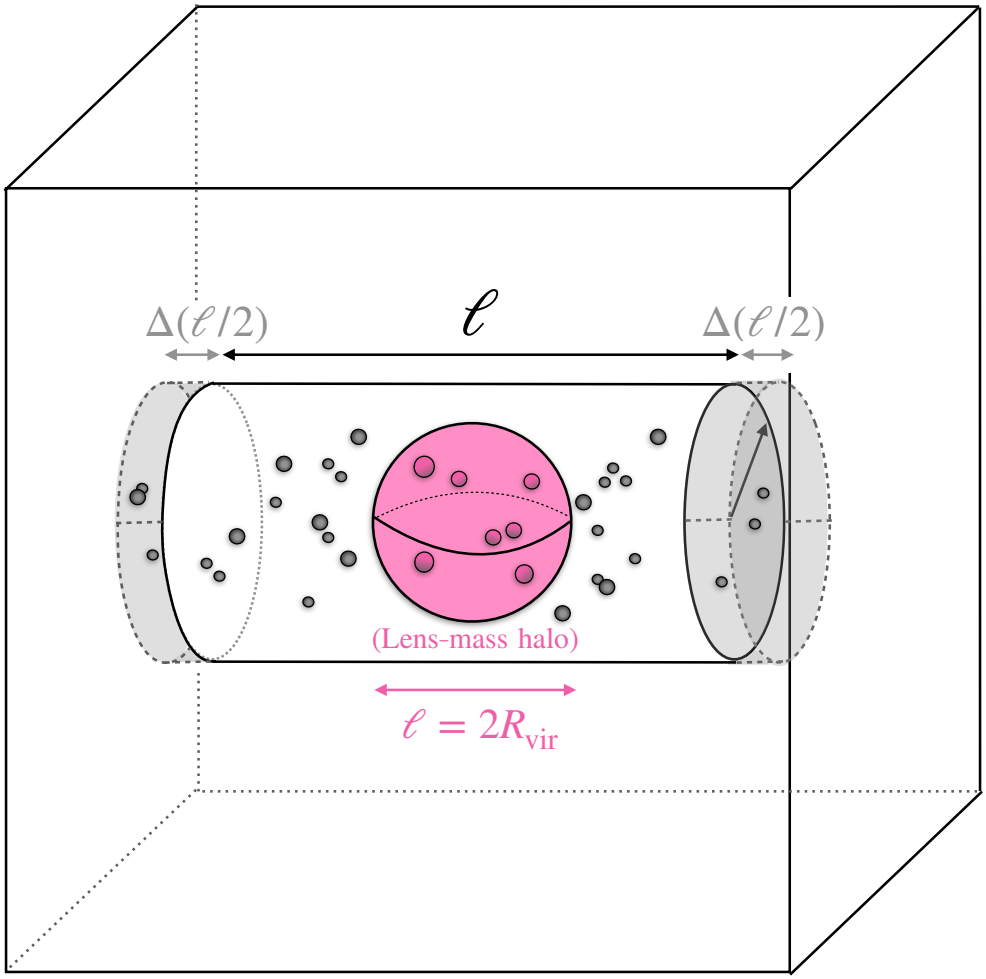

Figure 2.2: A cartoon depiction of the analysis performed for each lens-centered cylinder in a simulation box. The lens-mass halo, centered at the origin of the box, is illustrated as the large pink sphere, while subhalos are illustrated as smaller halos. With the cylinder held at a fixed $\mathcal{R}$, the cylinder is varied by increments of $\Delta\ell$ ($\Delta\ell/2$ at each end of the cylinder) until reaching the edge of the box. Note that the radius of the cylinder has been exaggerated for clarity. In practice, $\mathcal{R} \ll R_{\rm vir}$.

center, i.e., $r \simeq \ell/2$. For example, a lens-centered cylinder length of $\ell = 2R_{\rm vir}$ spans the full diameter of the dark matter halo.

In what follows we compare counts from lens-centered cylinders to those of *average* cylinders, which are configured like a lens-centered cylinder, but now with their centers randomly placed within the simulation box. Note for a large sample of average cylinders, the mean count per unit volume at any ℓ will be equal to the average halo density (e.g. Sheth and Tormen 2002). For both cylinder types, we take into account the periodicity of the cosmological box but never allow the

full cylinder length to exceed the box length.

Figure 2.3 provides a simple illustration of our counting prescription applied to TNG100 for a single lens-mass halo of $M_{\rm vir} \simeq 10^{13} M_{\odot}$ (labeled as "lens-centered cylinder") and for a randomly placed cylinder of the same size inside the box (labeled as "average cylinder"). For illustrative purposes, we have set the radius of the cylinder to a very large value $\mathcal{R} = R_{\rm vir} \simeq 500$ kpc, much larger than what we will use in our main analysis. The cylinder length is set to $\ell = 10$ Mpc. The filled circles show all subhalos with $M_{\rm halo} > 10^9\ M_{\odot}$. Points and circles are colored based on their relative distance from the host: within $\ell = 2R_{\rm vir}$ ($r = R_{\rm vir}$) as cyan, $\ell = [2-4]R_{\rm vir}$ ($r = [1-2]R_{\rm vir}$) as magenta, and black for everything else out to a length $\ell = 10$ Mpc. The two top plots show the edge-on projections while the bottom plots are the face-on projections. For the face-on projections, the sizes of the circles are scaled proportionally to the mass of the halos in the cylinder (with the host halo removed for clarity). In the bottom-left panel, we show only halos that are *outside* of $R_{\rm vir}$ of the lens-host. Even excluding substructure, the overall count is much higher than the random cylinder.

For this particular randomly-chosen "average" cylinder, we find 14 halos with $M_{\rm halo} > 10^9\ M_{\odot}$ within the 10 Mpc projection visualized. Note that the cosmological average expected for this volume is ≈ 14.3 when using the Sheth and Torman mass function (Sheth and Tormen 2002). Counts are significantly higher for the lens-centered cylinder. For comparison, the lens-centered cylinder contains 108 halos of the same mass. Interestingly, correlated structure counts around the lens-host that exist outside of $r = R_{\rm vir}$ but within $r = 2R_{\rm vir}$ is 28, which exceeds all of the counts within the 10 Mpc long average cylinder. This shows that clustering in the vicinity of the lens will boost signals non-trivially compared to what we would have estimated by ignoring local clustering outside of the halo virial radius.

While Figure 2.3 is useful to elucidate the point of a projected cylinder, the radius shown, $\mathcal{R} = R_{\rm vir}$, is not relevant for lensing studies. The remainder of the analysis hereafter imposes a fixed projected cylinder radius of $\mathcal{R} = 10$ kpc, which is a value comparable to size of the lens-mass' Einstein radius

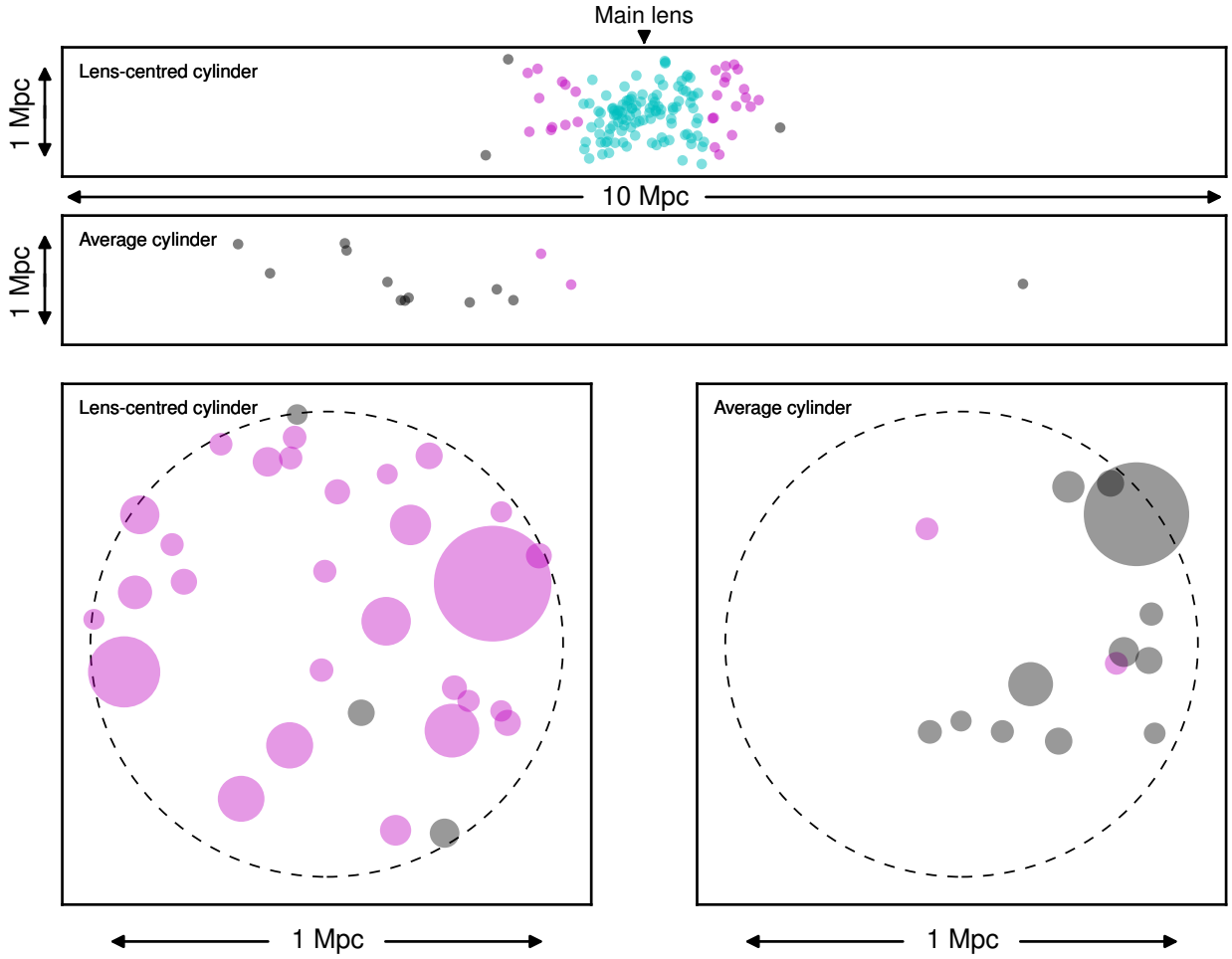

Figure 2.3: *The importance of correlated structure in sub-galactic lensing*. The upper and middle panels depict the side-view of a cylinder length of $\ell = 10$ Mpc and radius $\mathcal{R} = 500$ kpc centered on a lens-mass host halo with radius $R_{\rm vir} \simeq 500$ kpc at $z = 0.2$ in the TNG100 simulation. The points show locations of $M_{\rm halo} > 10^9\,M_\odot$ halos within the cylinder, color coded by relative distance from the host out to the size of the halo $\ell = 2R_{\rm vir}$ (or equivalently to $r = R_{\rm vir}$; cyan points), within $\ell = [2-4]\,R_{\rm vir}$ ($r = [1-2]\,R_{\rm vir}$; magenta points), and everything else outside $\ell = 4R_{\rm vir}$ out to $\ell = 10$ Mpc (black points). The figure beneath it shows an identical cylinder that samples a representative region of the simulation box using the same color scheme; the area of each point is proportional to that halo's mass. The square plots are the same cylinders shown face on, centered on the lens (left) and centered randomly (right). The cylinder radius $\mathcal{R} = 500\,$kpc used for this figure is, for illustrative purposes, much larger than the typical Einstein radius of the host ($\mathcal{R} \approx 10\,$kpc; we use the latter value for our actual analysis. *Local, correlated perturbers around the lens are highly significant* (compare the magenta points in the left verses right panels on the bottom)

(typically $\lesssim$ 10 kpc). Note that in the SLACS sample used by Vegetti et al. (2014) at a redshift $\langle z_{\rm lens} \rangle \sim 0.2$, the median Einstein radius is ~ 4.2 kpc. We adopt a slightly larger 10 kpc radius in what follows in order to improve counting statistics; see Section 2.5 for a discussion of counting variance. Our primary results below are framed as relative counts per unit volume, such that the precise radius of the cylinder factors out. We show in Section 2.5.1 that our results are insensitive (to within counting noise) to choices of cylinder radii of 5 kpc and even 2 kpc.

2.3 Comparison between mass functions of lens-mass sample

As mentioned in Section 2.2, the SUBFIND halo finder was ran for the TNG suites while ROCKSTAR was applied to FIREbox$_{\rm DM}$. Figure 2.1 provides confidence in the resulting halo catalogs used in the main text, as both catalogs show robust agreement with the analytical prediction. However, halo finders vary in routines for quantifying the masses for subhalos and can potentially produce different mass functions when ran to the same simulations. It would be worth comparing our resulting halo finders with one another based on the resolved substructure population found for our lens-target halos at $z = 0.2$.

Figure 2.4 shows the subhalo mass functions for the 10^{13} $M_\odot$ target-lens systems in TNG100$_{\rm DM}$ (purple) while the three from FIREbox$_{\rm DM}$ (black curves). The purple band for TNG100$_{\rm DM}$ encloses the 90% dispersion of all of the target-lens subhalo mass functions. Significant disagreement could arise based on the assignment of particles to subhalos from halo finders (Graus et al. 2018). To clarify this point, Figure 2.5 provides a different view of subhalo sample, where the subhalo $V_{\rm max}$ function for the same lens-target systems.

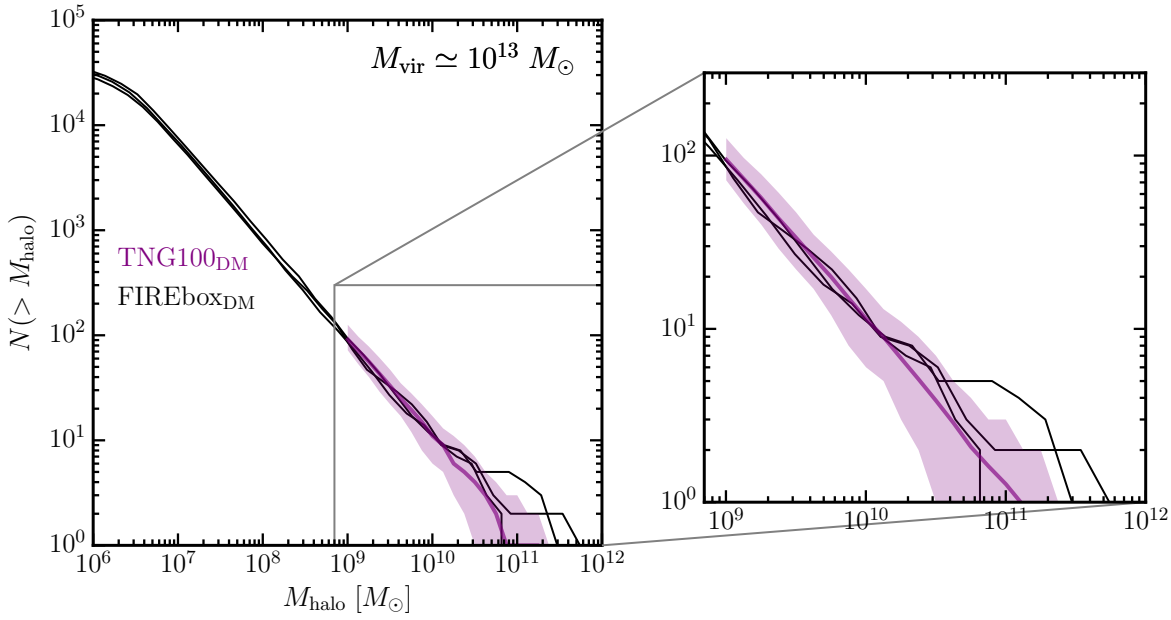

Figure 2.4: The subhalo mass functions for the lens-target halos in our main sample compared between the TNG100$_{\rm DM}$ (purple curve) and FIREbox$_{\rm DM}$ (black curves). FIREbox$_{\rm DM}$ follows the median TNG100$_{\rm DM}$ curves sufficiently for the subhalo masses ranging from $\sim 10^{9-10}\ M_\odot$ while the three lens-target in FIREbox$_{\rm DM}$ hosts several more massive $10^{11}\ M_\odot$. Though, the curves are still mostly found enclosed in the 90% dispersion. The agreement depicted from the subhalo mass functions provides further justification for the choice of our ROCKSTAR parameters detailed in Section 2.2.

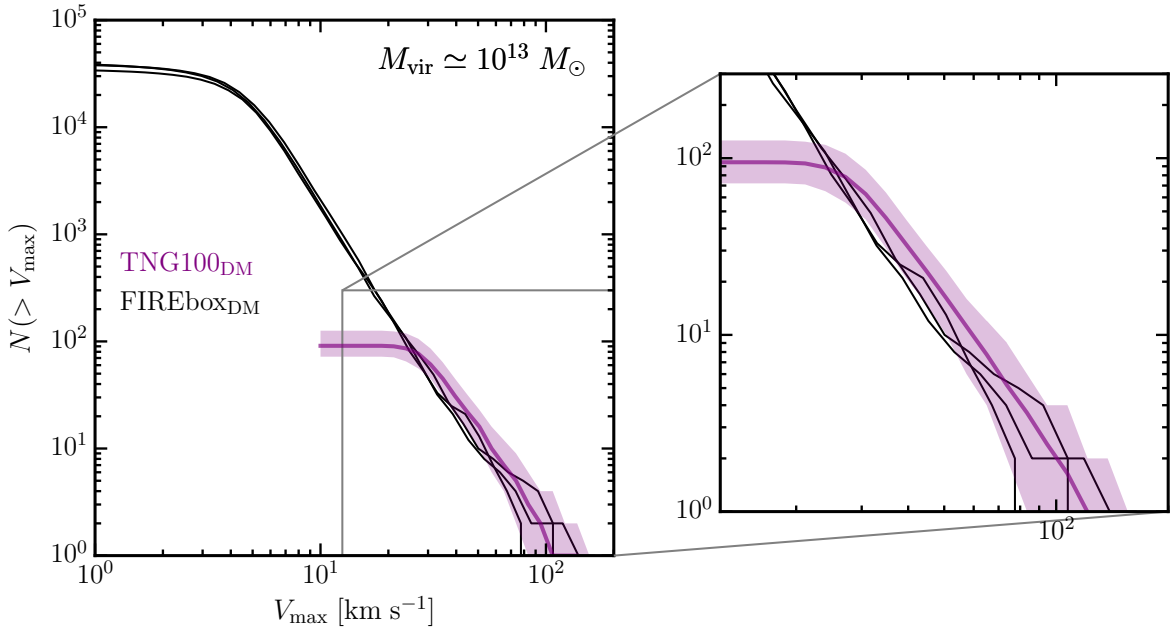

Figure 2.5: Similar to Figure 2.4, where the subhalo $V_{\rm max}$ functions for the lens-target halos in our main sample are plotted instead.

2.4 Key results

2.4.1 Average halo counts in projection

Our main results are presented in Figure 2.6, where we plot the *mean* differential count of halos per cylinder length, $\langle dN/d\ell \rangle$ using 100 cylinders randomly oriented around each lens-mass halo (solid lines). The cylinders mirror those shown in Fig 2.3, but now with a radius comparable to the Einstein radius of the lens-mass halos, $\mathcal{R} = 10$ kpc (and varying length ℓ). Integrating $dN/d\ell$ over ℓ gives the cumulative count $N(< \ell)$ within a cylinder of total length ℓ. We plot the differential count as a function of cylinder length, ℓ. Shown is the *mean* differential count rather than the *median* because this allows us to compare directly to analytic expectations for the average halo abundance. Each solid curve shows the rate of counts for halo masses greater than a given value (indicated in the legend), normalized by the rate of counts expected from the average background from Sheth and Tormen (2002). Counts equal to the rate of counts from the average background are shown as the horizontal dotted line with an amplitude of unity.[5] The vertical grey-dashed line separates between the two regimes of interest: the substructure contribution ($\ell < 2R_{\rm vir}$ and the local structure ($\ell > 2R_{\rm vir}$).

We see that for all simulations and mass cuts, the differential counts are above the average counts out to $r \sim 20$ Mpc ($\ell \sim 40\, R_{\rm vir}$). This is attributed to excess clustering in the vicinity of the massive host, an effect often ignored in lensing studies (see e.g. Despali et al. 2018, who assume average counts outside the virial radius), though some groups (e.g. Gilman et al. 2018) have attempted to account for the effect (see below). For perturbers more massive than $10^9\ M_\odot$, the rate of counts do not reach the average background until $\ell \sim 75 R_{\rm vir} \approx 40$ Mpc for both TNG100 (magenta), TNG100$_{\rm DM}$ (cyan), and FIREbox$_{\rm DM}$ (red, which is limited by only having three hosts). It is interesting also to compare TNG100 (magenta) to TNG100$_{\rm DM}$ (cyan). We see that at small ℓ

[5] We have also tested with a large number average cylinders in the simulations (as the example shown in Figure 2.3) and confirmed that the average background counts are consistent with analytical expectations of Sheth and Tormen (2002).

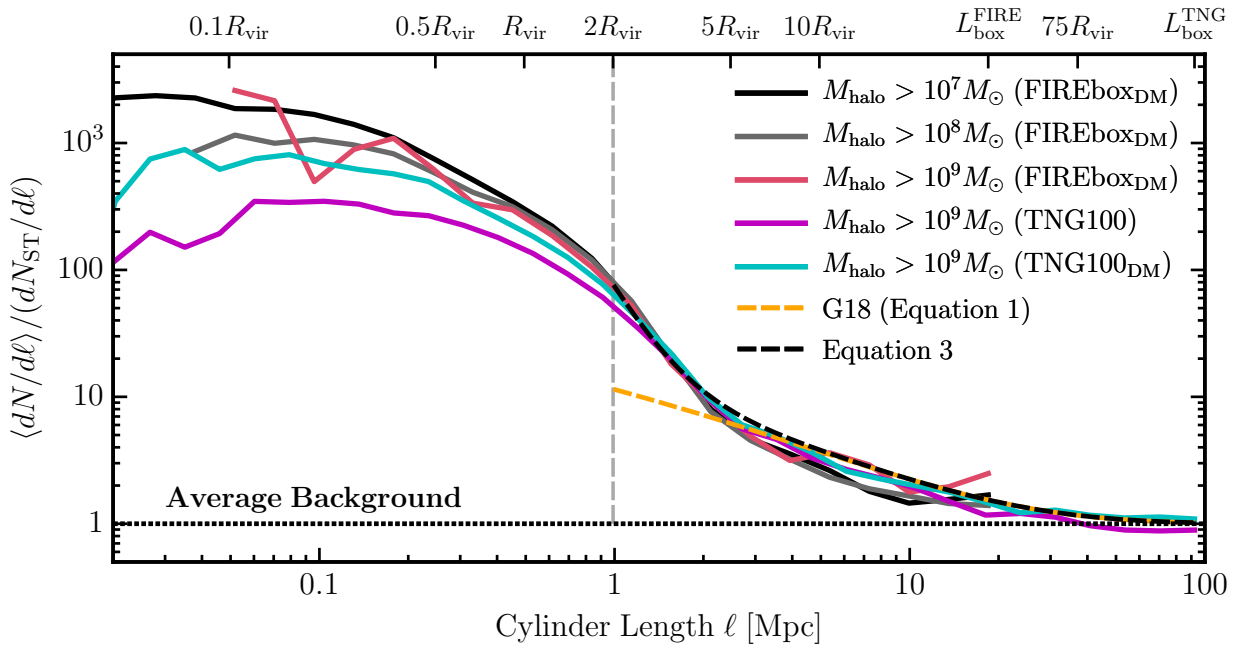

Figure 2.6: *Structure excess along lens-centered projections*: The mean differential count $\langle dN/d\ell \rangle$ of small halos within cylinders of increasing length $\ell + \Delta\ell$ centered on the lens-mass host halos ($M_{\rm vir} \simeq 10^{13} M_\odot$, solid colored), normalized by the expected average background counts via from analytical halo mass function (dotted black). The cylinders mirror those shown in Figure 2.3, but now with a radius comparable to the Einstein radius of the lens-mass halos, $\mathcal{R} = 10$ kpc (and varying length ℓ). The gray vertical dashed line marks the typical outer region of the halo ($\ell = 2R_{\rm vir} \leftrightarrow r = R_{\rm vir}$). Inside the lens-mass host halos ($\ell < 2R_{\rm vir}$), the differential counts are self-similar for the DMO simulations. For TNG100 (solid magenta), the counts decrease by almost a factor of 10 because of the destructive effect of the central galaxy. Differences between the curves become apparent outside the halo due to local halo clustering. This effect originates predominantly from "backsplash" halos that have pericenters with $r < R_{\rm vir}$ but apocenters of $r > R_{\rm vir}$, meaning they lie within the splashback radius of the lens-mass host but spend most of their time at $r > R_{\rm vir}$. For comparison, we plot the analytical contribution of the two-halo term given by G18 (Equation 2.1; dashed orange), where we set $\delta_{\rm los} = 1$. While G18 accurately reproduces the contribution at $\ell > 5 \times R_{\rm vir}$ for most of the curves, it significantly under-predicts the differential halo counts within $\ell \in [2 - 5] R_{\rm vir}$. Our proposed modification, Equation 2.3 (dashed black), captures the excess for $\ell > 2\, R_{\rm vir}$ to within 10%.

(corresponding to the center of the host halo), the overall count is higher in the DMO run. This comes about because of enhanced subhalo destruction from the central galaxy potential (e.g. Graus et al. 2018). Differential counts in FIREbox$_{\rm DM}$ are consistent with those in TNG100$_{\rm DM}$ for a lower mass threshold of $M_{\rm halo} = 10^9\,M_\odot$, though the FIREbox$_{\rm DM}$ result is noisier owing to the fact that there are only three target lens-mass halos in the volume. In Section 2.5, we further discuss the effect of sample variance in our analysis.

Comparing the $10^9\ M_\odot$ (magenta/cyan), $10^8\ M_\odot$ (gray) and $10^7\ M_\odot$ (black) lines, there is an indication that lower-mass halos contribute more near the center of the lens-host ($\ell \sim 0.1 R_{\rm vir}$). This would be expected if subhalo radial distributions within the host halo are more centrally concentrated at lower subhalo masses. Beyond the virial radius ($\ell > 2\,R_{\rm vir}$) the lower-mass halos found in FIREbox$_{\rm DM}$, $10^8\ M_\odot$ (gray) and $10^7\ M_\odot$ (black), track the enhanced counts seen at $10^9\ M_\odot$. For $\ell > 5 R_{\rm vir}$, the counts for lower mass halos in FIREbox$_{\rm DM}$ fall slightly below those seen in TNG. This difference could be physical. For example, lower mass halos may be less clustered around the lens host. However, the offset we see from $10^9\ M_\odot$ to $10^8\ M_\odot$ is much larger than would be expected naively from the clustering bias change over this mass range: $b(10^9 M_\odot) \simeq 0.64$ vs. $b(10^8 M_\odot) \simeq 0.63$ at $z = 0.2$ (Sheth and Tormen 1999). The difference could also arise from the lack of large-scale power in the small volume of FIREbox$_{\rm DM}$ or from simple sample variance from having only three host halos.

2.4.2 Analytic model comparison

Correlated structure outside of the virial radius of a massive target halo is related to the "two-halo term" of the halo-matter correlation function (e.g. Ma and Fry 2000, Seljak 2000, Smith et al. 2003). Gilman et al. (2018) (G18 hereafter) estimated this effect as

$$\frac{d^2N}{dm\ dV} = \delta_{\rm los}\Big[1 + \xi_{\rm 2halo}(r, M_{\rm vir}, z)\Big]\frac{d^2N_{\rm ST}}{dm\ dV},\ , \tag{2.1}$$

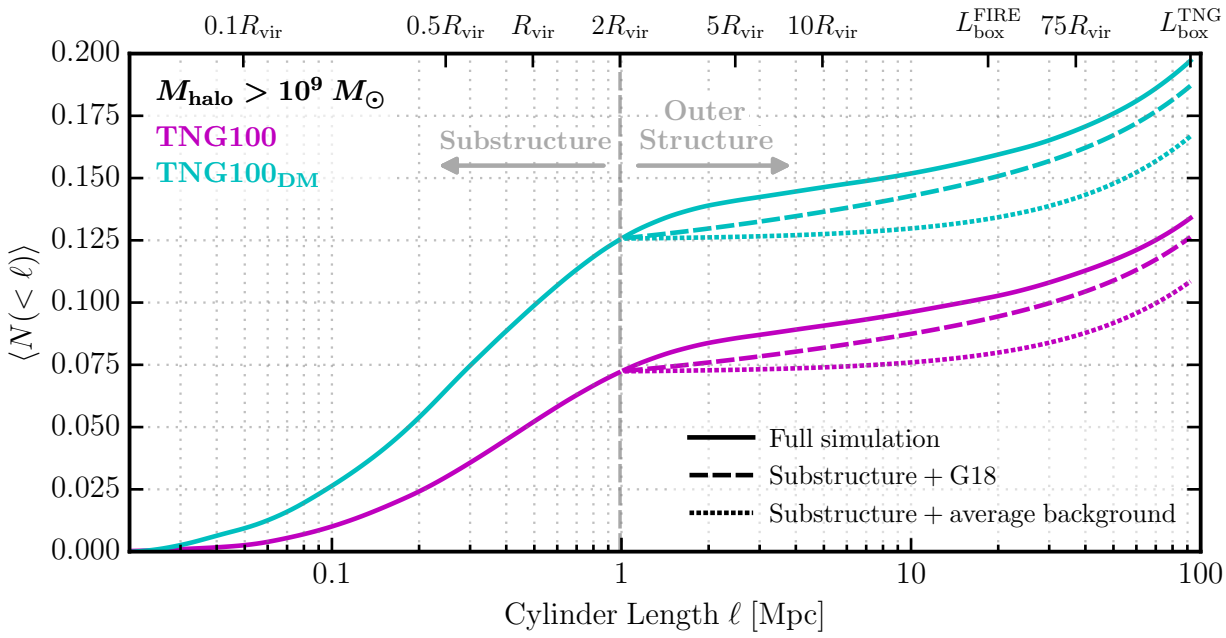

Figure 2.7: Solid lines show the integrated mean count of halos more massive than $10^9\ M_\odot$ within cylinders of radius $\mathcal{R}$ = 10 kpc and of length ℓ centered on lens hosts from TNG100 (magenta) and TNG100$_{\rm DM}$ (cyan). The gray vertical line marks the cylinder length at the halo boundary ($\ell = 2R_{\rm vir}$). The cumulative count of halos that would result without any adjustment for correlated structure beyond the virial radius is shown by the dotted lines. The predicted contribution of correlated structure from G18 (Equation 2.3) is shown by the dashed lines. In implementing G18, we set $\delta_{\rm los} = 1$ for TNG100$_{\rm DM}$, as the convergence to average is about one-to-one. However, for TNG100, we set $\delta_{\rm los} = 0.879$ to remain consistent with the average-count differences in TNG100$_{\rm DM}$. The G18 model captures much, but not all, of the correlated structure; the extra component beyond the G18 prediction comes from virialized halos beyond $R_{\rm vir}$ but within the splashback radius.

where $M_{\rm vir}$ is the mass of the host halo and $\delta_{\rm los}$ is an overall scaling term that accounts for a systematic shift of the mean number of halos predicted by the Sheth and Tormen (2002) mass function ($N_{\rm ST}$), and

$$\xi_{\rm 2halo}(r, M_{\rm vir}, z) = b_{\rm ST}(M_{\rm vir}, z)\xi_{\rm lin}(r, z) \tag{2.2}$$

is the two-halo term that depends on the bias, $b_{\rm ST}$, around the lens halo computed as in Sheth and Tormen (1999) and $\xi_{\rm lin}$ is the linear matter-matter correlation function at a three-dimensional distance, r, computed from the linear power spectrum at redshift z.

Equation 2.1 (labeled “G18”) is plotted as the orange dashed curve in Figure 2.4. There, we designate $\delta_{\rm los} = 1$ since the structure found in the volumes of all three simulations tend to be well represented by the halo mass function (refer to Figure 2.1). Notice that in the region $\ell = [2-5]R_{\rm vir}$, counts in the simulation are in excess of the G18 estimate. This excess likely originates from subhalos with orbits that have apocenters beyond $R_{\rm vir}$. This “backsplash" population can be substantial just outside of $R_{\rm vir}$, as 50-80% of halos at $r \in [1-1.5]\,R_{\rm vir}$ were once subhalos (e.g. Gill et al. 2005, Garrison-Kimmel et al. 2014) and therefore represent a natural continuation of the subhalo population within $R_{\rm vir}$[6]. A physical boundary for this virialized population of halos is the so-called “splashback" radius of the host (More et al. 2015), where recently-accreted material reaches its second apocenter (or the first apocenter after turn-around, where the turn-around – or infall – radius is $R_{\rm infall} \approx 1.4\,R_{\rm sp}$). Our sample of lens-mass halos at $z = 0.2$ should have a median splashback radius of $R_{\rm sp} \approx 1.5R_{\rm vir}$ (More et al. 2015). Subhalos outside of $R_{\rm vir}$ but within $R_{\rm sp}$ ($\ell \approx 3R_{\rm vir}$), and accompanying halos on first infall ($r < R_{\rm infall} \approx 2.1\,R_{\rm vir} \leftrightarrow \ell 4.2\,R_{\rm vir}$) therefore provide a natural explanation of the excess relative to G18 at $\ell = [2-5]R_{\rm vir}$. Notably, the G18 model matches our simulation results for $\ell > 5R_{\rm vir}$, similar to the radius at which Garrison-Kimmel et al. (2014) find the backsplash fraction is essentially zero.

To accommodate the excess clustering seen within $5R_{\rm vir}$, we modify Equation 2.1 as

$$\frac{d^2N_{\rm CDM}}{dm\,dV} = \delta_{\rm los}\left[1 + \xi_{\rm 2halo}(r, M_{\rm vir}, z) + b_{\rm sp}(r)\right]\,\frac{d^2N_{\rm ST}}{dm\,dV}\,, \tag{2.3}$$

where

$$b_{\rm sp}(r) := b_e\left(\frac{r}{5R_{\rm vir}}\right)^{-s_e}\,. \tag{2.4}$$

Here b_e and s_e are free parameters, and the term in parentheses accounts for the excess clustering (compared to Equation 2.1). Equation 2.3 explicitly separates the contribution of the cosmologically

[6]A backsplash excess is also hinted at pictorially in Figure 2.3 (top panel) from the magenta dots in the (edge-on) lens-centered projection

average LOS halos, an enhancement from halo-halo clustering, and a further enhancement from backsplash halos. The implied LOS count with this parametrization is shown as the black-dashed curve in Figure 2.6 with $b_e = 0.1$ and $s_e = 4$. This choice of parameters captures our results to an accuracy of 10% all the way out to the edge of the simulation box. In particular, our parametrization is what we would expect for a population of virialized (sub)halos that populate between distances of $R_{\rm vir}$ and $5R_{\rm vir}$

2.4.3 Cumulative counts

In order to estimate sample size of suitable lenses needed for testing predictions, it is useful to know how many low-mass halos, on average, we expect to see along the LOS to a host. The lower the expected count per lens, the more lenses we will need to place meaningful constraints on the halo mass function at low masses. The average count will depend, of course, on the redshift of the target galaxy and lens relative to the observer (e.g. Despali and Vegetti 2017) but our results allow us to determine the average count within the $\sim$ 100 Mpc vicinity of the lens. Broadly speaking, the closer the lens to the observer, the more important correlated structure will be. *The results that follow will be important for any lens where the substructure contribution is significant compared to the total expected count of perturbers.* This is the case for roughly half of the lenses in the Despali and Vegetti (2017) sample, for example.

Figure 2.7 shows the mean count of halos along the projected lens-centered cylinder as a function of cylinder length ℓ, where the mean cumulative counts, $\langle N(<\ell)\rangle$, is related to the average rate of counts by

$$\langle N(<\ell)\rangle = \int_0^\ell d\ell' \left\langle \frac{dN}{d\ell'} \right\rangle . \tag{2.5}$$

Following the presentation of Figure 2.4, for increasing ℓ, the simulation results fully realize the expected clustering contribution to the LOS halo count once integrating the solid lines out to the

cosmological boxes.

Solid lines in Figure 2.7 show the integrated mean count of halos more massive than $10^9\ M_\odot$ within cylinders of length ℓ centered on lens hosts from TNG100 (magenta) and TNG100$_{\rm DM}$ (cyan). The gray vertical line marks the cylinder length at the halo boundary ($\ell = 2R_{\rm vir}$). As we can see by comparing TNG100 and TNG100$_{\rm DM}$ at $\ell < 2R_{\rm vir}$, subhalo counts are reduced by ≈ 40 in the full-physics run compared to the DMO run. This result is consistent with the findings of Despali and Vegetti (2017) and Graus et al. (2018). A second takeaway from Figure 2.7 is that the average count of halos is much less than unity out to the edge of the box. This means that most of the lens-centered LOS cylinder *do not* contain halos larger than $10^9\ M_\odot$within within 100 Mpc in projections of radius $\mathcal{R} = 10$kpc. We find that for TNG100$_{\rm DM}$, 87.5% of projections contain no halos at this mass limit. For TNG100, the fraction of empty projections rises to $\approx 92.5\%$.

The dashed and dotted lines in Figure 2.7 compares our simulation results to alternative ways of estimating cumulative counts beyond the host halo virial radius. The first assumes that halo counts are equal to the universal average (estimated via Sheth and Tormen 2002) for all radii beyond the virial radius of the lens (dotted lines) and the second uses the estimate from G18, which models local clustering as in Equation 2.1. We see that if we assume the average background is achieved for radii beyond the virial radius, the cumulative count at 100 Mpc is underpredicted by $\sim 20\%$ in TNG100 and $\sim 15\%$ in TNG100$_{\rm DM}$. Differences between the simulations and the G18 estimate are not as large, with $\approx 5\%$ offsets in TNG100$_{\rm DM}$ and TNG100 at 100 Mpc. Note that when using the G18 formula, we set $\delta_{\rm los} = 1$ for TNG100$_{\rm DM}$ and $\delta_{\rm los} = 0.879$ for TNG100. The latter value is below unity because the average differential count is slightly below the Sheth and Tormen (2002) estimate at large ℓ (see the magenta vs. dotted lines at > 40 Mpc in Figure 2.6). This factor is also introduced for the average background interpolation. We provide a more thorough discussion on how the contribution of the clustering component to quantifying the LOS structure of TNG100 in later in this section, while TNG100$_{\rm DM}$ results are discussed in Section 2.6.

Figure 2.8 displays the mean cumulative counts for FIREbox$_{\rm DM}$ subhalos of $M_{\rm halo} > 10^8\ M_\odot$ and

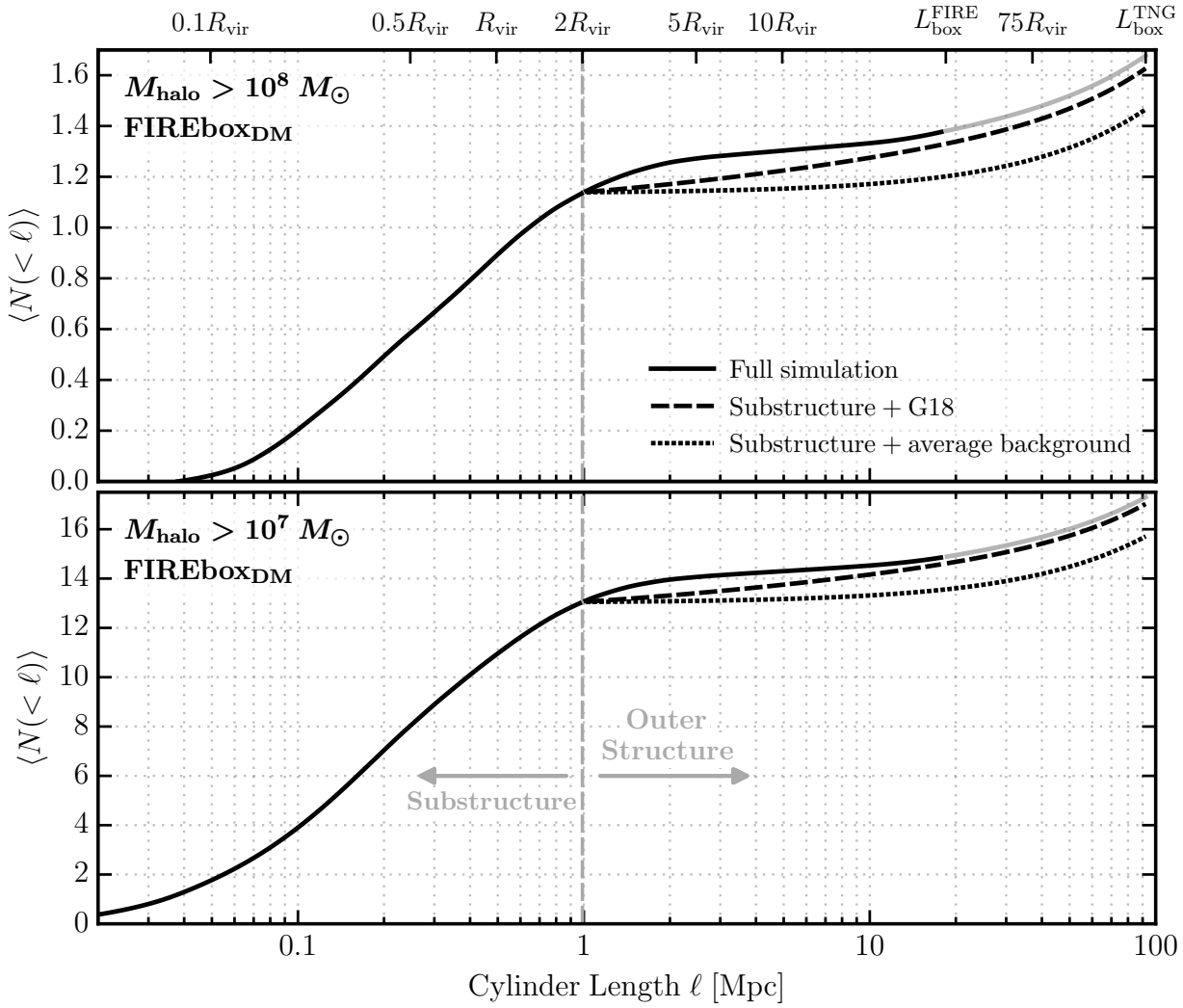

Figure 2.8: Similar to Figure 2.5, but now for FIREbox$_{\rm DM}$ halos with $M_{\rm halo} > 10^8\ M_\odot$ (top) and $M_{\rm halo} > 10^7\ M_\odot$ (bottom). Both curves (top and bottom panels) incorporating the G18 model use $\delta_{\rm los} = 1$. The typical LOS passing through a lensing host encounters significantly more perturbers above a given mass as the perturber mass threshold is lowered.

$M_{\rm halo} > 10^7\ M_\odot$ in the top and bottom panel, respectively. The likelihood of finding a halo in a single projected cylinder increases substantially at these lower masses compared to the $10^9\ M_\odot$. Specifically, we expect to see, on average, more than one small halo per LOS for $10^8\ M_\odot$ and more than 15 for $10^7\ M_\odot$.One caveat here is that these simulations do not include the destructive effects of a central galaxy. We would expect substructure to be depleted within $\ell \approx 1$ Mpc by approximately 40% if the destruction mirrors that seen in Figure 2.5 for $M_{\rm halo} > 10^9\ M_\odot$ halos.[7]

The line styles in Figure 2.8 mimic those in Figure 2.7, with solid lines representing the full simulation results. The line is extrapolated beyond the edge of FIREbox$_{\rm DM}$ (gray solid line) by assuming it follows the G18 estimate starting at $L_{\rm box}^{\rm FIRE}$ with $\delta_{\rm los} = 1$ for both mass cuts. We have also modeled the entire solid line using Equation 2.3 instead of the simulation results to test whether the relatively small box of FIREbox$_{\rm DM}$ suppresses large-scale modes, thereby affecting the number of halos found from $\ell = 5R_{\rm vir}$ out to $L_{\rm box}^{\rm FIRE}$. Doing so, we find very little difference in the final results. The assumption of average background to the simulation results out to $L_{\rm box}^{\rm TNG}$ results differ to about 15% for $10^8\ M_\odot$ while 10% for $10^7\ M_\odot$.

It is important to quantify the contribution of correlated clustering to counts for $\ell > 2\,R_{\rm vir}$, i.e., when subtracting off the contribution of subhalos to $N(<\ell)$, what is the fractional contribution of the population of clustered halos compared to the average halo population at $\ell > 2\,R_{\rm vir}$? This is explicitly address in Figure 2.9, which shows the total average cumulative count of $10^9\ M_\odot$ halos in TNG100 for cylinder lengths ranging from the edge of the virial radius to the edge of the box. We plot the average count $\langle N(<\ell)\rangle$ in units of the average cumulative count from subhalos $\langle N_{\rm sub}\rangle \equiv \langle N(\ell < 2R_{\rm vir})\rangle$, where $\langle N_{\rm sub}\rangle = 0.072$. The full count from the simulation (labeled as "total") is shown by the magenta curve while cylinders that are assumed to have the average background outside of the virial radius (labeled "average") are plotted as the light gray curve. To quantify the excess clustering associated beyond substructure, we take the difference between

[7]Recently, Kelley et al. (2019) presented high-resolution zoom simulations for MW-mass DMO halos while accounting for the central galaxy and found that the depletion of substructure is about roughly the same factor for halos down to $10^7\ M_\odot$ at $z = 0$. While we are drawing possible conclusions from MW-mass halos, this scaling could translate to our lens-mass halos.

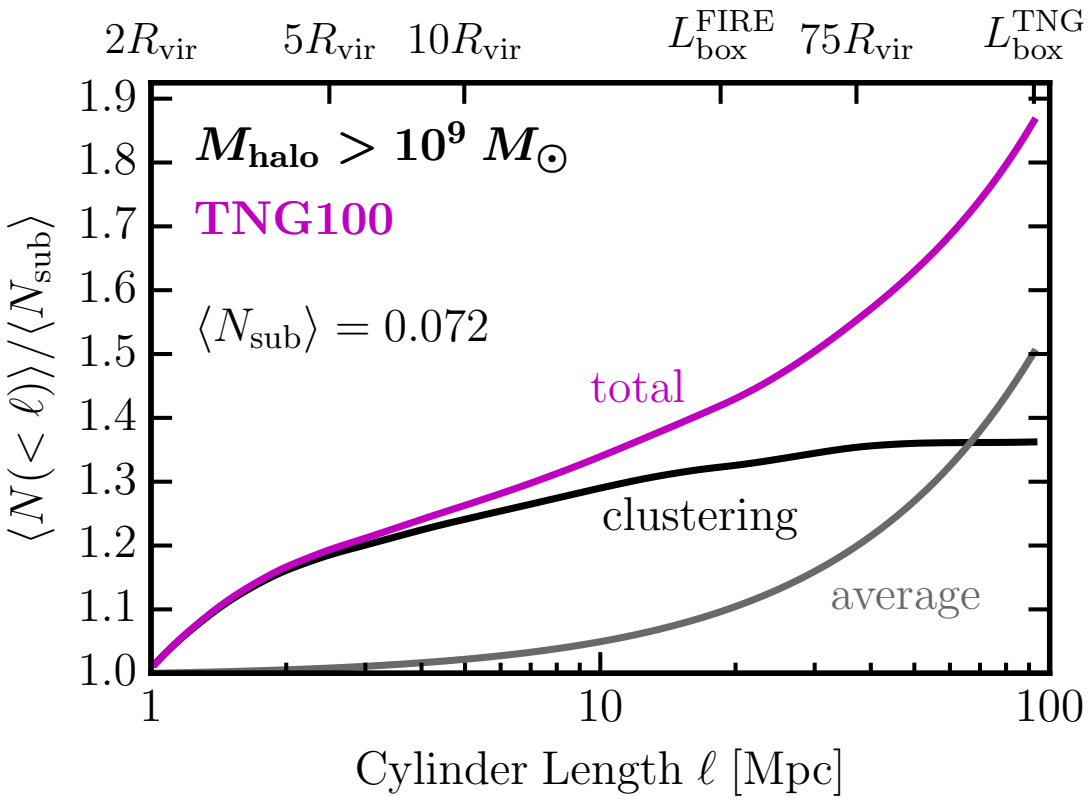

Figure 2.9: *Boost in counts from local clustering*: The mean count of LOS halos more massive than $10^9\ M_\odot$ within lens-centered cylinders from TNG100 relative to the mean count within the virial radius $\langle N_{\rm sub}\rangle \equiv \langle N(\ell < 2\,R_{\rm vir})\rangle$ is presented here. The magenta line shows the mean total count from the simulation (labeled "total"), while the gray line shows counts in cylinders that assume the density of halos matches the mean background (dubbed "average") for $\ell > 2\,R_{\rm vir}$. The black line shows the difference between the "total" and "average" contributions; this is the component that is attributable to local halo clustering (dubbed "clustering"). We see that the local clustering effect provides a boost of $\sim 35\%$ compared to the subhalo count alone and that this contribution dominates the "average" contribution out to ~65 Mpc $\approx 130\,R_{\rm vir}$.

the magenta and gray curves. This results in the black curve ("clustering"). The excess clustered contribution asymptotes to $\sim 1.35\langle N_{\rm sub}\rangle$ at $\ell \approx 70$ Mpc (~75 $R_{\rm vir}$). This means that local clustering boosts the expected signal by $\sim 35\%$ compared to what we would expect from subhalos alone. We show similar results for lower mass halos in other simulations in Section 2.6. Broadly speaking, the boost from local clustering is smaller *relatively* in DMO simulations that do not have enhanced subhalo destruction from the central galaxy. Note that the clustering contribution is larger than the average contribution out to $\ell \approx 65$ Mpc, or equivalently, ~130 $R_{\rm vir}$.

2.4.4 Structure along principal axes

CDM halos have significant triaxiality (e.g. Frenk et al. 1988, Dubinski and Carlberg 1991, Warren et al. 1992, Cole and Lacey 1996, Jing and Suto 2002, Bailin and Steinmetz 2005, Kasun and Evrard 2005, Paz et al. 2006, Allgood et al. 2006, Bett et al. 2007, Muñoz-Cuartas et al. 2011, Despali et al. 2014, Vega-Ferrero et al. 2017, Lau et al. 2020), which could also mean that subhalos are found preferentially along the host's major (densest) axis (e.g. Zentner et al. 2005). This effect can qualitatively impact our analysis of lens-centered projections, especially for substructure lensing. Furthermore, it is likely that galaxy lenses are biased to be oriented with the LOS coinciding with the host halo's major axis (Mandelbaum et al. 2009, Osato et al. 2018), as this configuration produces a larger surface mass density for a fixed overall mass distribution. In order to explore the potential magnitude of this effect, we calculate dark matter halo shapes from the lens targets using the shape inertia tensor as discussed in Allgood et al. (2006). We include all dark matter particles within a shell between $10 - 20\%$ of $R_{\rm vir}$ as a conservative approach for our sample of halos. Using a shell rather than the enclosed mass minimizes the influence of particles with radii smaller than the numerical convergence scale. The resulting eigenvalues of the shape tensor are proportional to the square root of the principal axes of the dark matter distribution. We then re-do the analysis of Section 2.4, now aligning the lens-centered projections along each principal axis of the lens-mass halo.

Figure 2.10 plots the results for the average (mean) counts along each principal axis for halos more massive than $10^9\ M_\odot$ in TNG100 (for comparison with TNG100$_{\rm DM}$, see Figure 2.14). The top, middle, and bottom panels depict the average counts along the major axis, intermediate axis, and minor axis, respectively, with cylinders of radius $\mathcal{R} = 10$ kpc. For comparison, the faded solid line in each panel shows the mean counts presented previously in Figure 2.7. We see that the major axis sight-line results in measurably more halos, on average, than do other orientations. The boost along the major axis is $\sim 30\%$ compared to the random LOS, with essentially the entire contribution coming from subhalos (and backsplash halos). Along the minor axis, on the other hand, average

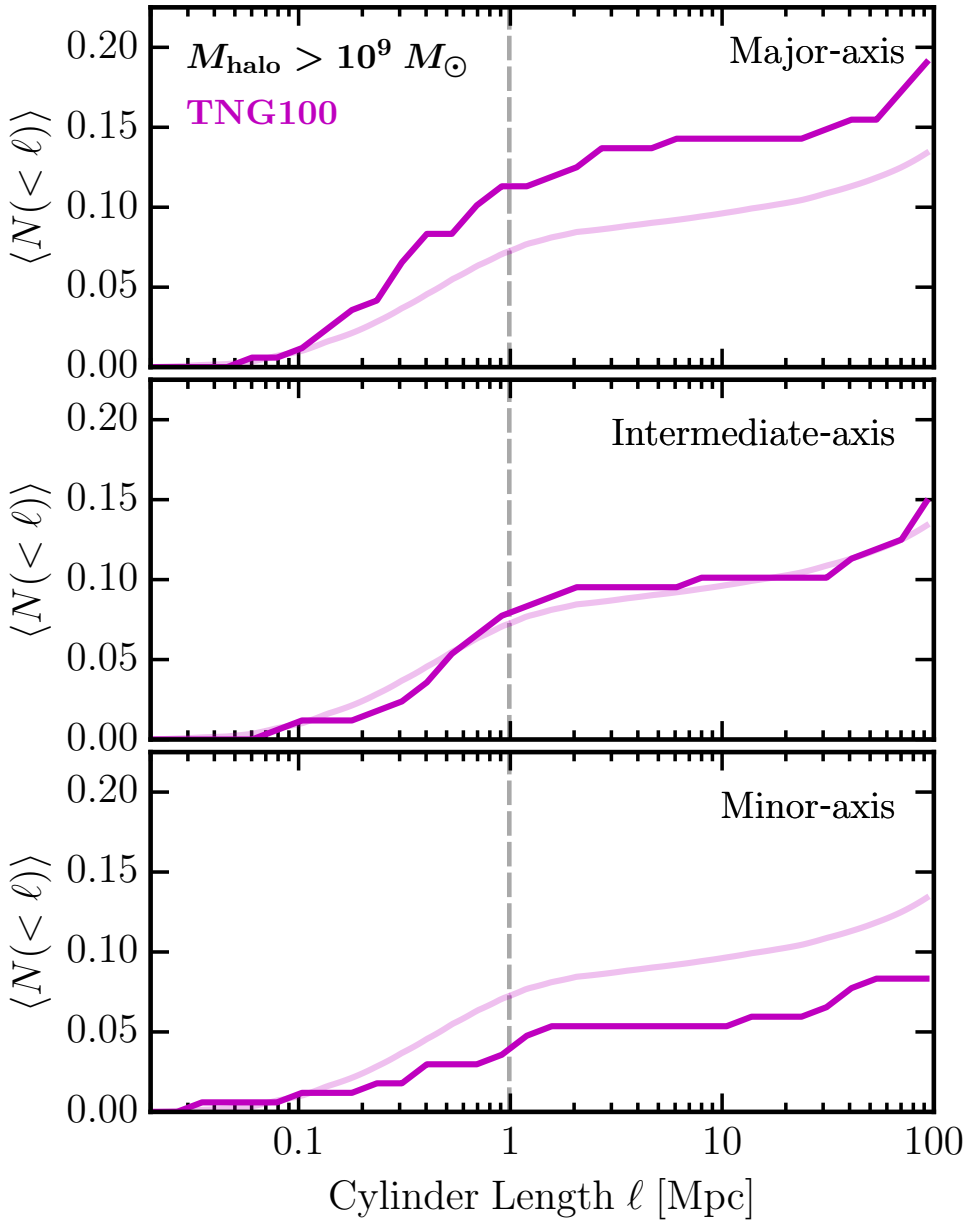

Figure 2.10: *Projections along the principal axes*: Similar presentation as Figure 2.6, but now filled solid lines show the counts for TNG100 halos $M_{\rm halo} > 10^9\ M_\odot$ along the major, intermediate, and minor axis in the top, center, and bottom panels, respectively. The transparent lines give the mean counts of the substructure with local clustering counts of TNG100 presented previously in Figure 2.7. Sight-lines oriented along the major (minor) axis of the halo result in a non-trivial increase (decrease) in the number of perturbers encountered along the sight line.

counts are significantly reduced. Projections along the intermediate-axis are comparable to the average counts shown in Figure 2.6. It is clear that lens-centered projections along the major or minor axis can non-trivially boost or decrease the lensing signals by a factor of ~ 2. This factor is also acquired for analog simulation neglecting the presence of the central galaxy and baryons (see Figure 2.14).

2.5 Nuances from counting statistics

In Section 2.4.1, we discussed the possibility that the differences in local clustering signal between $\mathrm{TNG100_{DM}}$ and $\mathrm{FIREbox_{DM}}$ could arise from sampling variance – there are only three lens-mass hosts in $\mathrm{FIREbox_{DM}}$ – rather than differences in large-scale structure (compare the red and cyan curve in Figure 2.6). In order to explore this more fully, Figure 2.11 shows $\langle dN/d\ell \rangle$ for $\mathrm{TNG100_{DM}}$ (cyan) and $\mathrm{FIREbox_{DM}}$ (red). This figure mirrors Figure 2.6 except now we are using a cylinder radius with the size of the lens-mass virial radius ($\mathcal{R} = R_{\rm vir} \simeq 500$ kpc) as opposed to the typical Einstein radius ($\mathcal{R} = 10$ kpc) in order to improve counting statistics. The solid lines depict the mean of all projections while the dashed (shown only for $\mathrm{TNG100_{DM}}$) is the *median* of all projections. The cyan band encloses the $\pm 1\sigma$ of all of the individual curves around median.

For $\ell < 1$ Mpc, the median and mean curve for $\mathrm{TNG100_{DM}}$ are consistent with one another, but for $\ell > 1$ Mpc we see that the average count (which is what we plot in Figure 2.6) sits well above the median. This is indicative of a highly non-Gaussian distribution, with a tail skewed towards large fluctuations, as expected for non-linear dark matter structure. Specifically, rare (high-count) events drive the average higher than the median. If this is the case, we require a large number of realizations in order to sample enough of the distribution to capture the true average. As further evidence that sample variance is the cause of the differences in local clustering signal between $\mathrm{TNG100_{DM}}$ and $\mathrm{FIREbox_{DM}}$, the median line in Figure 2.11 falls *below* the average background (black dashed) at $\ell \approx 10$ Mpc. This is due to a large number of null counts.

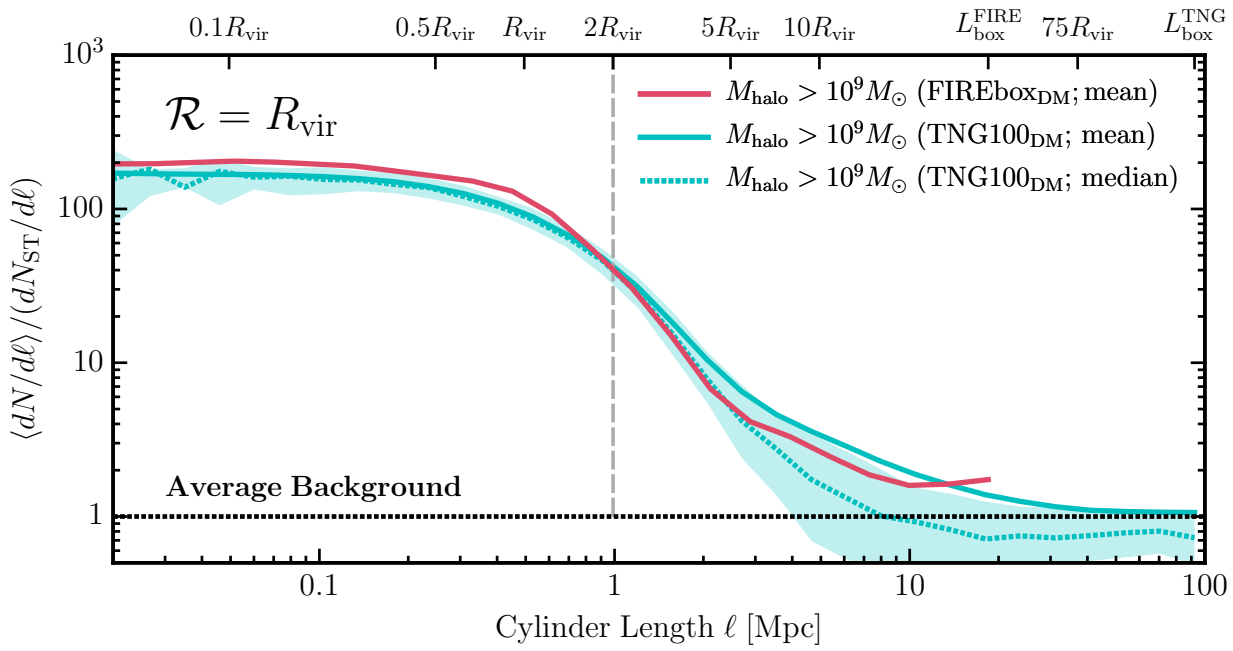

Figure 2.11: Analogous to Figure 2.4, now with results of TNG100$_{\rm DM}$ (cyan) and FIREbox$_{\rm DM}$ (red) for $M_{\rm halo} > 10^9\ M_\odot$ for cylinders with a radius size comparable to the lens mass halo ($\mathcal{R} = R_{\rm vir}$) as opposed to the lens halo's Einstein radius ($\mathcal{R} = 10\,$kpc). The solid curves depict the *mean* differential count while the dashed cyan is the *median* differential count for TNG100$_{\rm DM}$. The cyan band encloses the $\pm 1\sigma$ region of the curves. The median counts fall below the mean counts, indicating that the mean counts are strongly affected by rare, high-count orientations.

Though the *average* count from FIREbox$_{\rm DM}$ falls below the average line from TNG100$_{\rm DM}$, we see that it falls within the 1σ band about the *median*. Given that we only have three host halos in our sample, this would not be unexpected even if the halos were sampling the same large-scale structure field. Naively, there is a $\sim 30\%$ chance that three randomly drawn distributions will lie within 1σ of the median. Given that we only have three host halos, we conclude that the observed result is consistent with small-number statistics.

2.5.1 Choice of cylinder radius

The conclusions made in the results protion of this chapter are based on the average number density of subhalos within a project cylinder radius of 10 kpc, which is comparable to the typical Einstein ring of our 10^{13} $M_\odot$ lens-mass halos. The choice of $\mathcal{R} = 10\,$kpc could bias our results towards higher substructure, and potentially, LOS halo counts, as massive galaxy lenses typically have Einstein ring radii of ~ 5 kpc (Bolton et al. 2008).

In Figure 2.12, we demonstrate how the selection of smaller lens radii does not impact the trends discussed in our main analysis. Both the top and bottom plot mirrors exactly Figure 2.6, now with the top and bottom plot showing results for a projected radius of 5 and 2 kpc, respectively. We find that we are able to mostly recover the same trend seen for the 10 kpc projected radius from Figure 2.6 for both $\mathcal{R} = 5$ and 2 kpc. In the 5 kpc radius projection, the curves are more noisier than the 10 kpc owing to the increasing fraction of projections with zero halos. We would argue that the $\mathcal{R} = 5$ kpc size projections have comparable trends to the $\mathcal{R} = 10$ kpc case. Out to $\ell = 5R_{\rm vir}$, most of the mean differentials drives faster down to the average compared to the 10 kpc case, but we suspect this is owed to low number statistics along with the sampling variance for TNG100$_{\rm DM}$ (see discussion in Section 2.5). This becomes more apparent for the smaller projected radius of 2 kpc, as the fraction of projections of zero halos increases appreciably. Note that the $M_{\rm halo} > 10^9$ $M_\odot$ result is impacted greatly by sampling variance the low number of halos along the LOS.

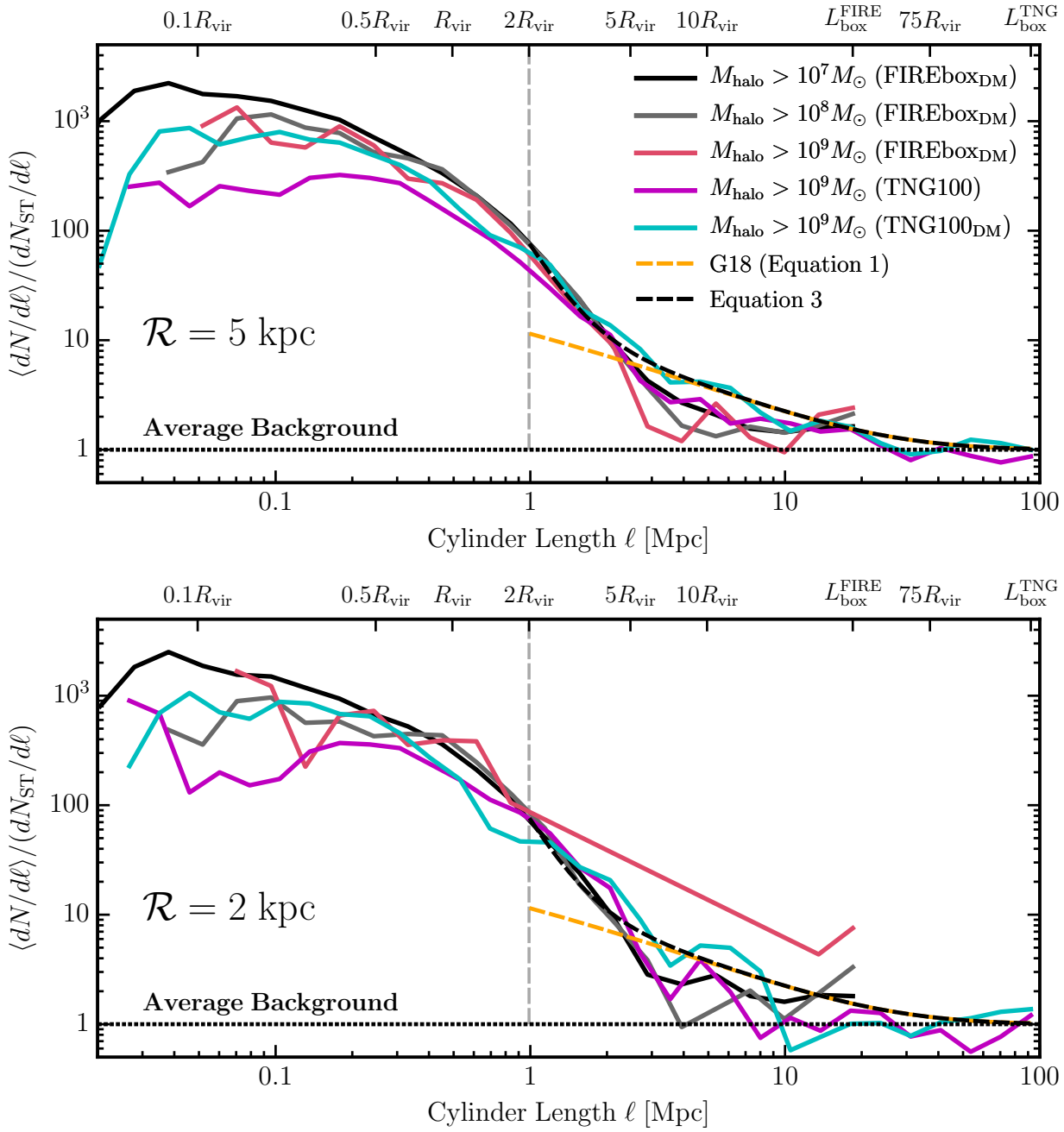

Figure 2.12: Analogous to Figure 2.6, now for cylinders with a radius size $\mathcal{R}$ = 5 kpc and a much smaller annulus $\mathcal{R}$ = 2 kpc. While the curves are much noisier as the radius size becomes smaller (owing to the increased fraction of null sight lines), the we are able to recover the same trend for the differential counts seen for a projected radius of $\mathcal{R}$ = 10 kpc.

2.6 Supplementary discussion with dark matter only physics

This section presents the DMO results from TNG100$_{\rm DM}$ and for FIREbox$_{\rm DM}$and provides additional elaboration of the results presented in Section 2.4. Section 2.6.1 picks up from later discussion of Section 2.4.3 and Section 2.6.2 picks up from Section 2.4.4.

2.6.1 Clustering contribution to the line-of-sight population

Figure 2.13 presents the contribution of the simulated clustering to the LOS halo population in TNG100$_{\rm DM}$ and FIREbox$_{\rm DM}$. Namely, the top, middle, and bottom panels plots the subhalo populations based on the lower-mass cuts of $10^9\ M_\odot$, $10^8\ M_\odot$, and $10^7\ M_\odot$, respectively. The colored curves, labeled "total", are the actual results of the simulation out to the box using our method discussed in the main text. The average background expectation for halos above the low-mass cuts in each panel is depicted by the grey curves. The clustering contribution from the simulations, labeled "clustering", are plotted as the black curves, which is the difference between the "total" curve and "average" curves. Like before, all results are normalized by the $\langle N_{\rm sub}\rangle$ quantified from out lens-mass sample. Since the actual FIREbox$_{\rm DM}$ results extend out to $L_{\rm box}^{\rm FIRE}$, we extrapolate the curves out to $L_{\rm box}^{\rm TNG}$using Equation 2.1 (using Equation 2.3 is also equally adequate).

Starting with the counts $10^9\ M_\odot$ (top panel), clustering acts as the most contributing component to the LOS halo population until the average background takes over at $\ell \approx 75R_{\rm vir}$ (or $r \approx 37.5$ Mpc) for TNG100$_{\rm DM}$ (cyan curve). As a comparison check, we plotted the FIREbox$_{\rm DM}$ results of $10^9\ M_\odot$ (thin blue curve) and find minimal difference in results. Note the clustering component is determined from TNG100$_{\rm DM}$ and not FIREbox$_{\rm DM}$. The clustering component in TNG100$_{\rm DM}$ boosts about $1.5\langle N_{\rm sub}\rangle$ out until the average background takes over at $\ell \approx 70$ Mpc (or $r \approx 35$ Mpc). This is less significant than the TNG100 in the main text, the clustering component strongly boosts the number of LOS halos to about $1.7\langle N_{\rm sub}\rangle$ until the average background takes over.

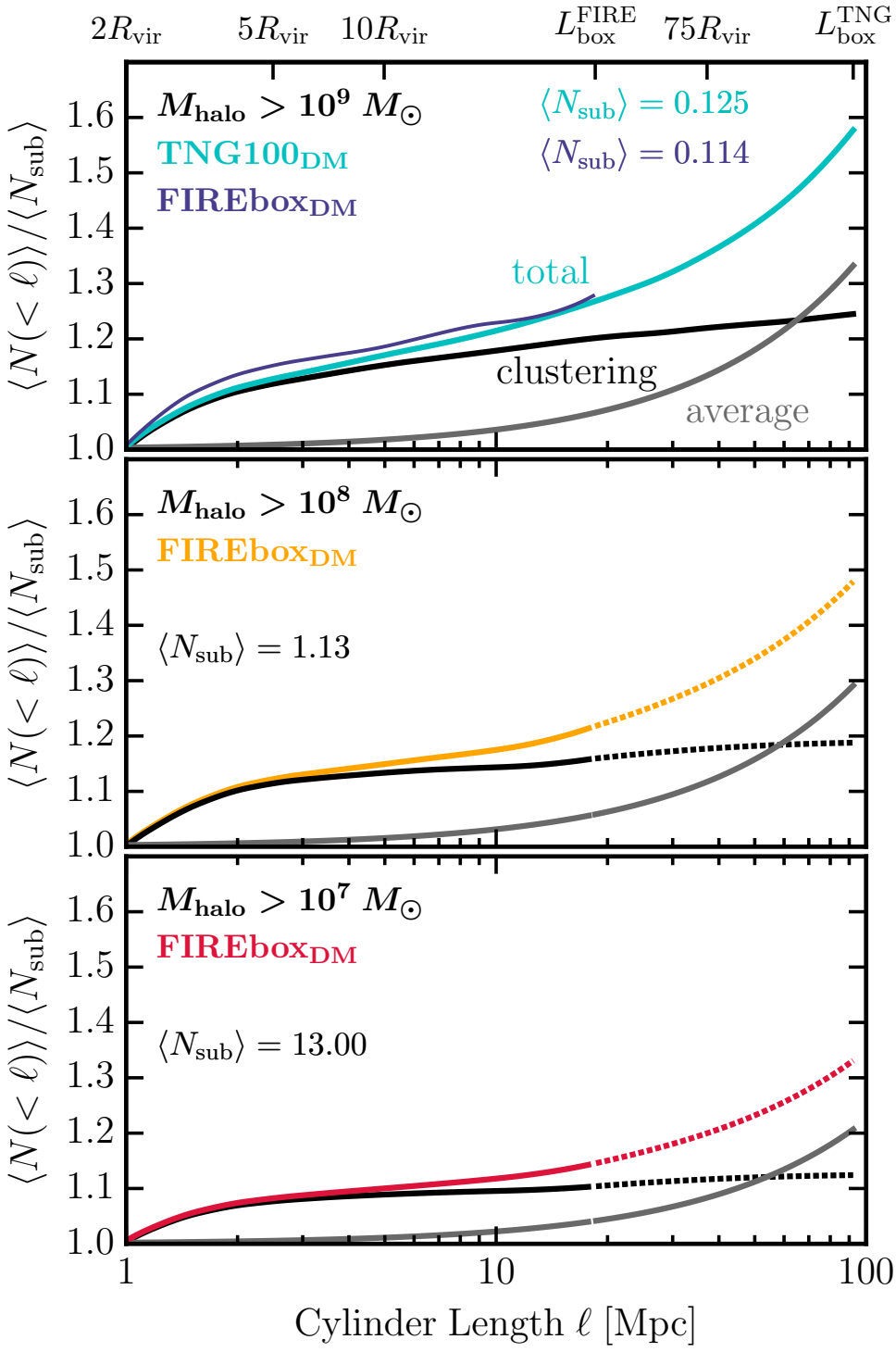

Figure 2.13: Like Figure 2.9, now showing only the results for TNG100$_{\rm DM}$ and FIREbox$_{\rm DM}$. In the top panel, the black and gray curve are computed based off of the total counts from TNG100$_{\rm DM}$ (cyan curve). As a comparison, the blue curve shows the total counts from FIREbox$_{\rm DM}$ out to $L_{\rm box}^{\rm FIRE}$. The middle and bottom panel are presented similarly with their curves extrapolated out to the $L_{\rm box}^{\rm TNG}$ using Equation 2.3.

As we go further down to the low-mass cuts of the subhalo populations, the contribution from correlated clustering becomes much weaker for decrease mass. For $M_{\rm halo} > 10^8$ $M_\odot$ (middle panel), the clustering component boosts the number of LOS halos to only about $\sim 1.2\langle N_{\rm sub}\rangle$ until the average background takes over at about $\ell \approx 60$ Mpc (or $r \approx 30$ Mpc). The clustering component for $M_{\rm halo} > 10^7$ $M_\odot$ (bottom panel) becomes weaker by only boosting the number of LOS halos to only about $\sim 1.1\langle N_{\rm sub}\rangle$ until the average background takes over at $r \approx 30$ Mpc). In order to conclude with more robust predictions, a larger sample lens-mass halos in comparable cosmological environments is needed to reduced the uncertainty possibly found in $\langle N_{\rm sub}\rangle$ for these low-mass halos.

2.6.2 Structure along principal axes

Figure 2.14 plots the mean subhalo counts as seen from lens-centered projections along the principal axis of the TNG100$_{\rm DM}$ lens-mass halos. The axes were computed using the method detailed in Section 2.4.4. Shown are only the results from TNG100$_{\rm DM}$ since these cosmological volumes have enough lens-centered mass halos to provide enough statistics since each halo has only three principal axis to orientate on. Moreover, FIREbox$_{\rm DM}$, while useful for simulating 10^{7-8} $M_\odot$ halos in cosmological environment, has only three lens-centered hosts, which will not provide adequate statistics to present. Though, we find similar trends. The top, middle, and bottom panels depict the average counts along the major-, intermediate-, and minor-axis, respectively. For comparison, the faded solid line in each panel plots the mean counts presented previously in Figure 2.7. We again see that projections along the major-axis of DMO lens-mass halos, subhalos tend to populate on the densest principal axis. This effect is more dramatic for the substructure compared to the TNG100 shown previously, owing to the lack of a central galaxy.

Projections the size of the Einstein radius along the major-axis find around 75% of the projections to contain no substructure out to the size of the halo. Along the minor-axis, this is around $\sim$ 90%.

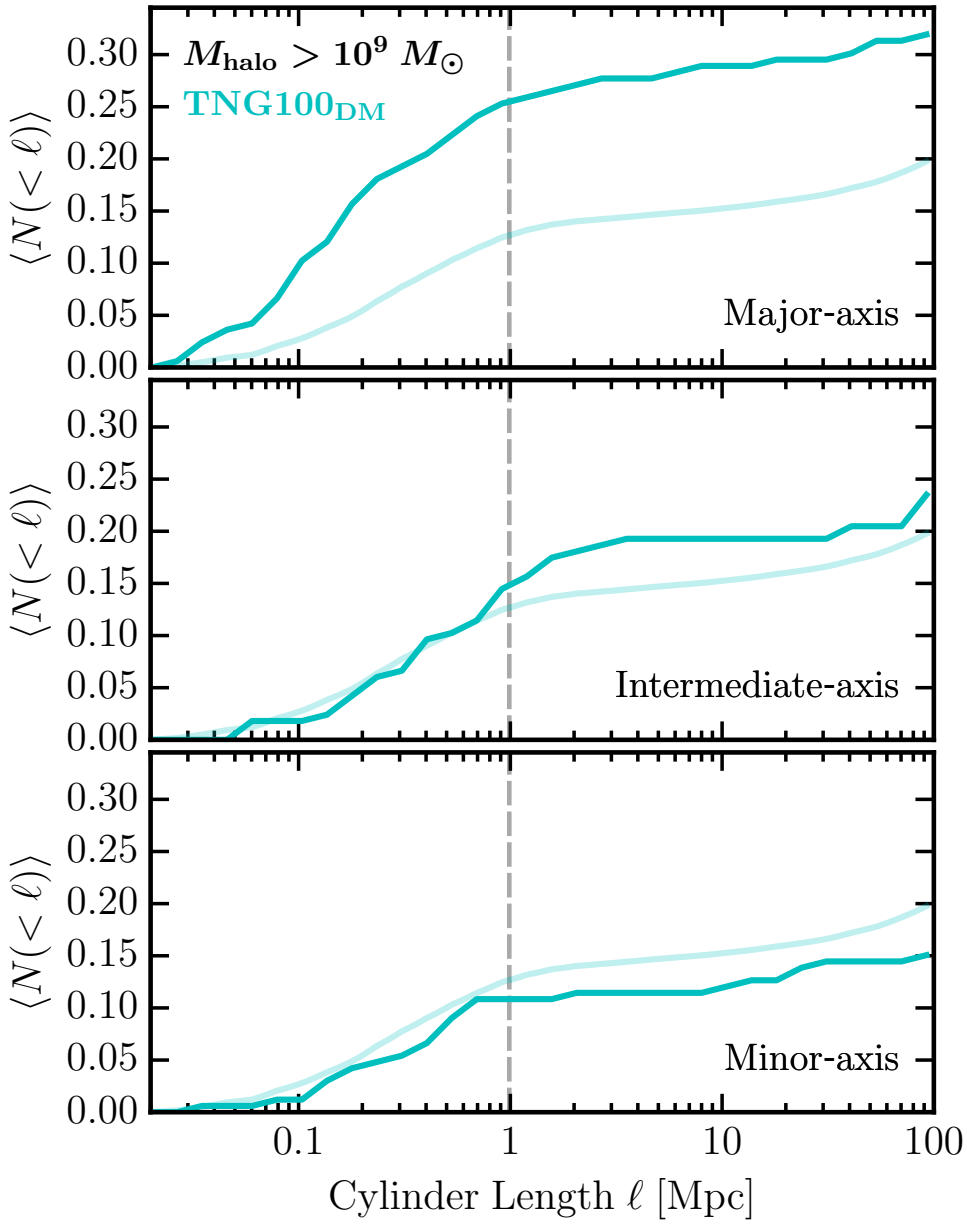

Figure 2.14: Like Figure 2.10, but now showing the TNG100$_{\rm DM}$ counts for halos $M_{\rm halo} > 10^9\ M_\odot$ along the major, intermediate, and minor axis in the top, center, and bottom panels, respectively. Plotted for comparison, the transparent lines are the mean counts of the substructure with local clustering counts for TNG100$_{\rm DM}$ presented previously in Figure 2.7.

Additionally, the substructure counts appear to be almost comparable to the mean from Figure 2.6, though slightly less. Done on the intermediate-axis, this results in counts somewhat comparable to the mean counts, though we see ∼5% boost in the LOS component.

2.7 Summary and concluding remarks

Using the set of TNG100 and DMO FIREbox$_{\rm DM}$ cosmological simulations, we quantify the effect of local clustering on gravitational lensing searches for low-mass dark matter halos. We specifically focus on lens-mass halos of mass $M_{\rm vir} \simeq 10^{13}\ M_\odot$ at $z = 0.2$ as prime targets for future lensing surveys and explore counts of halos down to $M_{\rm halo} = 10^{7-9}\ M_\odot$.

Our primary result is that local clustering can boost the expected LOS perturber halo counts significantly compared subhalos alone. The signal exceeds that expected for an average background projection to distances in excess of ±10 Mpc from the lens host (Figure 2.6), with a significant excess within $2 - 5\,R_{\rm vir}$. We provide an analytic expression for this contribution (Equation 2.3), which we hope will be useful in full lensing interpretation studies.

Using full-physics TNG100 simulations (which resolve halos down to $10^9\ M_\odot$), we find that the central galaxy in lens-mass hosts depletes subhalos by $\sim$ 70% compared to dark-matter-only simulations (see Figure 2.7). This result agrees with previous studies (Despali and Vegetti 2017, Graus et al. 2018). From TNG100, the excess local clustering outside of the virial radius gives an expected count that is $\sim$ 35% higher than would be expected from subhalos alone (Figure 2.9).

Local contributions to perturber counts are also affected by halo orientation. The above results assume a random lens-orientation with respect to the observer, but if there is a bias for lenses to be oriented along the principal axis (e.g. Dietrich et al. 2014, Groener and Goldberg 2014), then the expected local count may be enhanced. Our initial exploration of this issue indicates that local projected counts are $\sim$ 50% higher when the target halo is oriented along the major axis compared

to a random orientation (Figure 2.8). This result, in turn, has implications for derived constraints on the mass spectrum of perturbers and accompanying constraints on dark matter particle properties.

The above results will be particularly important for low-redshift lenses ($z_l \sim 0.2$), such as those in the SLACS sample (Vegetti et al. 2014). For such lenses, (Despali et al. 2018) found that subhalos should contribute $\sim 30 - 50\%$ of the total perturber signal *relative* to LOS halos that neglect local clustering. With clustering included, the local (subhalo + clustering) contribution may well be comparable to $\sim 67.5\%$ of the total LOS contribution that neglect clustering (or $\sim 40\%$ of the total contribution) for some lenses, especially those with lower-redshift sources ($z_s \sim 0.6$). Taking into account any biases in lens-halo orientation is also important for these lenses, as an additional $\sim 50\%$ boost in counts from local clustering could significantly affect interpretations.

Chapter Acknowledgements

This chapter was worked to completion during the COVID-19 lock-down and would not have been possible without the labors of our essential workers. We thank Ran Li for helpful comments in improving the early version of this chapter. We are thankful to Quinn Minor and Manoj Kaplinghat for helpful discussions. The authors thank the Illustris collaboration for facilitating the IllustrisTNG simulations for public access and the FIRE collaboration for the use of the DMO FIREbox simulation for our analysis. Support came from the National Science Foundation (NSF) grant AST-1910965 and partial support from the NASA grant 80NSSSC20K1469.

Chapter 3

An analytic surface density profile for CDM halos and gravitational lensing studies

This chapter introduces an analytic surface density profile for dark matter halos that accurately reproduces the structure of simulated halos of mass $M_{\rm vir} = 10^{7-11}\,M_{\odot}$, making it useful for modeling line-of-sight perturbers in strong gravitational lensing models. The two-parameter function has an analytic deflection potential and is more accurate than the projected Navarro, Frenk & White (NFW) profile commonly adopted at this mass scale for perturbers, especially at the small radii of most relevant for lensing perturbations. Using a characteristic radius, R_{-1}, where the log slope of surface density is equal to -1, and an associated surface density, Σ_{-1}, we can represent the expected lensing signal from line-of-sight halos statistically, for an ensemble of halo orientations, using a distribution of *projected concentration* parameters, $C_{\rm vir} := r_{\rm vir}/R_{-1}$. Though an individual halo can have a projected concentration that varies with orientation with respect to the observer, the range of projected concentrations correlates with the usual three-dimensional halo concentration in a way that enables ease of use.

3.1 Chapter context

The ΛCDM (the cosmological constant + cold dark matter) cosmogony has served as the benchmark model for decades. A major component of its success is in matching the large-scale structure of the Universe, which also places principal constraints on the Universe's composition (e.g. Davis et al. 1985, Geller and Huchra 1989, Bond et al. 1996, Tegmark et al. 2004, Sánchez et al. 2006, Weinberg et al. 2013). A key prediction of ΛCDM is that the Universe is lavished with a high number density of very low-mass ($M_{\rm halo} \lesssim 10^9\ M_\odot$) dark matter halos that can act as perturbers in lensing studies (Press and Schechter 1974, Green et al. 2005, Diemand et al. 2007, Springel et al. 2008, Frenk and White 2012). The existence of very low mass, nearly starless, dark halos of the kind and character predicted have yet to be confirmed by observations and may only be detectable via their gravitational effects, e.g., on strong gravitational lenses.

While the cosmological model of ΛCDM has been successful at matching large-scale observations, ΛCDM still suffers from discrepancies found at small scales (see Bullock and Boylan-Kolchin 2017 for a comprehensive overview) and this has motivated alternative dark matter models. One such model is warm dark matter (WDM), which suppresses the matter power spectrum of initial density perturbations at scales smaller than the free-streaming length (Colín et al. 2000, Bode et al. 2001, Lovell et al. 2012, Schneider et al. 2012). As an example, a 7 keV sterile neutrino of the type that could be responsible for the observed 3.5 keV line in galaxy cluster X-ray spectra (e.g. Boyarsky et al. 2014, Bulbul et al. 2014), would produce a sharp cutoff off in the abundance of halos smaller than $M_{\rm halo} \lesssim 10^8\ M_\odot$. Demonstrating the existence of halos below this mass could rule out this class of WDM; conversely, the ability to rule out such a population would eliminate ΛCDM as a complete model of cosmology. One other prediction for galaxies in a WDM cosmology is that they form with lower central densities compared to ΛCDM (Lovell et al. 2014). It is also possible that dark matter particles interact among themselves within a hidden sector (Feng et al. 2009). If self-interaction cross-sections are high enough, low-mass dark matter halos have lower central densities compared to that of ΛCDM (Rocha et al. 2013, Elbert et al. 2015, Tulin and Yu 2018). For

dark matter halos of a given mass, all of these alternative cosmological paradigms make distinct predictions for both the abundance and central densities compared to expectations of ΛCDM.

Regardless of the cosmological model, a common characteristic of low-mass dark matter halos is that they are extremely inefficient at forming stars and are nearly devoid of baryons (e.g. Sawala et al. 2016, Benitez-Llambay and Frenk 2020). This results in these objects being too difficult to detect electromagnetically. A more promising route for their detection is via gravitational perturbations of strongly lensed images (Dalal and Kochanek 2002, Moustakas and Metcalf 2003, Koopmans 2005, Vegetti and Koopmans 2009a,b, Vegetti et al. 2010, 2012, Hezaveh et al. 2016, Nierenberg et al. 2020, Gilman et al. 2020a, Hsueh et al. 2020). To fully constrain the nature of the dark matter using strong lensing, it is necessary to know the expected number of halos in ΛCDM and other cosmology models. It is convenient to characterize low-mass halo perturbers as either subhalos embedded within the main lens halo or field halos that are not part of the main lens but rather lie in projection near the lens' Einstein radius. In the strong lensing literature, this population of field halos are typically called "line-of-sight" (LOS) halos (or LOS perturbers). Recent work has shown that the LOS component contributes significantly more to strongly lensed signals. Within ΛCDM, Li et al. (2017) found that that LOS halos dominated the subhalo signal by a factor of 3-4. A similar result was found in Despali et al. (2018), where the number of LOS perturbers compared to subhalo perturbers ranges from three to ten times depending on the lens configuration. Similar results are found in Gilman et al. (2019), He et al. (2022), and in the contents within Chapter 2 (Lazar et al. 2021).

The internal structure of dark matter halo perturbers can greatly impact their lensing effect. Specifically, in order to properly constrain the mass function predicted by ΛCDM, the surface density profiles of the dark matter halos of interest must be precisely known (e.g., Minor et al. 2017, 2021b). A common way to characterize low-mass dark matter halo structure for perturbing, field (LOS) halos is to assume that they follow spherically-symmetric NFW profiles (Navarro et al. 1997, Nierenberg et al. 2017, Gilman et al. 2018, He et al. 2022). The implied surface-density profile

(and associated lensing properties) is more straightforward to work with (Wright and Brainerd 2000) and enables fast and theoretically-motivated analysis. With this assumption, the expected distribution of NFW concentration parameters at fixed mass becomes an important input for models (e.g. Gilman et al. 2022).

The spherical NFW profile is seen to be simpler analytically, which has an advantage that enables direct connection with theoretical predictions, especially for low-mass halos where feedback is believed to be less important in altering the density structure compared to dark-matter-only predictions (e.g. Lazar et al. 2020). Additionally, the NFW form also has a fairly easy-to-use surface-density profile for lensing-based analysis (Wright and Brainerd 2000). However, there are some potential shortcomings in this approach. One is that dark matter halos are not perfectly spherical and tend to be more triaxial (e.g. Frenk et al. 1988, Cole and Lacey 1996, Allgood et al. 2006). This means that, even for a halo with a spherically-averaged profile that is well described by an NFW fit, its surface density could well be different from the two-dimensional projection inferred by the spherical-average fit depending on its orientation. Second, it is well known that dark-matter-only simulations produce halos that are better modeled using the Einasto (1965) profile than NFW when the particle resolution is increased (Wang et al. 2020), however, transforming that equation into the projected two-dimensional density and the lensing signal results in a relatively complicated expression (Retana-Montenegro et al. 2012) and can be better approximated (Dhar and Williams 2010, Dhar 2021).

The aim of the work in this chapter is to provide an easy-to-use surface-density profile that accurately reproduces the structure of simulated dark matter halos in any projection. Below we show with regression analysis that the projected density profiles of simulated dark matter halos deviate from the projected NFW profile inferred from their three-dimensional, spherical NFW fits (i.e., their best-fit fit concentrations and normalization) in ways that do not average out over all orientations. This is particularly true at projected radii smaller than the scale radius. Since the NFW form is commonly used for substructure lensing analysis, this motivates the exploration of an alternative approach that

is just as easy to use and more accurate. The projected profile presented below has a scale radius and a corresponding "projected concentration". This projected concentration can account both for the fact that individual halos have different projected density profiles depending on their orientation with respect to the observer and that, at fixed halo mass, there is an intrinsic halo-to-halo (spherical) concentration scatter. While this chapter focuses on circularly-averaged projected densities on the sky, but the functional form can be easily generalized to elliptically-averaged profiles with one additional parameter, which would be a natural extension of this work.

This chapter is structured as follows. Section 3.2 introduces the suite of high-resolution simulations of dark matter halos used, provides a description of the selected sample of halos, and details the methods of constructing the radial dark matter profiles of each sampled halo. Section 3.3 provides the main results of this paper and introduces our simple fitting formula for LOS perturbers for lensing analysis. We discuss the implications for our fitting formula in Section 3.6 and demonstrate its impact to the commonly used LOS perturber formula, the NFW profile. Finally, we summarize out results in Section 3.7.

3.2 Methodology

This chapter acts as the first iteration of work focused on robustly characterizing ΛCDM predictions for substructure lensing studies. We use "zoom-in" *dark matter only* (DMO) simulations to study halo surface density structure at high resolution, focusing on isolated dark matter halos within the mass range that is applicable to substructure lensing, $M_{\rm halo} \in 10^{7-11}\,M_{\odot}$, at a characteristic redshift of $z = 0.2$. We use these simulations to discover an accurate surface density profile shape and to compare the shape parameters to the three-dimensional profile parameters of the same halos. We plan to follow-up with an analysis that utilizes a high-resolution cosmological environment (i.e., a cosmological box) to put the results presented here in a proper statistical setting and to explore redshift dependence.

3.2.1 Numerical zoom-in simulations

All of our simulations use the multi-method code GIZMO (Hopkins 2015). The initial conditions were calculated using MUSIC (Hahn and Abel 2011) at a redshift $z \approx 100$ following the methodology outlined in Oñorbe et al. (2014). This approach identifies a region spanning several virial radii around a main halo to resolve and produces a volume of uncontaminated halos around the main halo, which we use to study lower mass systems.

The first set of volumes we study come from the DMO versions of the following main halos from Fitts et al. (2017), which assume a WMAP year 7 cosmology: `m10f`, `m10g`, `m10h`, `m10i`, `m10j`, `m10k`, `m10l`, and `m10m`; these will be collectively referred to as the "`m10`" suite of simulations. These simulations have a dark matter particle mass of $m_{\rm dm} = 3000\ M_\odot$ with a physical force resolution of $\epsilon_{\rm dm} = 35$ pc. At this resolution, we are able to also explore dark matter halos surrounding the main halo down to masses of $10^7\ M_\odot$, which contains $\sim 10^4$ particles within the virial radius. In addition, we use several of the DMO volumes surrounding main halos mass of $\sim 10^{11}\ M_\odot$, which were first presented in Lazar et al. (2020): `m11d`, `m11e`, `m11h`, and `m11i`; these will be collectively referred to as the "`m11`" suite of simulations. The `m11` simulations have a mass resolution ~ 14 times worse than the `m10` suite. We use the `m11` volumes to explore halo masses down to $10^8\ M_\odot$, corresponding to $\sim 10^4$ particles within the virial radius. These simulations use a Planck 2015 cosmology (Planck Collaboration et al. 2016b).

Dark matter halos in all the simulations considered here are identified using the Amiga halo finder (AHF; Knollmann and Knebe 2009). The halo finder uses a recursively refined grid that determines the local overdensities found within the density field and identifies the density peaks of this field as the center of these halos. The AHF algorithm is known to be fully recursive in identifying host halos and there substructure (Gill et al. 2004, Onions et al. 2012).

3.2.2 Chapter nomenclature

Halo mass and radius

Isolated dark matter halos that inhabit the LOS population are defined as a spherical overdensity of mass, M_Δ, contained within a radius, r_Δ, that encloses some density contrast, Δ, relative to a reference background density at a particular redshift, $\rho_{\rm ref}(z)$. Throughout this paper, we primarily define the dark matter halos by their virial mass, $M_{\rm vir}$, which are spherical systems with virial radius, $r_{\rm vir}$, inside of which the average density is equal to the critical density is a multiplicative factor of the virial overdensity, $\Delta_{\rm vir}(z)$ via (Bryan and Norman 1998), i.e., Equation 1.4. The Bryan and Norman (1998) definition is the primary spherical overdensity definition used for the AHF halo finding, but is computed based off of the gravitationally bound particles of the system. For the purposes of this analysis, we recompute $M_{\rm vir}$ and $r_{\rm vir}$ using *all* dark matter particles (bound and unbound) of the spherical overdensity peak identified by AHF. It should be noted that isolated dark matter halos are also commonly defined with overdensity $\Delta = 200$ with either a critical or mean-matter background densities. We do not explore such definitions other than $M_{\rm vir}$ in this analysis, but save such parametrization for the next chapter.

Three-dimensional structure of dark matter halos

The three-dimensional density profiles of dark matter halos in ΛCDM are commonly modeled with the Navarro et al. (1997) (NFW) profile ($\rho_{\rm NFW}$; Equation 1.12), where r_s is the scale radius and ρ_s is the scale density at r_s. The structure of a NFW halo is parameterized by the concentration ($c_{\rm NFW}$; Equation 1.13) of a dark matter halo, which is formally defined as the ratio between the size of the halo, $r_{\rm vir}$, and the scale radius, r_s. In DMO simulations, dark matter halos are better described by the Einasto profile (ρ_ϵ; Equation 1.14), which provides a good description over 20 decades of halo masses (Wang et al. 2020). Here, r_{-2} is the scale radius where the log-slope is

equal to −2, the scale density is $\rho_{-2} := \rho(r_{-2})$, and α_ϵ is the shape parameter. Usually α_ϵ is fixed to make this a two-parameter function, but it can be expressed in terms of peak height (e.g. Gao et al. 2008, Prada et al. 2012, Klypin et al. 2016, Child et al. 2018). The shape parameter is fixed to $\alpha_\epsilon = 0.17$ for this analysis, which fits well for the range of halo masses we explore here and is close to commonly-adopted values (e.g. Wang et al. 2020). The internal structure from the Einasto profile is parameterized by the dimensionless concentration parameter ($c_{\rm vir}$; Equation 1.15). Note that r_s in the NFW profile is also the radius where the log slope of the NFW form is −2, so typically $c_{\rm vir} \simeq c_{\rm NFW}$ for any individual halo.

Two-dimensional structure of dark matter halos

For a given system that has a (intrinsic) spherically-averaged local density profile in three-dimensions, $\rho(r)$, the *cylindricaly-averaged, local surface density* profile, $\Sigma_\rho(R)$, is quantified by integrating the along the line of sight, ℓ, for a path of some depth $\mathcal{L}$

$$\Sigma_\rho(R) = \int_{-\mathcal{L}/2}^{\mathcal{L}/2} d\ell\, \rho(R,\ell) \tag{3.1}$$

$$= 2\int_{R}^{\mathcal{L}/2} dr\, \frac{r\rho(r)}{\sqrt{r^2 - R^2}}\,, \tag{3.2}$$

where R denotes the projected radius relative to the center of the halo and $\ell = \sqrt{r^2 - R^2}$ is a coordinate along the line of sight to the observe. In lensing studies, it is common to use an NFW profile in the limit where $\mathcal{L} = \infty$ via a forward Abel transformation, which recovers Equation 1.18. In what follows we explore choices for the path length of integration in constructing numerical surface density profiles of the form $\mathcal{L} = 2\,\xi\, r_{\rm vir}$. As described below, we settle on $\xi = 1.5$ as an optimal choice.

Non-spherical dark matter halos

Another important aspect of dark matter halos is their non-spherical shape. ΛCDM halos are triaxial and tend to be more elongated higher halo masses. Dark matter halos viewed along their major axis (i.e., the densest axis) could be misidentified as a higher mass halo or a halo of higher concentration. To explore the magnitude of this effect, we calculate dark matter halo shapes for our halos by computing the shape inertia tensor outlined in Allgood et al. (2006). This is done by solving the eigenvalues from all of the dark matter particles within a shell between 10 - 20% of $r_{\rm vir}$. The resulting eigenvalues of the shape tensor are proportional to the square root of the principal axes of the dark matter distribution, which we will refer to as the "major", "intermediate", and "minor" axes throughout this paper.

Note that the triaxial shape of DMO halos can be taken into account in lensing studies by projecting a triaxial NFW profile directly (e.g., Feroz and Hobson 2012). Doing so requires six parameters rather than two for each halo. In what follows, we present a direct fit to the projected, cylindricaly-averaged, profiles that provide improved accuracy over the projected NFW with the same number of free parameters.

3.2.3 Radial profiling

Region of numerical convergence

One of the key components of our analysis focuses on the spherically (and circularly) averaged mass profiles. Before radial bins are constructed, dark matter particles are first shifted relative to the halo center determined by AHF. The innermost regions of N-body simulated dark matter halos, to some extent, are impacted by numerical relaxation. The region of convergence, $r_{\rm conv}$, is quantified using the method specified in Power et al. (2003), where the effective resolution of the simulations dictates the location of the radius where the two-body relaxation timescale, $t_{\rm relax}$, becomes shorter

than the age of the universe, t_0, set by the criterion:

$$\frac{t_{\rm relax}(r)}{t_0} = \frac{\sqrt{200}}{8}\frac{N(<r)}{\ln N(<r)}\left[\frac{\bar{\rho}(<r)}{\rho_{\rm c}(z)}\right]^{-1/2} . \tag{3.3}$$

Here, $N(<r)$ is the cumulative number of particles within radius r and the cumulative density profile, $\bar{\rho}(<r) = 3M(<r)/4\pi r^3$, with $M(<r)$ being the cumulative mass. For N-body simulations of our resolution, convergence is shown to be well resolved to the radius at which the criterion satisfies $t_{\rm relax} > 0.6\,t_0$ with <1% resolution level deviations for isolated zoom runs (see Hopkins et al. 2018). The typical convergence radii within our sample at redshift $z = 0.2$ are resolved to regions relevant for lensing based analysis; in what follows, we present results grouped in five mass bins, set by five decades in halo virial mass: $M_{\rm vir} \simeq 10^{7-11}\,M_\odot$. The halo masses with bins of $M_{\rm vir} = \{10^7,\,10^8,\,10^9,\,10^{10},\,10^{11}\}\,M_\odot$ have convergence radii of $r_{\rm conv} \simeq \{300,\,270,\,240,\,200,\,500\}$ pc, in order from lowest to highest mass decade.

Constructing spherical density profiles

The local density profile, $\rho(r)$, is defined as the *total* (bound and unbound) dark matter mass found in each bin divided by the spherical shell. From halo-to-halo, we fit the NFW and Einasto profiles to their local density profiles, which is constructed using 35 logarithmic spaced radial bins from $r_{\rm conv}$ to $r_{\rm vir}$ for all of the dark matter particles within $r_{\rm vir}$. The best-fit parameters are determined by the following minimization of the figure-of-merit in a least-squares optimization:[1]

$$Q^2_\rho = \frac{1}{N_{\rm bins}}\sum_i^{N_{\rm bins}}\left[\log\left(r_i^2\rho_i\right) - \log\left(r_i^2\rho_i^{\rm model}\right)\right]^2 . \tag{3.4}$$

Instead of ρ being minimized, which has the numerical value decrease by many orders of magnitude between the inner and outer region of the profile, the $r^2\rho$ merit provides a more balanced indicator of goodness-of-fit across the entire radial range. From each individual fit, we record best-fit

[1]The convention used here in this chapter is $\log \equiv \log_e \equiv \ln$.

parameters for the NFW density profile and Einasto profile with fixed $\alpha_\epsilon = 0.17$.

Constructing cylindrical surface-density profiles

Halo surface density profiles are constructed in a similar manner to the three-dimensional profile: we measure the local surface density profile in two-dimensions, $\Sigma(R)$, by counting *all* (bound and unbound) dark matter particle mass that exists along a line-of-sight of total depth $\mathcal{L}$ in a thin circular ring of average radius R divided by the area of that ring. We use 35 logarithmic spaced bins of projected radius R that span an inner radius $R = r_{\rm conv}$ to an outer cylindrical radius $R = r_{\rm vir}$.

In order to define the surface density of a three-dimensional object, we must define a depth of interest, $\mathcal{L}$ (see Equation 3.1). In analytic investigations, it is common to chose $\mathcal{L} = \infty$, however this is neither possible numerically nor physically meaningful since we would like to characterize the degree of perturbation caused by the halo *over the background*. At minimum, one should span the full diameter of the halo and use $\mathcal{L} = 2\,r_{\rm vir}$. However, we expect that there is additional clustered matter outside $r_{\rm vir}$. We have explored this question using a depth parameter ξ defined via $\mathcal{L} = 2\,\xi\,r_{\rm vir}$. As discussed later in Section 3.5, we find that $\xi = 1.5$ provides stable results that appear to capture the relevant over-density adequately. We use $\xi = 1.5$ for the rest of this work.

In the following subsections we discuss fits to projected profiles. We do so by minimizing the figure-of-merit in a least squares optimization for surface density structures in a given projection:

$$Q^2_\Sigma = \frac{1}{N_{\rm bins}} \sum_i^{N_{\rm bins}} \left[\log\left(R_i \Sigma_i\right) - \log\left(R_i \Sigma_i^{\rm model}\right) \right]^2 . \tag{3.5}$$

As with the figure of merit used for the three-dimensional density profile, the $R\Sigma$ merit enables a more balanced weighing across the radial range being fitted. We exclude the outer radii ($R > 0.5 r_{\rm vir}$) when fitting since we aim to model the inner, higher-density regions that are most relevant for strong-gravitational lensing studies.

3.3 The projected structure of CDM halos

This section present the main results of this paper. We first start by contextualizing our work by comparing the accuracy of NFW and Einasto fits to the spherically-averaged density profiles for our sample of halos (Section 3.3.1). Sections 3.3.2 and 3.3.3 presents the circularly-averaged surface density profiles of the same dark matter halos and introduce an easy-to-use analytic profile that improves upon the projected NFW case, with an accuracy similar to that of an Einasto in three dimensions (Section 3.3.3). Finally, we introduce a convenient parameterization of a surface density structure along a specific orientation in Section 3.3.4.

3.3.1 Projected surface density profiles

The top panels of Figure 3.1 plot the local, spherically-averaged density profiles, $\rho(r)$, for several simulated halos (colored dash curves) grouped by decades of mass at $z = 0.2$. We chose this redshift since it is typical of lens systems. The density is additionally scaled by r^2 to constrain the dynamic range of the horizontal axis. The halos with masses ranging from $10^7 - 10^{10}\ M_\odot$ are collected from the `m10` suite of simulations while the `m11` simulations only presents their $10^{11}\ M_\odot$ main halos. Each profile is plotted from the virial radius, $r_{\rm vir}$, down to the innermost converged radius, $r_{\rm conv}$.[2] The thin solid lines show the best-fit NFW profiles (left plot) and Einasto profiles (right plot). The radii along the horizontal axis are all scaled by their best-fit scale radius, r_s for the NFW profile fits and r_{-2} for the Einasto profile fits. Residuals of the fits are shown in the bottom panels. We see that best-fit NFW profiles capture the normalization of the simulated profiles to within $\sim 40\%$, though the residuals do show a systematic U-shape. The best-fit Einasto profiles show no systematic difference with radius, and are accurate to within $\sim 20\%$ except at large radius. It is this level of improvement that has motivated the community to utilize the Einasto profile in favor of the NFW profile when precise predictions are required. We present this comparison here

[2]We adopt this convention for most of the figures in this paper, unless otherwise specified.

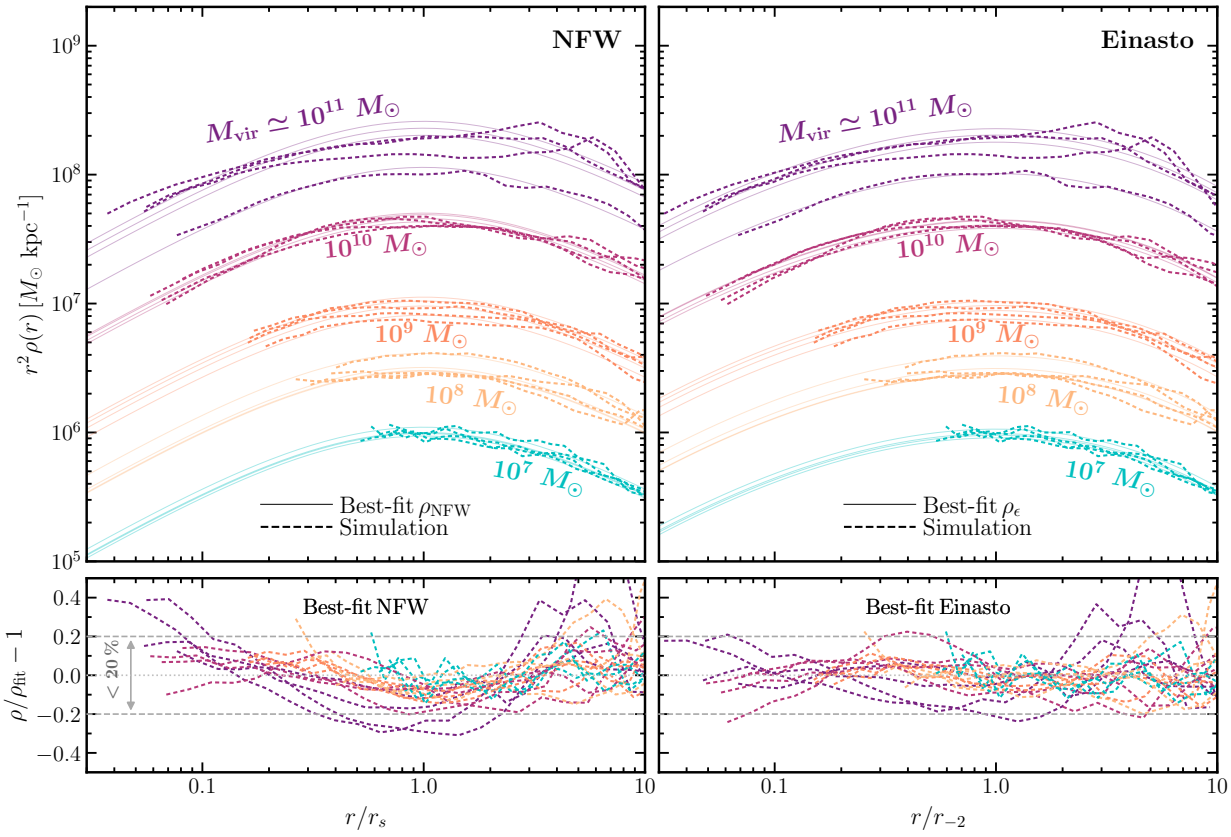

Figure 3.1: The spherically averaged density profiles, $\rho(r)$, of the simulated dark matter halos at $z = 0.2$. The top panels present several density profiles of the isolated dark matter halos (dashed curves) in mass groups spanning $M_{\rm vir} = 10^{7-11}\ M_\odot$. The density profiles are scaled by r^2 to set apart the dynamic range and the x-axis is scaled by r_s of the best-fit NFW profile (left panels) and r_{-2} of the best-fit Einasto profile (right panels). The simulated profiles are plotted from the convergence radius, $r_{\rm conv}$ out to $r_{\rm vir}$. The thin solid lines illustrates the best-fit halo density profile of each halo for the NFW profile (left panel) and the Einasto profile (right panel). The bottom panels depicts the quality of fit based on the *best-fit* parameters for each individual halo using the NFW and Einasto density profiles. The gray dashed lines encapsulates fits within 20% accuracy.

to provide context for the new surface-density fit we propose. We note that the projected version of the Einasto profile is analytically cumbersome, and this is why most lensing searches for low-mass perturbers assume projected NFW forms.

The left panels of Figure 3.2 presents the same simulated halos shown in Figure 3.1, but now as circularly-averaged surface-density profiles, $\Sigma(R)$, along with the projected version of the best-fit NFW profile for each halo (Equation 1.12, thin solid lines). For each halo, we show the surface density profile along the three main halo density axes (as described in Section 3.2.2): the major axis (thick-dashed curves), intermediate axis (thin-dashed curves), and the minor axis (dotted curves). On the vertical axis we plot the surface density profile multiplied by the projected radius, R, to limit the dynamic range. The horizontal axis shows the projected radius, R, divided by the best-fit NFW scale radius determine from the spherically average density fits (left plot), r_s. The fit residuals are shown along the bottom. We see that, especially at small radii, the fits are systematically biased (either low or high depending on the halo orientation).

3.3.2 Radial dependence on logarithmic slopes

As interesting observation from Figure 3.2 is that their is a hint, though, a non-trivial one, of a "universal" scale along the projected radius that the projected structure becomes more or less dense based on a specific orientation. Importantly, this seems to happen at a radial scale that is mass independent. It is instructive then to see how the logarithmic slope of the projected density, $\mathrm{d}\log\Sigma/\mathrm{d}\log R$, behaves a function of projected radius, R. We find that the behavior of the logarithmic slope for the surface-density profile is captured by a radially-dependent power law profile that is simple in form:

$$\frac{\mathrm{d}\log\Sigma_\beta}{\mathrm{d}\log R} = -\left(\frac{R}{R_{-1}}\right)^\beta . \tag{3.6}$$

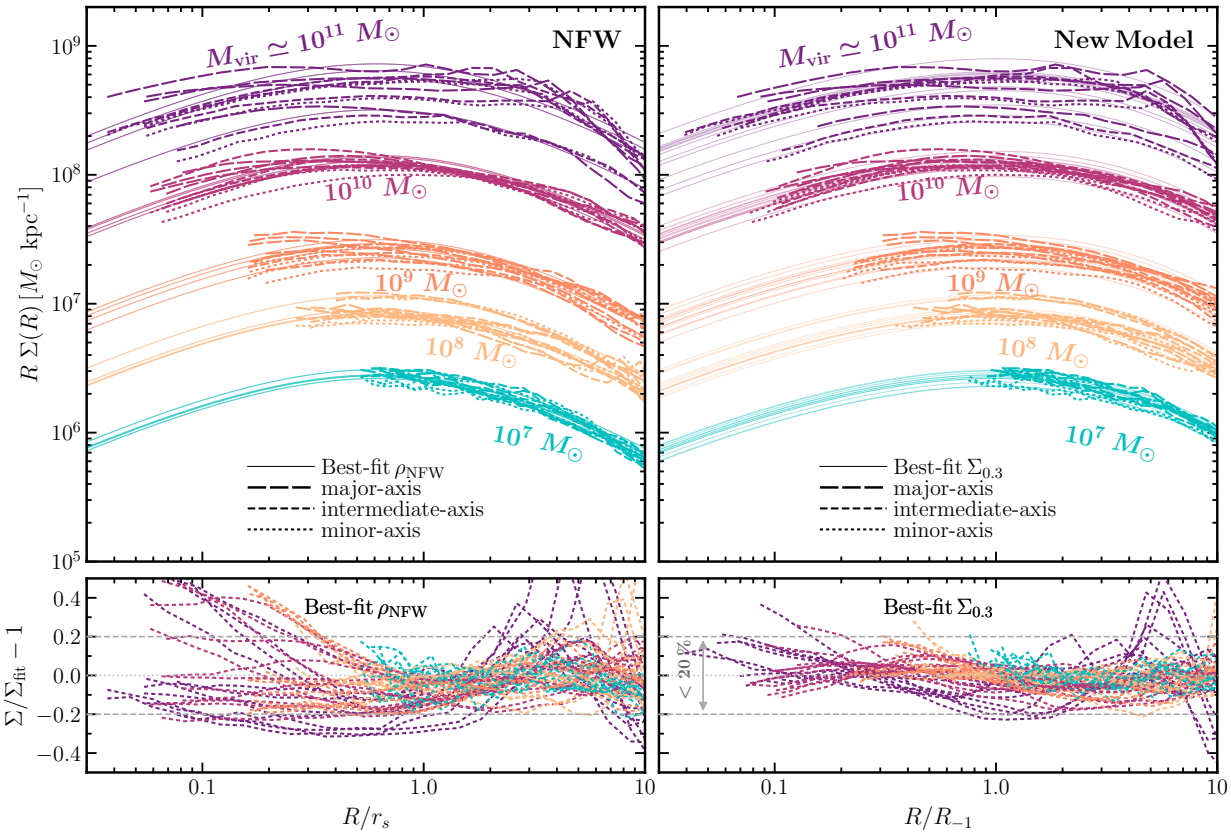

Figure 3.2: The resulting *mean surface density* profiles of the simulated dark matter halos at $z = 0.2$. Similar in presentation as the previous figure, the top panel presents the same isolated dark matter halos, but now for their projected density profiles, $\Sigma(R)$, along the major (thick-dashed curve), intermediate (thin-dashed curve), and minor axis (dotted curve). The bottom panels depict the fit quality made to each density axis. Here, we scale the $\Sigma(R)$ with R to emphasize the dynamic range and we also scale the projected radius (R) by the respective, best-fit scale radii, where the simulated profiles in R are plotted from the convergence radius, $r_{\rm conv}$ out to $r_{\rm vir}$. *Left:* The thin solid line shows the expected surface-density profile of each halo from the previous figure according to the NFW model, which are based on their *best-fit* parameters for each individual three-dimensional density profile. The radii is also scaled by the corresponding scale radius, r_s). *Right:* The same simulated curves presented in the left panel, but instead, the *best-fit* curves from fitting the $\Sigma_{0.3}$ profile (Equation 3.7 with $\beta = 0.3$) we introduced in the main text applied to each density projection. The projected radii for these panels are normalized by the radius at which the logarithmic slope is equal to -1, R_{-1}, which is acquired by the curve fitting procedure. The $\Sigma_{0.3}$ profile is able to model each orientation to ~ 20 % and better based off of the fit quality presented in the bottom panel; an improvement from the NFW model shown in the left panel.

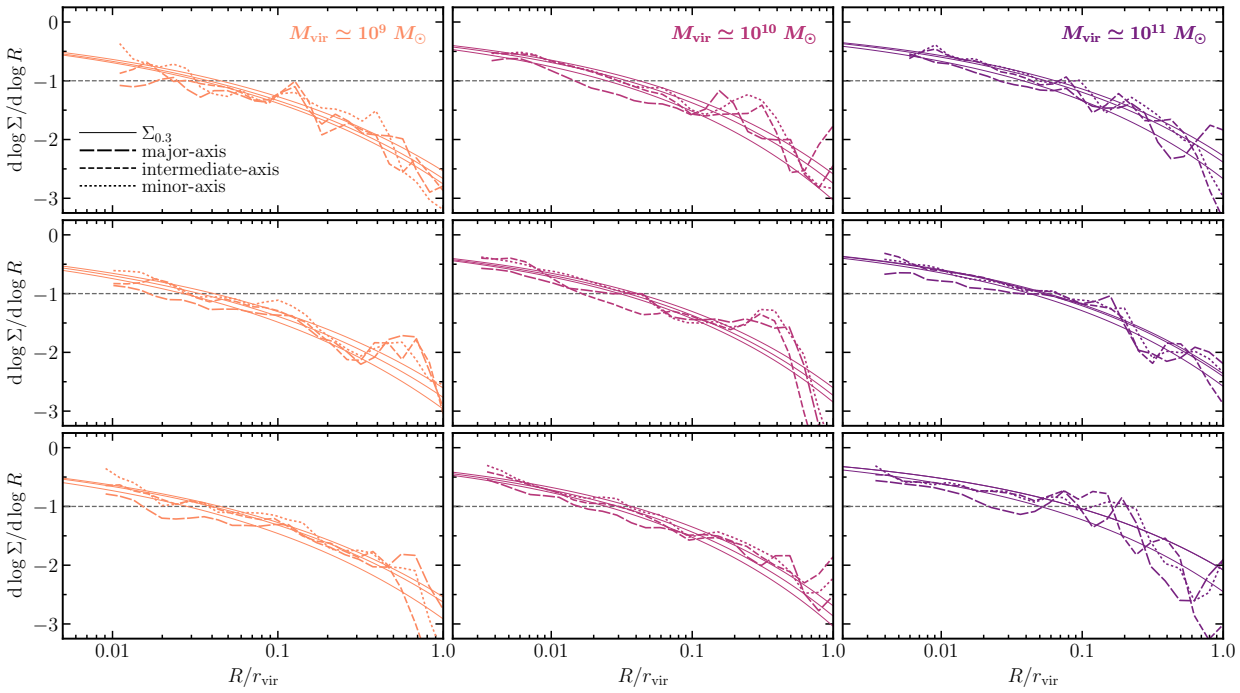

Figure 3.3: The logarithmic slope of the surface-mass density profiles, $\Sigma(R)$, along three density axis. Presented are several example halos for mass bins of $M_{\rm vir} \simeq 10^{11}$ (right-most panel), 10^{10} (center panel), and $10^9\ M_\odot$ (left-most panel) for demonstration purposes. The three density axes for a single halo are is plotted within a single panel. A power-law radial dependence of the slope seems to fit the different density axes of our simulations very well. Our predictive model, Σ_β, introduced in Equations 3.6 and 3.7, are shown as thin-solid lines for the best-fit parameters to Σ_β with fixed $\beta = 0.3$.

Here, R_{-1} is the radius where the logarithmic slope of the surface density is equal to -1 and β is the shape parameters of that effectively tailors itself to any dark matter halo. Note that by eliminating the dependence of the shape parameter, β, for a given halo, a given orientation is parametrized by the projected scale radius, R_{-1}, which in-turn captures the variation and scatter expected from halo-to-halo.

This is shown in Figure 3.3, where we selected three representative halos within three of the higher-mass bins: 10^9, 10^{10}, and $10^{11}\ M_\odot$ in the left-most, center, and right-most panel, respectively. The logarithmic slopes in each mass bin follows a similar shape out to $r_{\rm vir}$ along each density-axes projection, minus the sporadic-like behavior seen in the outer region. It is until the profiles approaches the inner-region where we begin to see differences between all three profiles. A clear

deviation, found for all of these masses, between each density axes is seen around the region at which the log-slope is equal to -1, which is marked by the dotted-gray horizontal line. Another important feature here is how each profile does not converge to some finite value. This would imply that the actual two-dimensional profile does not centrally converge to some power law.

The thinner solid lines in each panel of Figure 3.3 depicts Equation 3.6. The lines are determined from fitting the integrated profile of Σ_β to the local surface density profiles with a fixed shape $\beta = 0.3$. The power-law profile is shown to reproduce the radial dependence fairly well within the three different density axes. Not that by eliminating the dependence of the shape parameter, β, for a given halo, a given orientation is parametrized by the projected scale radius, R_{-1}, which in-turn captures the variation and scatter expected from halo-to-halo.

3.3.3 An improved surface density profile for dark matter halos

Our improved model is demonstrated in Figure 3.3 where it satisfies several requirements seen for our simulated halos: the analytical profile captures the different, radial-dependent structure towards the center, the scatter in the dynamical shape from halo-to-halo, and the lack of convergence to a central power-law. Equation 3.6 was shown to satisfy these requirements. Integrating out Equation 3.6 introduces a generalized form that captures the dynamical shapes of the surface density profile for a given projection:

$$\Sigma_\beta(R) = \Sigma_{-1} \exp\left\{ -\frac{1}{\beta}\left[\left(\frac{R}{R_{-1}}\right)^\beta - 1\right]\right\}, \tag{3.7}$$

where the normalization is defined by $\Sigma_{-1} := \Sigma(R_{-1})$. Notice that Equation 3.7 is the same analytical form as the Sersic (1968) and Einasto (1965) profile.

Note as a consequence of defining functional form of Equation 3.6, the logarithmic slope is null at the $R = 0$, which will then imply a constant surface-mass density at the center for the integrated

profile: $\Sigma(0) = \Sigma_{-1} \exp(1/\beta)$. The form of Σ_β has three free parameters: Σ_{-1}, R_{-1}, and β. Leaving all three parameters free allows Σ_β to be well fitted to any shape in projection. Based on the mass ranges for the ΛCDM halos explored here, we find that $\beta = 0.3$ is well fitted for our entire sample halos. As a result, we will refer to these fits as the $\Sigma_{0.3}$ model.

Usefully, for the mass ranges of ΛCDM halos explored here, we find that $\beta = 0.3$ allows us to characterize our entire sample of halos with two free parameters quite well, as shown below. With β fixed to 0.3, we have a two-parameter function, $\Sigma_{0.3}(R)$, that can be fully specified by Σ_{-1} and R_{-1}. As demonstrated in Section 3.3.4, we can also characterize the profile with a concentration parameter, in analogy with what is traditionally done with NFW profiles or Einasto profiles in three-dimensions.

The quality of the $\Sigma_{0.3}$ fits can be seen in the right-hand panels of Figure 3.2. Here we use the same simulated halos presented earlier in the left-most panel, but instead of using NFW fits for each halo, we now use the best-fit $\Sigma_{0.3}$ fit for the *individual* density-axis projections (the solid-thin lines). The projected radius along the horizontal axis is normalized by the best-fit projected scale radius, R_{-1}. The residuals of the $\Sigma_{0.3}$ fits are shown in the lower-right panel, where the inner-most region is captured to better than $\sim 20\%$ in all cases. This a clear improvement to the NFW model shown on the left, and similar in quality to the Einasto profile fits of halos within three dimensions shown in Figure 3.1. The improvement with respect to NFW is most significant at small radii $R \lesssim R_{-1}$, where the surface densities are the highest.

To further emphasize the improvement of the $\Sigma_{0.3}$ fits compared to NFW, we present quality-of-fit parameters in Figure 3.4. The top panel shows residuals for the eight $10^{10}\ M_\odot$ halos in our sample for the NFW model (dashed magenta curves) and our $\Sigma_{0.3}$ model (solid cyan curves). We use the projected profiles for each halo projected along its major, minor, intermediate density axes. We see that the NFW model can be off by as much as $\sim 50\%$ at small radius, and that the sign of the offset is systematic, depending on orientation. The new model captures the profiles to within 20% in all cases. At small radii, $R \lesssim 2$ kpc, which corresponds to $R \lesssim R_{-1}$ in this mass range, we again see

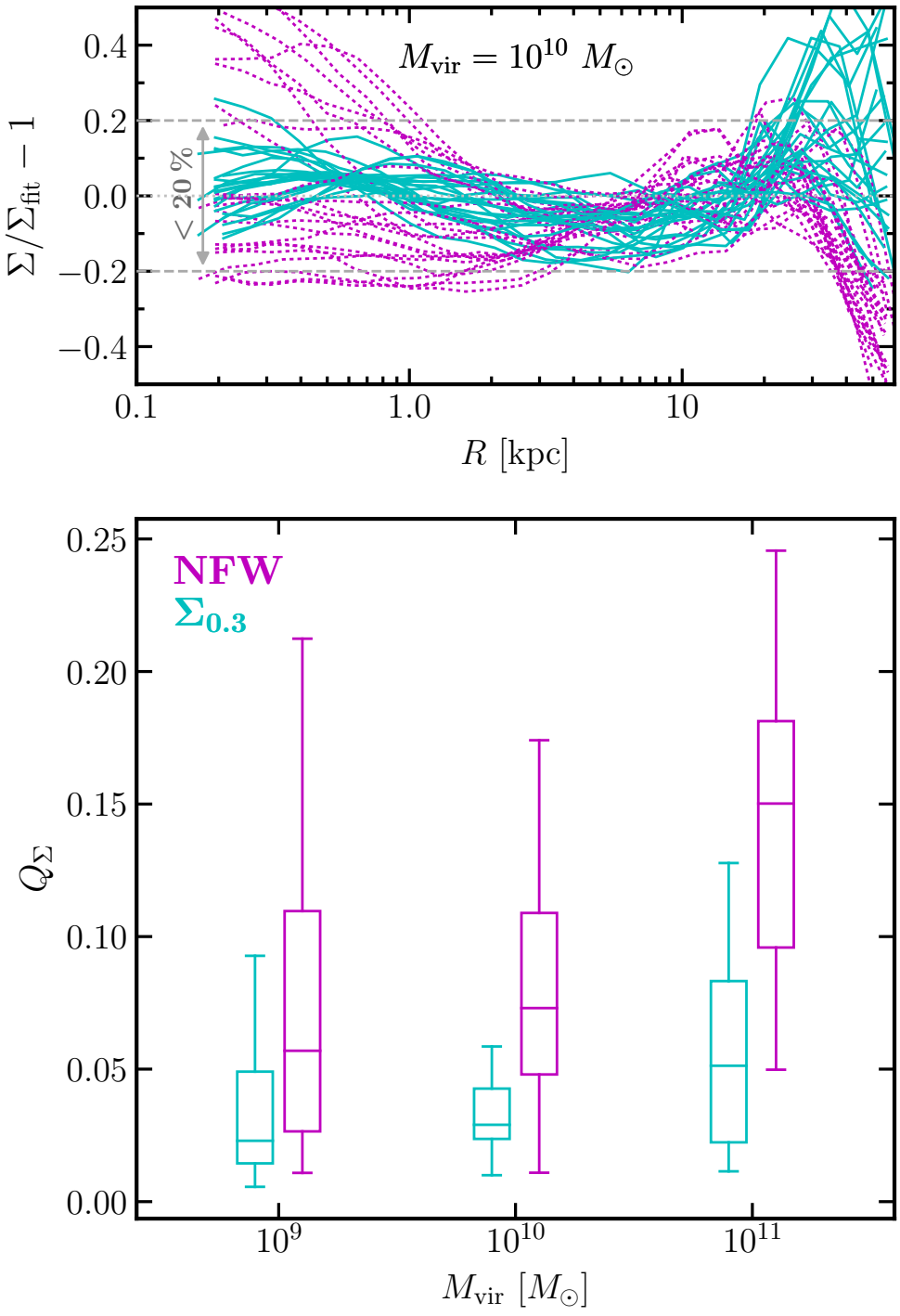

Figure 3.4: *Top*: The profile residuals for the four 10^{11} halos in our sample using the NFW model (dashed magenta curves) and our introduced $\Sigma_{0.3}$ model (solid cyan curves) for each of the density axis. Our new model significantly outperforms the NFW model for modelling cases of extreme elongation of high-mass halos in question. *Bottom*: The distribution of figure-of-merits (Equation 3.5) as quantified by the best-fit parameters of each model for four decades of halo mass.

that the $\Sigma_{0.3}$ profile is able to capture the true projected density structure more accurately than the inferred NFW shape.

Figure 3.5 shows the relationship between best-fit R_{-1} values and halo $M_{\rm vir}$ for our full sample. We have fit $\Sigma_{0.3}$ profiles to ten random projections of each halo. The thick magenta line and associated band show the median and 90 percentile range as a function of virial mass. The dotted cyan line shows a power-law fit, which has a best-fit slope $R_{-1} \propto M_{\rm vir}^{\gamma}$, where $\gamma = 0.35$, from only the sample up to $M_{\rm vir} = 10^{10}\ M_{\odot}$. The vertical pink band shows the region ($M_{\rm vir} < 10^{8}\ M_{\odot}$) where typical values of R_{-1} are smaller than the typical convergence radii for the simulated halos. Fits in this region rely on extrapolation to infer the value of R_{-1} and this likely gives rise to some non-physical dispersion in characteristic radius.

Another way to understand the utility of $\Sigma_{0.3}$ parameterization is compare its accuracy to the typical NFW approach at a fixed radius. Figure 3.6 shows the relative error (simulated vs. fit) of the two approaches at a projected radius $R = 600$ pc, which corresponds to ~ 0.2 arcsec at $z = 0.2$ as a function of halo virial mass. In this exercise, we have viewed each simulated halo along 10 random orientations and used $\Sigma_{0.3}$ fits associated with each orientation compared with the implied spherical NFW fit in each case. Relative errors for the best-fit $\rho_{\rm NFW}$ and $\Sigma_{0.3}$ fits are shown in magenta and cyan, respectively. The solid curve shows the median as a function of $M_{\rm vir}$, while the bands encapsulates the 2σ range. We see that the relative error in NFW fits is larger at larger masses. This reflects the fact that the $\Sigma_{0.3}$ fits show the most improvement for $R < R_{-1}$. At higher masses, 600 pc is “deeper" within the core, so that the relative error coming from the NFW assumption increases.

3.3.4 Parameterizing the orientation of projection

The spherically-averaged, three-dimensional density profile of a dark matter halo is often quantified by an NFW profile using two parameters: a halo mass and a concentration parameter (e.g. Bullock

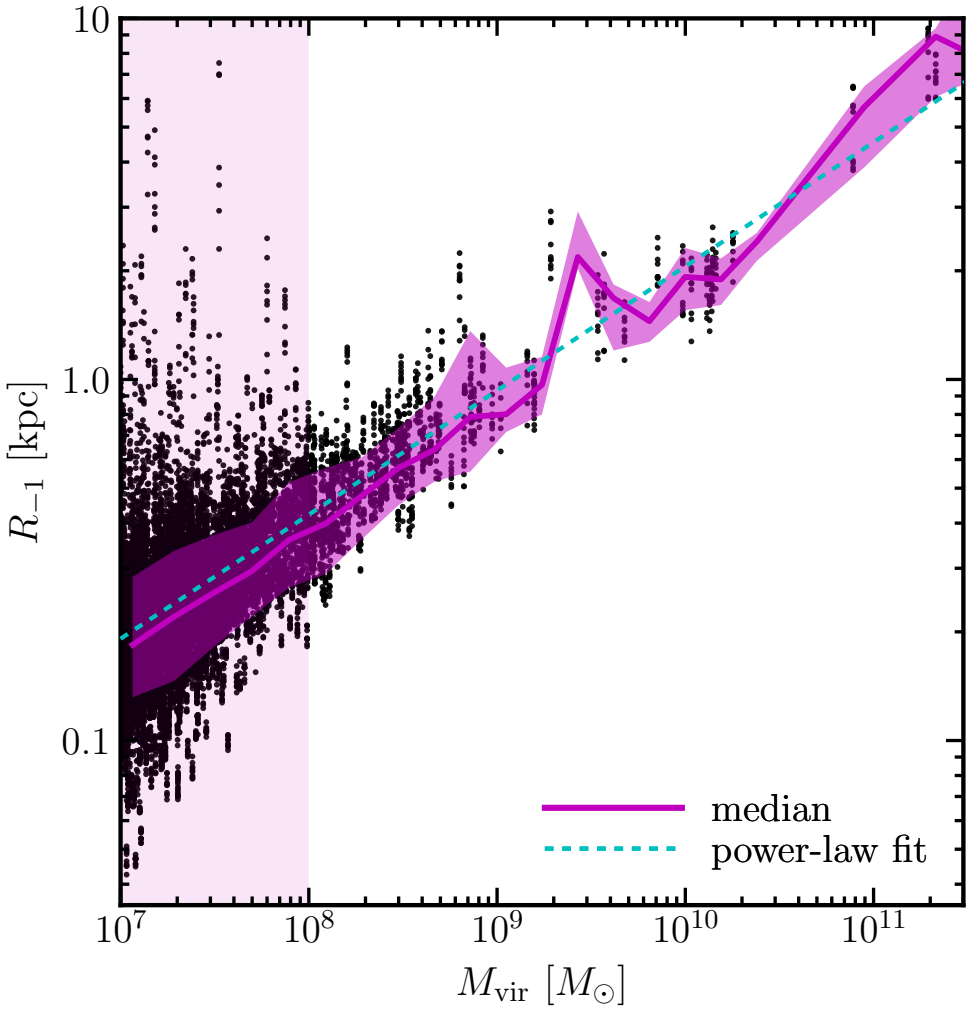

Figure 3.5: Best-fit values of the R_{-1} scale radius versus halo virial mass for $\Sigma_{0.3}$ fits to 10 random projections to each halo in our sample. The solid line and shaded bands reflect the median and ninety percentile bands of the distribution. The vertical pink band shows the region where fits are likely not reliable because the typical value of R_{-1} is smaller than the typical convergence radius for halos. Dotted power-law fit shows the relation $R_{-1} \propto M_{\rm vir}^{0.35}$. Note that these simulations are not a representative cosmological sample, so this masss-radius relation may not be representative for the halo population in general.

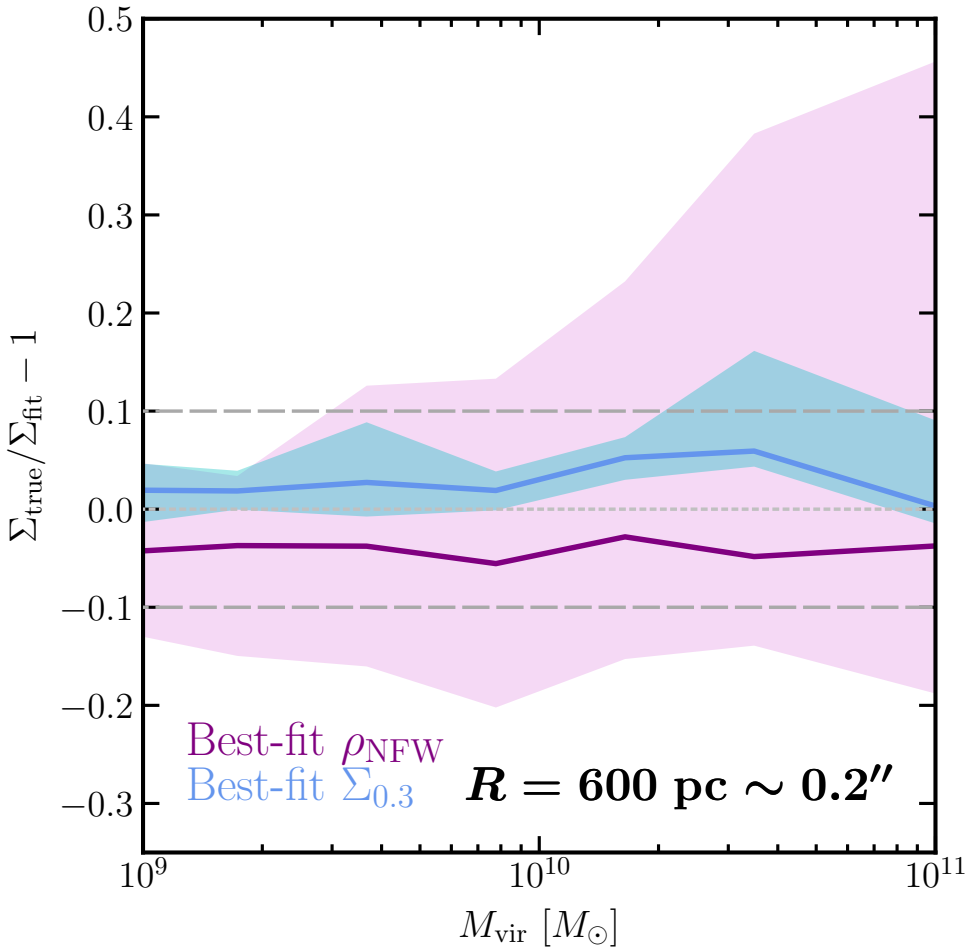

Figure 3.6: The quality of fit for inner-most projected density (at 600 pc) between the simulation results, $\Sigma_{\rm true}$, and the profile fits, $\Sigma_{\rm fit}$, for the $\rho_{\rm NFW}$ and $\Sigma_{0.3}$ profiles (purple and blue curves, respectively), as a function of $M_{\rm vir}$. The bands encapsulate the 2σ scatter for ten random projections on each resolved isolated halo. The relative error in NFW fits is larger at larger masses because 600 pc is "deeper" within the core (smaller compared to R_{-1}) at higher masses (see Figure 3.5). The $\Sigma_{0.3}$ fits provide the most improvement for radii smaller than the scale radius $R < R_{-1}$.

et al. 2001). Similarly, we can quantify the circularly-averaged, projected density profile of a dark matter halo along any orientation with a *projected concentration*, defined as

$$C_{\rm vir} := r_{\rm vir}/R_{-1}\,. \tag{3.8}$$

Figure 3.7 provides some physical insight on the meaning of these parameters. We plot the projected mass within 1 kpc, $\mathcal{M}(< R = 1\,{\rm kpc})$, as a function of halo mass. For reference, 1 kpc has an angular size of ~ 0.3 arcsec at $z = 0.2$. Each halo in our sample is viewed along 10 random orientations, which can be seen as vertical stacking at fixed virial mass at high masses. The color bar maps to the best-fit projected concentration $C_{\rm vir}$ for each halo/orientation. Lower-density projections for the same halo have lower projected concentrations, and this provides a way to quantify the scatter associated with halo shape. As one might expect, there is a correlation between $\mathcal{M}(1\,{\rm kpc})$ and $M_{\rm vir}$. For virial masses below $10^{10} M_\odot$, where $R_{-1} \lesssim 1$ kpc, the median relation scales as $\mathcal{M}(< 1{\rm kpc}) \sim M_{\rm vir}^{1/2}$. At higher masses, $R_{-1} \gtrsim 1$kpc, and the relationship becomes even flatter $\mathcal{M}(< 1{\rm kpc}) \sim M_{\rm vir}^{1/3}$. The weak power-law dependence makes inferring the halo mass from a projected mas somewhat challenging; a 20% error in surface density would map to a $\sim 40-60\%$ error in interpreted virial mass on average. The factor of ~ 2 scatter in projected mass at fixed virial mass is roughly captured by the scatter in projected concentration. Note that this level of variation at fixed virial mass is considerable; in the median, a factor of 2 increase in projected mass at 1 kpc is equivalent to a factor of ~ 4 (8) increase in $M_{\rm vir}$ at low (high) virial mass.

The light gray points in Figure 3.8 show the relationship between the projected concentration, $C_{\rm vir}$, and the standard three-dimensional halo concentration, $c_{\rm vir}$, for individual halos. Each halo has a fixed $c_{\rm vir}$, but has 10 values of $C_{\rm vir}$ derived from $\Sigma_{0.3}$ fits from 10 random orientations. We only include halos more massive than $M_{\rm vir} = 10^9\,M_\odot$ in this analysis in order to ensure accurate fits. The thick, solid black line shows a power-law fit to all the points, which provides a good representation of the average relation: $C_{\rm vir} \propto c_{\rm vir}^{\delta}$. The best-fit function is found to be $C_{\rm vir} = 2.3\,c_{\rm vir}^{0.87}$. The dashed

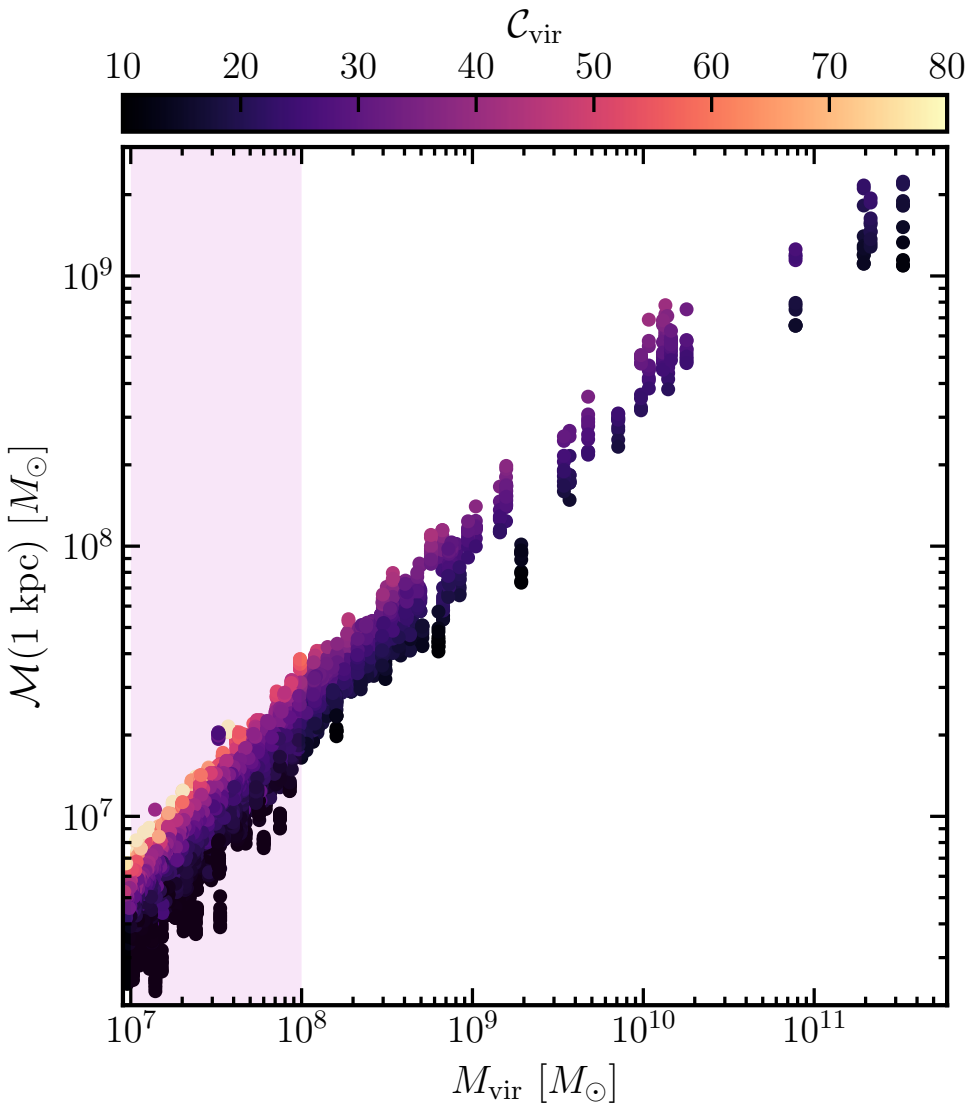

Figure 3.7: The projected mass within 1 kpc, $\mathcal{M}(< R = 1\ {\rm kpc})$, as a function of virial mass, $M_{\rm vir}$, for our sample of halos, each viewed along 10 random orientations. The points are color coded by the projected concentrations associated with $\Sigma_{0.3}$ fits along each orientation. We see that the projected concentration correlates with the density of the halo along a given projection at fixed $M_{\rm vir}$, and that this accounts for as much as a factor of ~ 2 variation in the relationship between virial mass and projected mass at this radius.

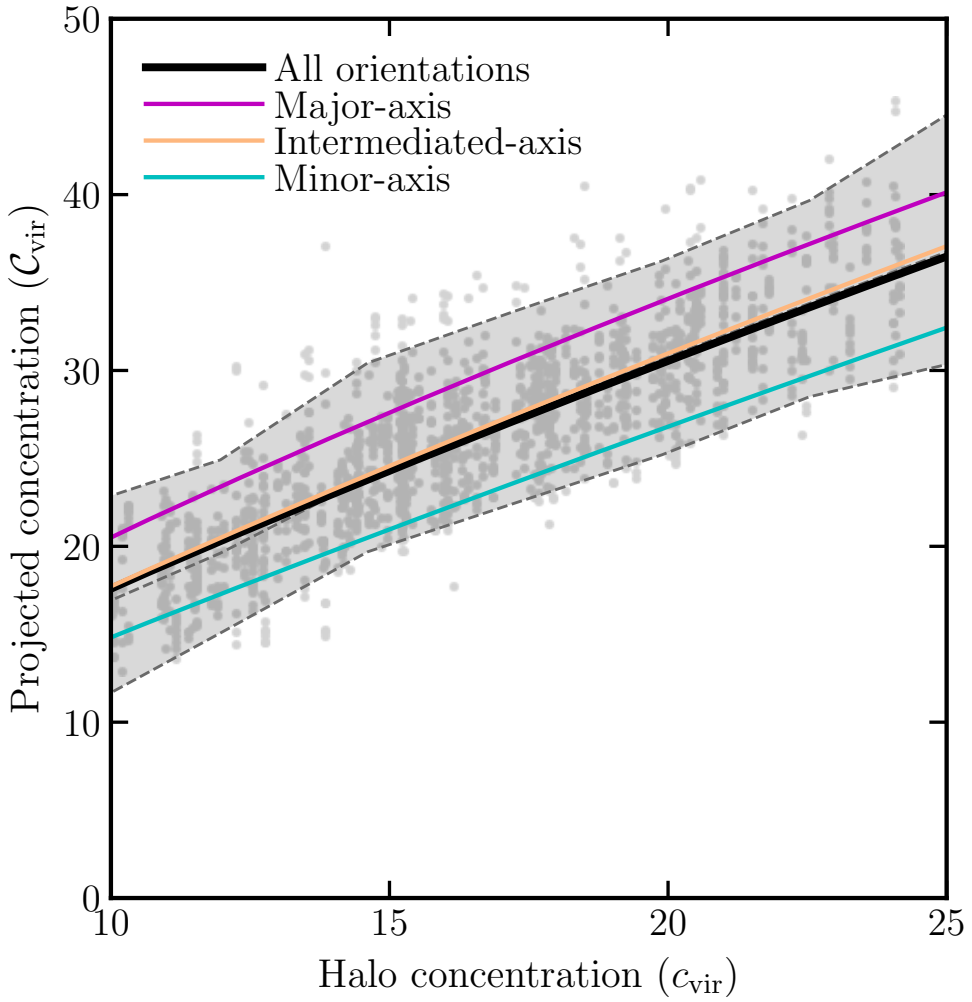

Figure 3.8: Relationship between the best-fit projected concentration using $\Sigma_{0.3}$ profiles, $C_{\rm vir}$, and the standard three-dimensional halo concentration, $c_{\rm vir}$, determined for the same halos' best-fit Einasto profiles. The gray points correspond to 10 projected random orientations of all halos in our sample. The thick, solid black is a power-law fit to all of light-gray points while the dashed lines reflect the $2-\sigma$ scatter at fixed $c_{\rm vir}$. The colored solid lines are power-law fits to the projected fits along the major, intermediate, and minor axis of each halo.

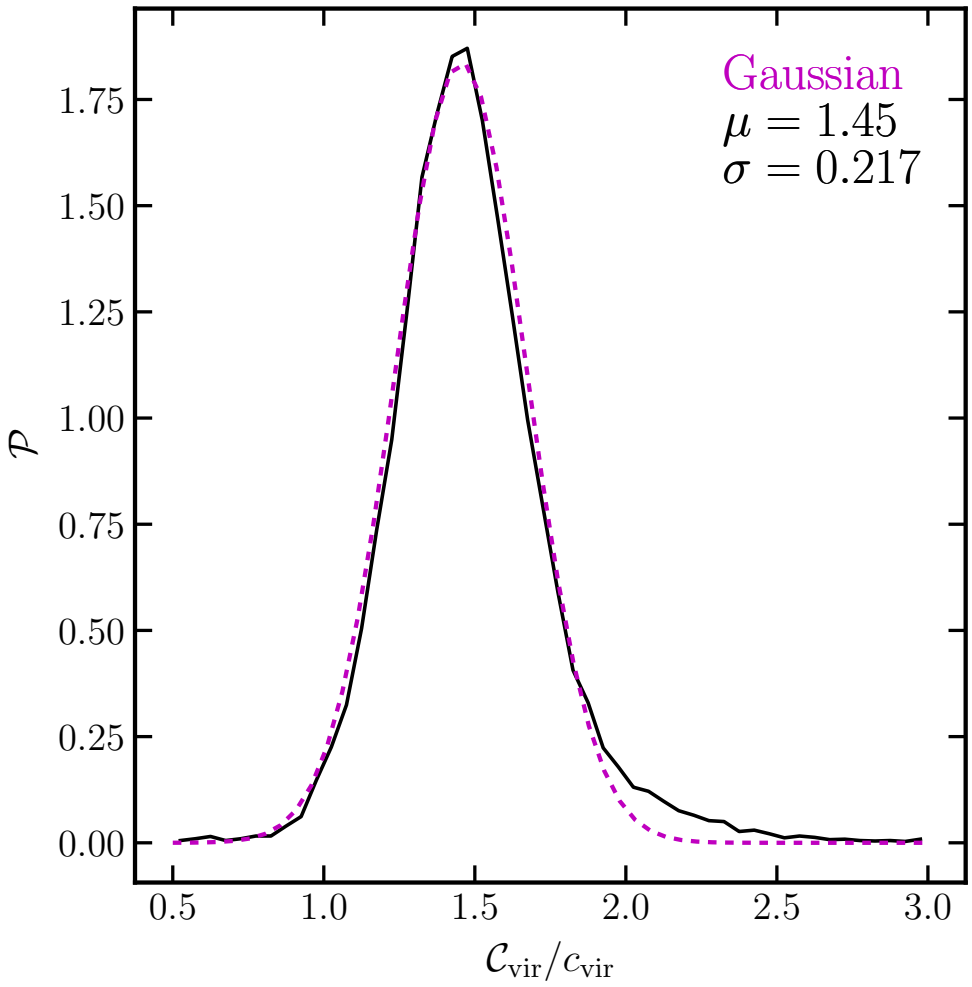

Figure 3.9: The probability distribution of the ratio between the projected concentration and the halo concentration $\mathcal{C}_{\rm vir}/c_{\rm vir}$ (black line), along with the best fit Gaussian fit (dashed magenta line).

lines show the 2σ distribution at fixed three-dimensional halo concentration, $c_{\rm vir}$. For reference, we also plot power-law fits for the same relation using only their major-, intermediate-, and minor-axis projections as pink, orange, and cyan lines, respectively. The intermediate-axis is roughly consistent with the average over all orientations, while the averages of the two other orientations track the $\sim 1.5\sigma$ range, suggesting that much of the variation at fixed $c_{\rm vir}$ comes from orientation effects.

Figure 3.9 plots the probability distribution (black curve) of $\mathcal{C}_{\rm vir}/c_{\rm vir}$ of all halos. The curve is nicely described by a Gaussian (dashed magenta) with mean $\mu = 1.45$ and standard deviation

$\sigma = 0.22$. From this, we can infer that the parameters have a mean relation of $C_{\rm vir} \simeq 1.5\, c_{\rm vir}$ at this fixed redshift; a larger sample of halos, sampled in cosmological volumes, and studied at a wider range of redshifts, will be needed to explore these relationships more completely.

3.4 Lensing profile properties

3.4.1 Projected mass distribution

The projected cumulative mass of the dark matter, $\mathcal{M}$, at the projected radius, R, found along a given orientation is structured as a face-on cylinder, where the variable cylinder radius is simply R with a hyper-parameter depth, $L_{\rm depth}$. In analytical form, this is

$$\mathcal{M}(R) = \int_0^{2\pi} \mathrm{d}\phi \int_0^R \mathrm{d}R'\, R'\, \Sigma_\beta(R') \tag{3.9}$$

$$= 2\pi \int_0^R \mathrm{d}R'\, R'\, \Sigma_\beta(R')\,, \tag{3.10}$$

where the last line assumes spherical symmetry. The projected mass profile for the enclosed mass is

$$\mathcal{M}\,(R) = \frac{2\pi\Sigma_{-1}R_{-1}^2}{\beta} \exp\left(\frac{1+2\ln\beta}{\beta}\right) \gamma\left[\frac{2}{\beta},\, \frac{1}{\beta}\left(\frac{R}{R_{-1}}\right)^\beta\right]\,, \tag{3.11}$$

where $\gamma(a, x)$ is the lower incomplete gamma function.

3.4.2 Projected mass normalization

To determine the normalization relation of the new lens mass model (Equation 3.7), assuming circular symmetry, we integrate R out to the virial radius r_Δ along a given orientation:

$$\mathcal{M}_{\rm eff} = 2\pi \int_0^{r_\Delta} {\rm d}R'\, R'\, \Sigma_\beta(R') \tag{3.12}$$

$$\mathcal{M}_{\rm eff} = 2\pi\, \Sigma_{-1} \int_0^{r_\Delta} {\rm d}R'\, R'\, \exp\left\{-\frac{1}{\beta}\left[\left(\frac{R'}{R_{-1}}\right)^\beta - 1\right]\right\}\,. \tag{3.13}$$

Note that we have defined $\mathcal{M}(r_\Delta) \equiv \mathcal{M}_{\rm eff}$, since integrating out to the virial radius does not always ensure we recover the virial mass of the halo, i.e., $\mathcal{M}(r_\Delta) \neq M_{\rm vir}$, as the depth of the projection is set by a cylinder depth defined in the main text, $L_{\rm depth} = \xi\, r_\Delta$, where ξ is some predetermined factor. Moving forward, we can make the substitution $x = R/R_{-1}$, which leads us to the relation:

$$\mathcal{M}_{\rm eff} = 2\pi\Sigma_{-1} r_\Delta^2\, \mathcal{I}\,(C_\Delta|\beta)\,, \tag{3.14}$$

where

$$\mathcal{I}\,(C_\Delta|\beta) = \frac{1}{C_\Delta^2}\int_0^{C_\Delta} {\rm d}x\, x \exp\left\{-\frac{1}{\beta}\left[x^\beta - 1\right]\right\}\,, \tag{3.15}$$

and the projected concentration is C_Δ.

The integral $\mathcal{I}$ cannot be solved analytically, but can be numerically integrated for a given value of C_Δ and β. We provide a generalized fitting fitting function:

$$\mathcal{I} = c_0 \exp\left[-n\left(\frac{C_\Delta + c_1}{c_2}\right)^{\frac{1}{n}}\right]\,. \tag{3.16}$$

Once fitted with $\beta = 0.3$, the best-fit parameters $c_0 = 5756$, $c_1 = 0.628$, $c_2 = 0.438$, $n = 7.41$. The results are presented in Figure 3.10, where the black line is the above integral with a fixed $\beta = 0.3$ as a function of the projected concentration, while the red-dashed line is the resulting

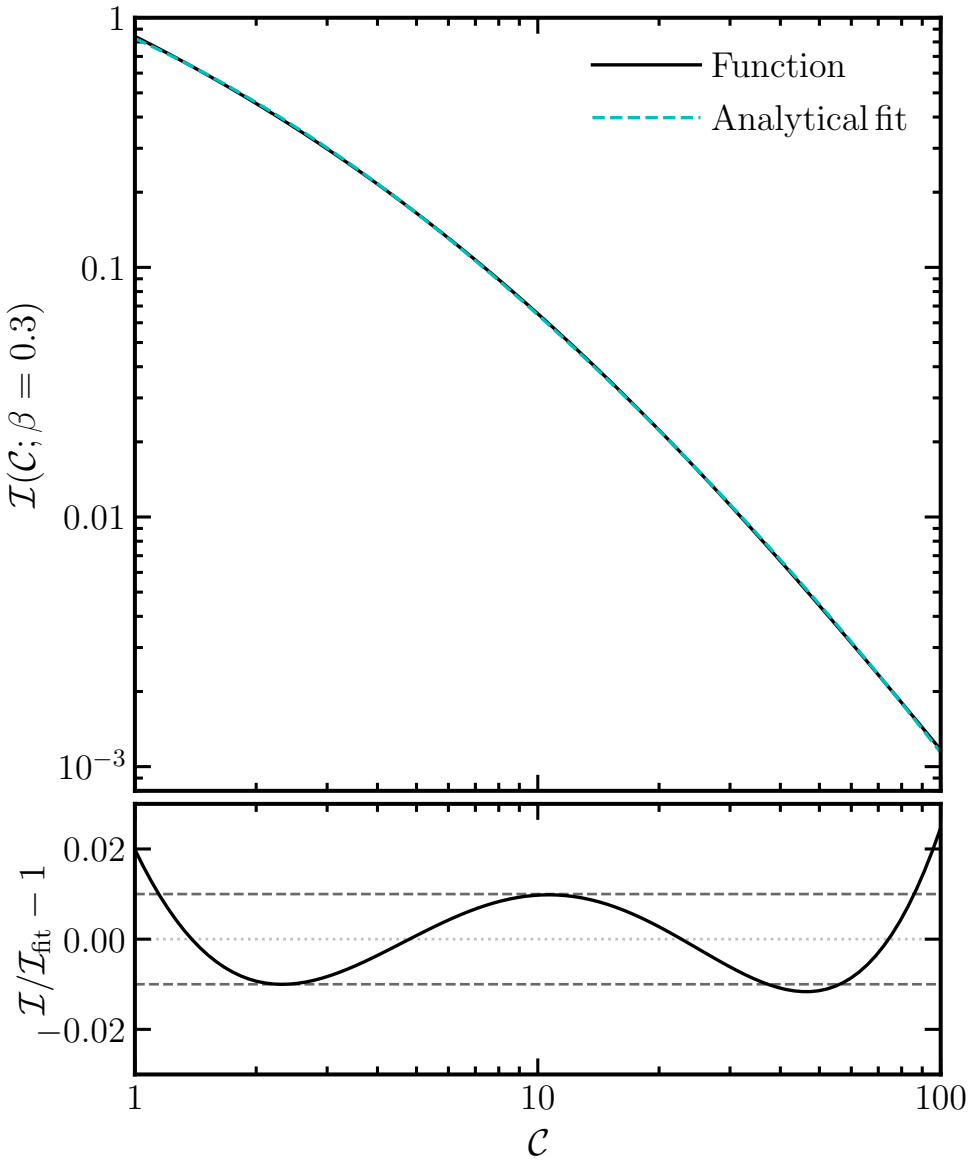

Figure 3.10: Fit to the integral function for $\beta = 0.3$ as a function of the projected concentration. The top panel plots Equation 3.15 as the black line while the dashed cyan curve is the resulting fit using Equation 3.16. The bottom panel plots the fit quality. The fit is accurate to 2% and better for a large range of projected concentrations.

fit. The bottom panel plots the residuals between the integral and the analytical fit. The best fit parameters is accurate to $\sim 2\%$ and better for ranges of $C_\Delta \in [1, 100]$. While not shown here, Equation 3.16 also fits accurately for shapes with $\beta \in [0.01, 0.40]$, which can be applicable for halos with differing shapes. With the above results, we arrive with the final form of the profile normalization as a function of mass and projected concentration:

$$\Sigma_{-1} = \frac{\mathcal{M}_{\rm eff}}{2\pi\, r_\Delta^2\, \mathcal{I}\,(C_\Delta; \beta)}\,. \tag{3.17}$$

Note that this normalization can be connected to the virial definition of the halo by imposing an established $\mathcal{M}_{\rm eff}$–$M_{\rm vir}$ relation (see next section for analysis).

3.4.3 Unit-convergence radius

The surface mass-density of a dark matter halo with a spherical Σ_β profile (Equation 3.7) expressed in units of the critical surface density yields the dimensionless convergence profile:

$$\kappa_\beta(R) = \Sigma_\beta(R)/\Sigma_{\rm c} = \kappa_{-1} \exp\left\{-\frac{1}{\beta}\left[\left(\frac{R}{R_{-1}}\right)^\beta - 1\right]\right\} \tag{3.18}$$

with $\kappa_{-1} := \Sigma_{-1}/\Sigma_{\rm c}$ such that $\Sigma_{-1} := \Sigma(R_{-1})$ and $\Sigma_{\rm c}$ is the critical surface density for lensing,

$$\Sigma_{\rm c} := \frac{c^2 D_s}{4\pi D_\ell D_{\ell s}}\,, \tag{3.19}$$

such that D_s, D_ℓ and $D_{\ell s}$ are the angular diameter distances between the observer from the source, the observer from the lens, and the lens from the source. The unit-convergence radius, R_κ, at which the convergence $\kappa_\beta(R_\kappa) = 1$, is simply

$$R_\kappa = R_{-1}\left[\beta \log\left(\kappa_{-1}\right) + 1\right]^{1/\beta}\,. \tag{3.20}$$

3.4.4 Deflection potential

A crucial component of modern lensing software is to analytically implement the lensing potential (and deflection angle) for structure in projection. Our projected mass profile is conveniently in a form similar to that of a two-dimensional Sersic (1968) light profile. Moreover, the lens properties for a Sersic (1968) profile are already derived in Cardone (2004), making it a straightforward procedure to map our parameters to those results. For completeness, we re-derive the lensing properties in a similar manner to Cardone (2004).

With the Σ_β profile (Equation 3.7), it is convenient to introduce a dimensionless variable $y := (R/R_{-1})^\beta$. The two-dimensional lens potential, $\psi(R)$, can be determined by solving the two-dimensional Poisson equation (e.g. Schneider et al. 1992):

$$\nabla^2\psi(R) = 2\,\kappa_\beta(R)\,, \tag{3.21}$$

where $\kappa_\beta(R)$ is the convergence profile for our model defined previously in Equation 3.18. Expanding out the two-dimensional Laplacian on the left-hand side to polar coordinates, the following change of variables transforms the differential equation as

$$y^{2\left(1-\frac{1}{\beta}\right)}\frac{\mathrm{d}^2\psi}{\mathrm{d}y^2} + y^{\left(1-\frac{2}{\beta}\right)}\frac{\mathrm{d}\psi}{\mathrm{d}y} = \frac{2\,R_{-1}^2\,\kappa_{-1}}{\beta^2}\exp\left[-\frac{1}{\beta}(y-1)\right]\,. \tag{3.22}$$

The above equation has the solution

$$\psi(y) = \psi_{-1}y^{\frac{2}{\beta}}\,{}_2F_2\left(\frac{2}{\beta},\frac{2}{\beta};1+\frac{2}{\beta},1+\frac{2}{\beta};\frac{y}{\beta}\right)\,, \tag{3.23}$$

where we have used the conditions that $\psi \to 0$ as $y \to 0$ or ∞, ${}_pF_q\left(a_1,\ldots,a_p;b_1,\ldots,b_p;z\right)$ is the generalized hyper-geometric function (Gradshteyn and Ryzhik 1980), and

$$\psi_{-1} := \frac{R_{-1}^2\kappa_{-1}}{2\,e^{1/\beta}} \tag{3.24}$$

is the value of the potential for $y = 1$.

3.4.5 Scaled deflection angle

Our lens profile model imposes circular symmetry. Therefore, the deflection angle is purely radial and will have a magnitude α given by $\mathrm{d}\psi/\mathrm{d}R$. The complete differentiation of the potential with respect to y gives

$$\alpha(y) = 2\,\alpha_{-1}\,y^{-\frac{1}{\beta}}\,\left[\Gamma\left(1+\frac{2}{\beta}\right) - \frac{2}{\beta}\,\Gamma\left[\frac{2}{\beta}, -\frac{y}{\beta}\right]\right], \tag{3.25}$$

where $\Gamma(x, a)$ is the incomplete Gamma function, $\Gamma(a)$ is the standard Gamma function, and

$$\alpha_{-1} := \frac{\left(-\frac{1}{\beta}\right)^{-\frac{2}{\beta}}}{e^{1/\beta}\,\beta}\,R_{-1}\,\kappa_{-1}\,. \tag{3.26}$$

3.4.6 Lensing shear

The radial dependence of a spherically symmetric system can be written as

$$\gamma_\ell(y) = \frac{\overline{\Sigma}(y) - \Sigma(y)}{\Sigma_\mathrm{c}}\,, \tag{3.27}$$

where

$$\overline{\Sigma}(y) = \frac{2}{y^2}\int_0^y \mathrm{d}y'\,y'\,\Sigma(y') \tag{3.28}$$

is the mean surface mass density inside the dimensionless radius y. For our lensing model, if we define $\tilde{y} := y^{\beta}/\beta$, the mean surface mass density is then

$$\overline{\Sigma}_{\beta}(\tilde{y}) = 2\,\Sigma_{-1}\exp\left(\frac{1-\beta\ln\beta}{\beta}\right)\frac{1}{\tilde{y}^{2/\beta}}\,\gamma\left[\frac{2}{\beta},\,\tilde{y}\right], \tag{3.29}$$

which gives us the shearing quantity in its compact form:

$$\gamma_{\ell}(y) = \kappa_{-1}\left\{\exp\left(\frac{1-\beta\ln\beta}{\beta}\right)\frac{2}{\tilde{y}^{2/\beta}}\,\gamma\left[\frac{2}{\beta},\,\tilde{y}\right] - \exp\left(-\tilde{y}+1\right)\right\}. \tag{3.30}$$

3.5 The impact of projection depth

A major component within the analysis done in this paper is how the mass is collected within a given a dark matter halo along the projection. Here, we treat the line-of-sight projection as a face-on-viewed cylinder, with a radius and length, $\mathcal{R}$ and $\mathcal{L}$. The total mass within this volume is denoted at the *effective mass*, $\mathcal{M}_{\rm eff}$, which is assumed to relate to $M_{\rm vir}$ in some way. In the main text, we chose the radius to be the size of the halo, $\mathcal{R} = r_{\rm vir}$, while we chose the cylinder length to be proportional to the halo virial radius $\mathcal{L} = 2\xi\, r_{\rm vir}$. The chosen value ξ plays a small part in inferring the effective mass. Indeed, as Figure 3.11 shows that the effective mass, based on our chosen cylinder volume, and the halo virial mass are roughly one-to-one, i.e., $\mathcal{M}_{\rm eff} \simeq M_{\rm vir}$ for most chosen values of ξ. Notably, as ξ increases, the scatter (which has reduced Poisson noise) for the lower-mass halos increases.

While the effective mass is consistent for different values of ξ, that is only one part of the complete story, where fortunately, the the inferred projected concentration is not impacted either. Figure 3.12 shows very little variance in the normalization of the mass function for the corresponding values of ξ previously shown in Figure 3.11. These projected concentration functions are compiled using our sample of zoom simulations, which has varying initial conditions, under-dense regions, as

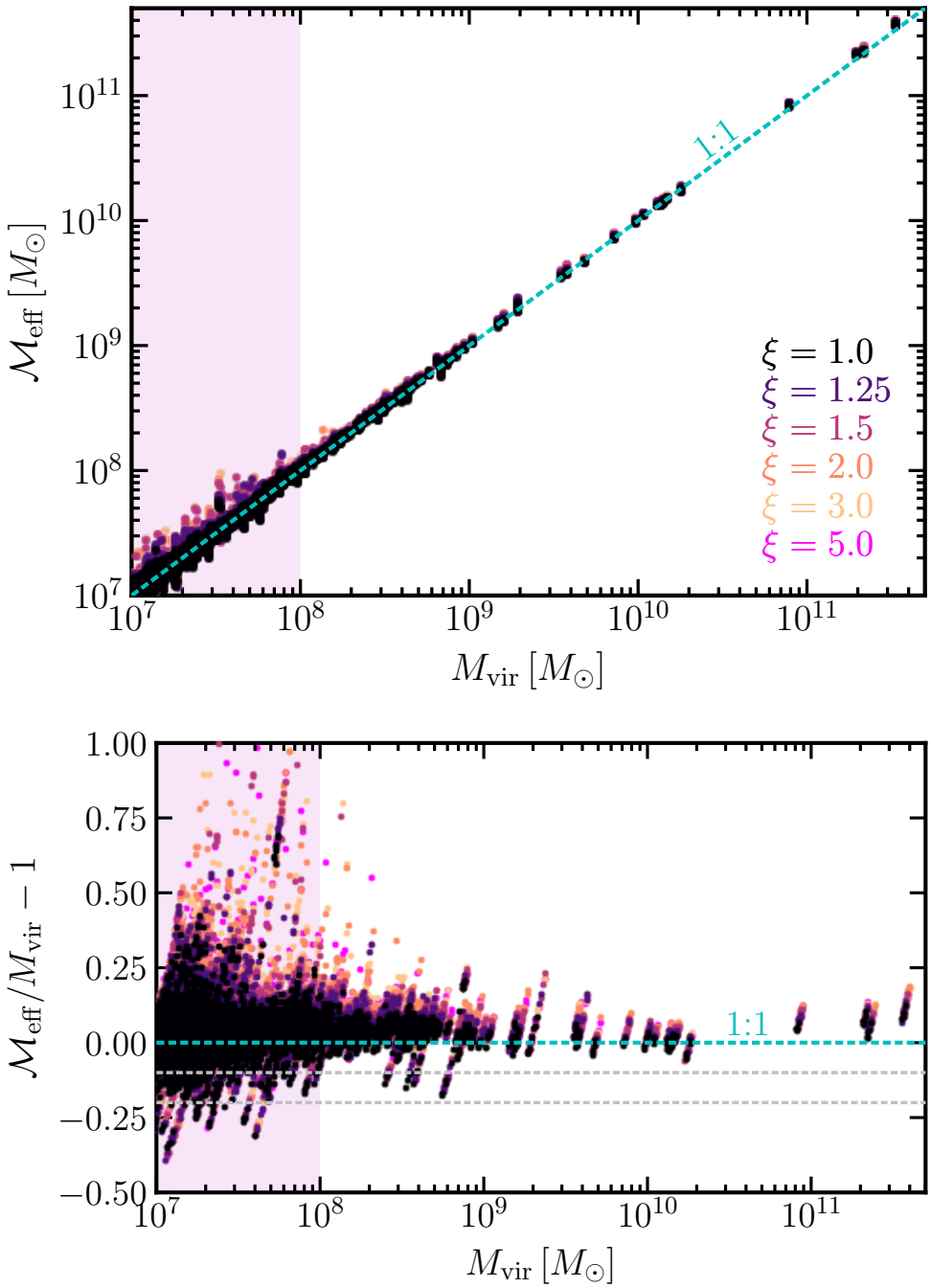

Figure 3.11: The virial mass plotted against the effective (projected) mass in multiple depths of projections for our chosen cylinder geometry: $\mathcal{L} = 2\xi\, r_{\rm vir}$. The color codes map to the value of ξ as shown. Note that the cylinder radius is fixed to be the virial radius. From the top plot, we see that the two masses are roughly be same. The cyan curve is a one-to-one relationship. The bottom plot shows residuals. The shaded pink band indicates the region where the convergence radius of each halo is larger than R_{-1}.

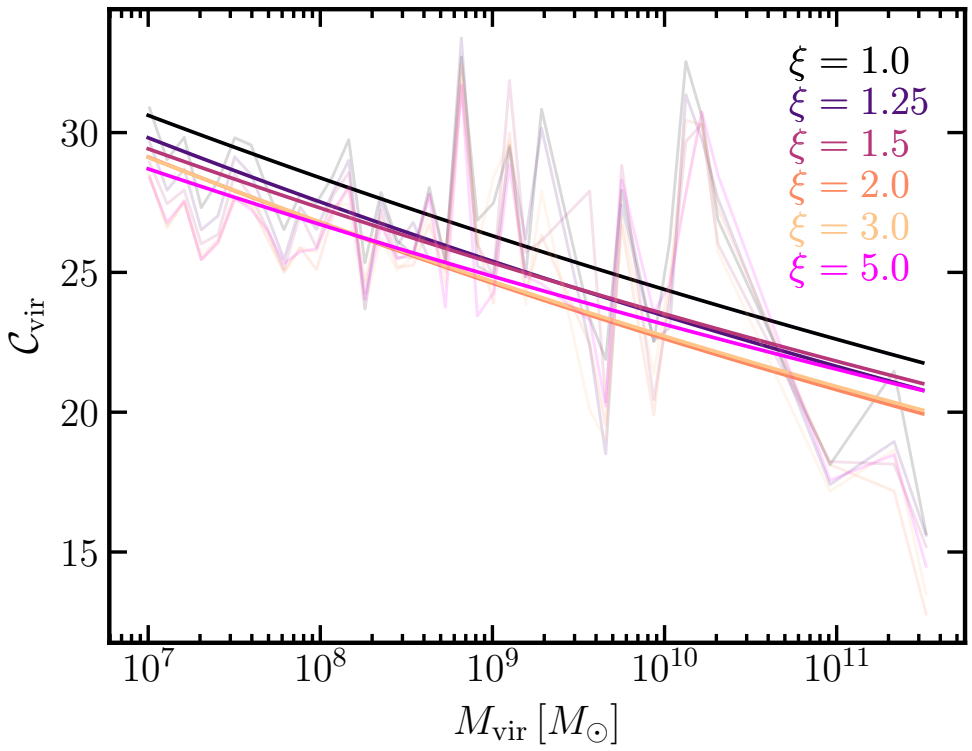

Figure 3.12: Same ξ values from the previous figure, now plotting the implied projected concentration-mass relations. No changes of the normalization are present.

compared to fully realized cosmological boxes, and a relation riddled Poisson noise; these results are to not to be taken as legitimate statistical relations and are plotted for demonstration purposes. The faded-solid lines depict the bin values of $C_{\rm vir}$ while the solid lines are power-law fits to these curves, as we want to emphasize the normalization values. As we increase to larger values of ξ, we see the normalizations remains relatively the same with slight adjustments of the slopes.

From both figures, it was decided to use a value of $\xi = 1.5$ as this is where the projected concentration and mass relation converges while also minimizing the scatter down at the low-mass range for the effective mass and halo mass relation (which otherwise large for $\xi = 2$).

3.6 Implications for gravitational lensing

Our primary motivation for characterizing the surface density profiles of dark matter halos is to provide a useful and accurate tool for gravitational lensing applications. As shown in section 3.4, the Σ_β profile given by Equation 3.7 has an analytic deflection potential, deflection angle, and lensing shear. One example use case is in the search for substructure within multiply-imaged quasar strong-lens systems. For example, the magnification ratios of images compared to those of a smoothly-parameterized mass distributions from a macro model provides a way to discover and characterize invisible dark matter halo perturbers (Mao and Schneider 1998, Metcalf and Madau 2001, Dalal and Kochanek 2002, Nierenberg et al. 2014, 2017, Gilman et al. 2020a,b, Hsueh et al. 2020).

Figure 3.13 shows an example of how the use of the $\Sigma_{0.3}$ profile gives different magnification predictions than an NFW profile fit for the same halo. For this calculation we use the open-source gravitational lensing software LENSTRONOMY[3], which performs the main lensing computations such as ray-tracing and magnifications (Birrer and Amara 2018, Birrer et al. 2021), combined with the open-source pyHalo[4], which generates realizations for subhalos and LOS halos within a lens system (Gilman et al. 2021). The left side of Figure 3.13 shows the projected surface density profile for an example $M \simeq 10^9\ M_\odot$ halo at $z = 0.2$ along the three primary projections (colored lines). The lines are truncated at the convergence radius for this simulation. Also shown is the implied surface-density profile for the best-fit (spherical) NFW profile for the same halo (solid black). The three solid colored lines show the best-fit $\Sigma_{0.3}$ profile fits for each projection. Note that he horizontal axis on the bottom shows projected radius in physical units (kpc) and on the top we show the same quantity in angular size for a $z = 0.2$ lens in seconds of arc.

The right panel depicts the relative magnification cross-sections compared to a smooth model for the three-dimensional NFW fit (thick, solid black line) and the three best-fit $\Sigma_{0.3}$ models for each

[3] https://github.com/sibirrer/lenstronomy
[4] https://github.com/dangilman/pyHalo

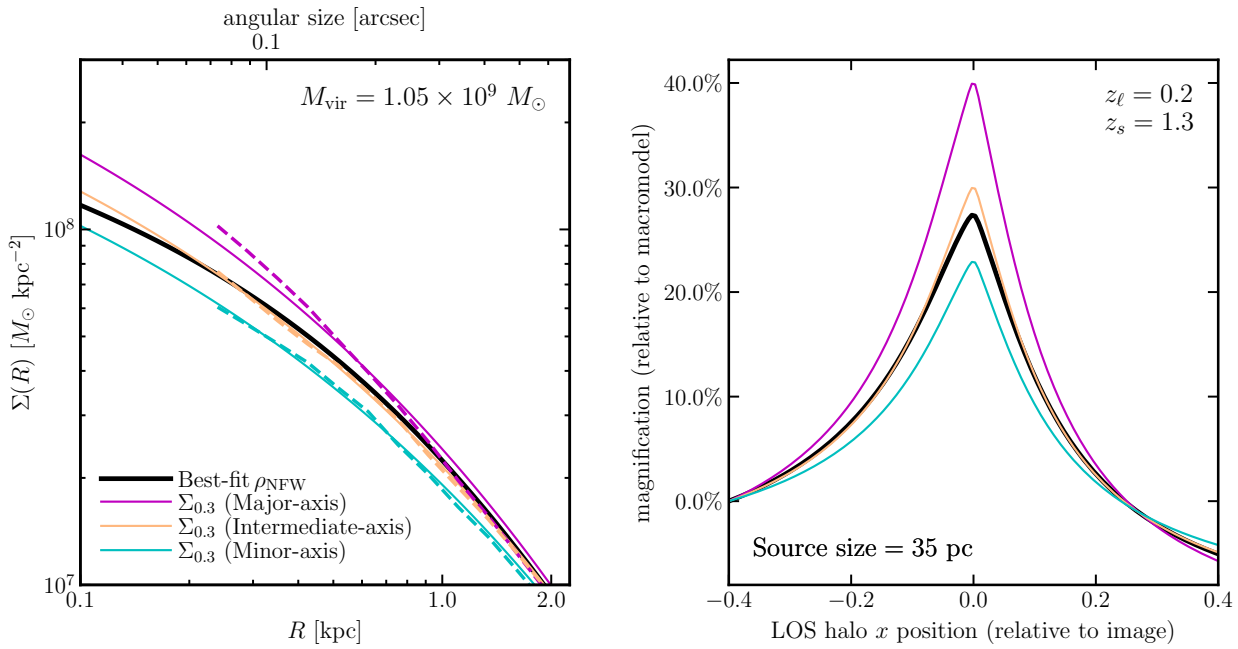

Figure 3.13: A demonstration of how inaccurate descriptions of the projected surface density for a $\simeq 10^8\ M_\odot$ dark matter halo can potentially impact strong lensing results. *Left*: the fitted dark matter surface profiles for this particular halo, where the solid black curve is the resulting best-fit $\rho_{\rm NFW}$ taken into projection, while the dashed color curves plot the simulated profiles along the three density axes, which includes their respective $\Sigma_{0.3}$ fits as the same-colored solid curves. *Right*: the magnification perturbation cross-section of the same halo using the left plot's analytical profiles. The $\Sigma_{0.3}$ profiles (colored curves) as LOS perturbers along the different density axis for this halo mass can greatly impact the lens image magnification. To match colored curves, one would need to select particular values of the NFW concentration or the halo mass.

orientation. The colored lines on the right panel were calculated using the analytic fits shown in the same color on the left. We assume a Gaussian source light distribution with a FWHM of 35 parsecs (comparable to the size of the nuclear narrow-line region of a quasar; e.g., Nierenberg et al. 2014, Müller-Sánchez et al. 2011) for a source redshift $z_s = 1.3$ and lens redshift $z_\ell = 0.2$. This figure is analogous to Figure 2 in Gilman et al. (2020a). The horizontal axis shows the perturber position relative to the image's position in arcseconds. The resulting change in magnification compared to a smooth-lens model is shown on the vertical axis.

We see that when a halo is projected along the densest and least-densest axis, relative magnification changes by a factor of ~ 2. The best-fit NFW density profile (black solid curve) fails to match these two extremes. This level of difference could bias the inferred parameters of the perturbing halo systematically at the $\sim 50\%$ level. For example, if we tried to interpret the major or minor axis orientations' magnification signals with NFW profiles of the same concentration, we would infer halos that are more or less massive than they actually are by factors of order unity.

3.7 Summary and concluding remarks

We have studied the surface density structure dark matter halos using a suite of dark matter only zoom simulations that contain halos of mass $M_{\rm vir} = 10^{7-11}\ M_\odot$. We find that their cylindrically-averaged surface density profiles along any projection can be modeled as a function of projected radius R using an easy-to-use, analytic profile, $\Sigma_{0.3}$, defined in Equation 3.7 with $\beta = 0.3$. The function has two free parameters: a scale radius R_{-1} and a normalization Σ_{-1}. A primary motivation is to provide a profile that is more accurate than a projected spherical NFW profile and that has analytic lensing properties that can be used in strong lensing studies for line-of-sight perturbing halos.

The common approach to modeling small-halo perturbers is to assume spherical NFW profiles

with properties drawn from mass-concentration relation predictions (e.g. Gilman et al. 2020b). As shown in Figures 3.2 and 3.4, the $\Sigma_{0.3}$ approach allows for significant improvement, with the same number of free parameters, especially at small projected radii, where the densities are highest and of most relevance for lensing perturbations. An important by-product introduced here is the *projected concentration*, defined by the size of the halo and the projected scale radius, $C_{\rm vir} := r_{\rm vir}/R_{-1}$. For any individual halo, the projected concentration can be higher or lower depending on the projected orientation. By fitting halos along an ensemble of orientations, the projected concentration provides a way to statistically account for asphericity while still utilizing a two-parameter foundation. The the projected concentration correlates with the standard three-dimensional concentration in a way that allows ease of use (Figures 3.8 and 3.9).

In order to illustrate implications for gravitational lensing, we set up a mock-lensing analysis to explore the implied perturber magnification with the $\Sigma_{0.3}$ model compared to the standard NFW approach (Figure 3.13). In this exercise, we examined the projected density structure of an example halo along three primary density axes and showed that the implied magnification perturbation as captured by $\Sigma_{0.3}$ fits for different orientations give as much as $\sim 50\%$ relative differences compared to the same halo's NFW fit at fixed mass. Flux ratio studies of lensing by halos draw populations of halos with halo to halo scatter in the mass-concentration relation. To studying the impact of the orientation observed in this work on a full dark matter inference would require full simulations of gravitational lenses. However we can see that the effect should in principle be similar to increasing the "effective scatter" in the lensing mass-concentration relation (Gilman et al. 2020a,b). We leave a detailed analysis of this to a future work.

One weakness of this analysis is that we have relied on zoom simulations, and not a fair cosmological sample. A next step in this analysis will be to use cosmological samples of simulated halos to provide statistically meaningful predictions for effective concentration distributions as a function of halo mass. We expect that the relative relationships we have found between the three-dimensional concentration and effective (projected) concentrations for our halos will be robust. From the

analysis done here, the average mapping obeys $C_{\rm vir} = 2.3\, c_{\rm vir}^{0.87}$ (Figure 3.8) with a Gaussian scatter of $\sigma \simeq 0.2$ at fixed $c_{\rm vir}$ for any individual halo. The work done the next chapter tests these expectations in a fair cosmological context.

Chapter Acknowledgements

Part of this research was carried out at the Jet Propulsion Laboratory, California Institute of Technology, under a contract with the National Aeronautics and Space Administration. The authors thank the FIRE collaboration for the use of the DMO zoom simulations for our analysis. Support came from the National Science Foundation (NSF) grant AST-1910965 and from the NASA grant 80NSSSC20K1469.

Chapter 4

The scatter and evolution of the projected concentration for line-of-sight halos

The line-of-sight (LOS) population of dark matter halo perturbers are an important contribution to lensing signals diagnosed in gravitational lensing studies. The density profiles of the LOS population are commonly described by fitting functions such as the NFW or Einasto models, but these approximations tend to break down when modeling the projected surface density from halo-to-halo. Chapter 3 proposed a simple, accurate fitting function designed to robustly model the surface mass-density of LOS halos expected in ΛCDM, which are parameterized by the so-called *projected concentration* (see previous chapter in its significance). Here we extend this surface density model for the LOS population by studying dark matter halos in a high-resolution N-body simulation of a ΛCDM cosmology, which contains a statistical sample of $\sim$ 250,000 halos in the mass range of $10^{8-11}\ h^{-1}M_{\odot}$ at $z = 0$. This sample allows us to present several statistical functions applicable for describing a population LOS halos for lensing studies, mainly the evolution of the projected concentration and the scatter, from redshift ranges of $z = 0 - 3$.

4.1 Chapter context

Structure formation within the ΛCDM (dark energy + cold dark matter) cosmological paradigm arises hierarchically, wherein small peaks within the density field collapse first and, in due course, overdensities on larger scales collapse and generate mergers (e.g., Zavala and Frenk 2019, Angulo and Hahn 2022). Owing to the scale-free nature of structure formation, cosmological N-body simulations have revealed that the local, spherically-averaged density profiles of dark matter halos exhibit self-similarity across a wide range of halo masses, cosmologies, and redshifts (Navarro et al. 1996, Moore et al. 1999, Huss et al. 1999, Bullock et al. 2001, Wechsler et al. 2002, Neto et al. 2007, Knollmann et al. 2008, Wang and White 2009, Ludlow and Angulo 2017, Bullock and Boylan-Kolchin 2017, Brown et al. 2022). As first pointed out by Navarro et al. (1996) (hereafter, NFW), dark matter only (DMO) halos within ΛCDM manifest as a simple double power-law profile. The NFW profile has been widely popular over the decades in cosmological studies of dark matter halos, as it depends on two parameters, a characteristic radius and density, to fully generate the density structure.

As a result of large-scale cosmology simulations, the NFW profile is self-similar for all halo mass ranges, and the density structure can be more sufficiently obtained by recasting these parameters in terms of the halo mass and the halo concentration, which is a ratio between the size of the halo and its scale radius. The halo mass and concentration are anti-correlated within N-body simulations, which reflects the epoch of collapse for the halo, where low-mass halos with higher concentrations are a product of the higher background density during the early times of the Universe when most of these small overdensities have collapsed (Navarro et al. 1997). This complex relationship has led to a plethora of studies of the so-called concentration-mass relation by analyzing the relationship between halo mass and concentration, and how it evolves as a function of redshift and cosmology (e.g., Bullock et al. 2001, Dolag et al. 2004, Duffy et al. 2008, Klypin et al. 2011, Prada et al. 2012, Bhattacharya et al. 2013, Dutton and Macciò 2014, Ludlow et al. 2014, Diemer and Kravtsov 2015, Klypin et al. 2016, Child et al. 2018, Diemer and Joyce 2019, Ishiyama et al. 2021).

The potential to accurately infer the halo concentrations of a given halo mass has countless applications to astrophysics. These examples include inferring the gamma-ray signals potentially generated by dark matter annihilation events (e.g., Sánchez-Conde and Prada 2014, Okoli et al. 2018), approximating the merger rates of primordial black holes (e.g., Mandic et al. 2016), and enhance the execution of cosmological rescaling algorithms (e.g., Angulo and White 2010, Contreras et al. 2020, López-Cano et al. 2022). One other astrophysical application, that this paper is also motivated by, is how well halo concentrations predict the galaxy-galaxy strong lensing signal associated with subhalos and, which this analysis focuses on, "line-of-sight" (LOS) halos in the field (e.g., Fedeli et al. 2007, Despali et al. 2018, Gilman et al. 2019, 2020a, Amorisco et al. 2022).

A key predictor of the Universe being ΛCDM is that is richly populated with very low-mass dark matter halos ($\lesssim 10^9\ M_\odot$) (Press and Schechter 1974, Green et al. 2005, Diemand et al. 2007, Springel et al. 2008, Frenk and White 2012). If halos with these low masses exists, they can act as significant perturbers for lensing studies, but given that stellar feedback is expected to be inefficient in modifying the inner-density structure compared to DMO predictions (e.g. Lazar et al. 2020), these nearly starless dark halos have yet to be observationally confirmed. We can instead expect to infer the existence of starless dark matter halos through their gravitational signatures in a strong lensing setting (Dalal and Kochanek 2002). Indeed, as the concentrations of low-mass substructure, and potentially line-of-sight halos, strongly impacts signals within lens systems. Minor et al. (2021a) demonstrated that the perturbations of strongly lensed images by low-mass dark matter subhalos are significantly impacted by the concentration of the perturbing subhalo in a ΛCDM cosmology.

It is encouraging that many concentration-mass relation models within the literature exist, yet successfully describes the median behavior and scatter seen in various cosmological simulations. Several ideas pertaining to the assembly history of NFW halos to construct age based models (e.g., Navarro et al. 1996, 1997, Bullock et al. 2001, Eke et al. 2001, Wechsler et al. 2002, Zhao et al. 2003, 2009, Lu et al. 2006, Dalal et al. 2010, van den Bosch et al. 2014, Correa et al. 2015), several methods by modeling the relation via power-law fits or simpler functions (e.g., Avila-Reese et al.

1999, Dolag et al. 2004, Neto et al. 2007, Duffy et al. 2008, Gao et al. 2008, Klypin et al. 2011, Bhattacharya et al. 2013, Dutton and Macciò 2014, Klypin et al. 2016, Child et al. 2018), and recently more physical motivating models (Diemer and Joyce 2019). In the context of substructure lensing, the numerous amount of concentration-mass models leaves very little room for accurate analysis when determining a ensemble of realized halos within lens systems, as most models are only fitted down to masses of $M_{\rm halo} \simeq 10^9\ M_\odot$, while halos of $M_{\rm halo} \lesssim 10^8\ M_\odot$ are objects of interest. Power-law fits have demonstrated to predict wrong concentrations when extrapolated to low halo masses (Ludlow et al. 2014). Moreover, such fitting functions are only correct for the cosmology and redshift at which they were constrained. The Diemer and Joyce (2019) model is motivated by physical characteristics that alleviates these shortcomings, such as accommodating the redshift, cosmology, and low-mass extrapolations. However it should be questioned whether NFW halos are the most practical way to model LOS perturbers.

The previous chapter proposes an alternative way to model LOS perturbers for strongly lensed lensing studies. We introduced an analytical surface density profile for dark matter halos that more accurately reproduces the structure of simulated halos of mass ranges within $10^{7-11}\ M_\odot$. This surface-density profile is a two-parameter function was found to be more accurate than the projected NFW profile used at the mass scale for lensing perturbers. Importantly, it was found to more accurate at modeling the inner-most regions for different projection orientations in a hale-to-halo case. A convenient way this could be characterized was through the so-called projected concentration, which was the ration between the halo size and projected scale radius. In this chapter, we extend the utility of this formalism by applying the Σ_β function to a cosmological simulation in order to determine and provide functional, and statistical, relations applicable for lensing studies, i.e., the *scatter* and the *project concentration-mass relation*.

This work makes use of a simulated cosmological box of unprecedented resolution to gather the required statistics for halo masses down to $\sim 10^7\ M_\odot$. Unlike previous work in the literature of concentration relations, this analysis is done under the context of substructure lensing. Therefore,

we restrict our analysis of halos within the mass range $M_{\rm halo} \in 10^{8-11}\,M_\odot$ from redshifts $z = 0-3$, as most of these masses are the most abundant and internally resolved at these redshifts. Additionally, we implement a physically-motivating model that allows to confidently extrapolate our results down to masses of $\sim 10^6\,M_\odot$. We only consider halos in the field, i.e., no subhalos; While subhalos are an important component in modeling for lensing, the LOS contribution, are arguably more important in contributing to lensing signals (Metcalf 2005, Inoue and Takahashi 2012, Inoue et al. 2015, Inoue 2016, Lazar et al. 2021).

This chapter is structured as follows: Section 4.2 introduces our cosmological simulation, defines our halo and structural properties, and outlines our methodology for measuring the concentration and projected concentrations of our sample. Section 4.3 briefly explores the mass-concentration of our halo sample. Section 4.4 presents our projected concentration-mass relations for our dark matter halo sample and provides a well-motivating fitting function for the relation over the redshifts explored. Finally, we summarize our results in Section 4.5.

Note that in strong lensing literature, terms such as "field halo" and "line-of-sight" (LOS) halo' typically refer to the same objects. These terms will be used interchangeably throughout this work to refer to halos having a volume density equal to the cosmological mean density of halos at that mass. For historical purposes, we will usually express halo masses with the factor of h, but will occasionally quote values that include these factors.

4.2 Methodology

4.2.1 Cosmological *N*-body simulation: FIREbox

The FIREbox suite of simulations are ran with cosmological volumes of box length $L_{\rm box} = 15\,h^{-1}$cMpc $= 22.14$ cMpc at the resolutions comparable to the FIRE 'zoom-in' simulations (Feldmann et al. 2022). These simulations are ran using the multi-method code GIZMO (Hopkins 2015), which uses a second-order mesh-free Lagrangian-Godunov finite mass (MFM) method for hydrodynamics. An updated version of the PM+Tree algorithm from GADGET-3 (Springel 2005) is used to calculate gravity. We use the results from the high-resolution dark matter only (DMO) version of FIREbox for a standard ΛCDM cosmology. We do not consider the affects of baryons here and withhold their impact for future analysis. The initial conditions for the high-resolution DMO version were generated with 2048^3 particles using MUSIC (Hahn and Abel 2011) at starting redshift of $z \approx 100$ assuming a Planck 2015 cosmology (Planck Collaboration et al. 2016b): $\Omega_{\rm m} = 0.3089$, $\Omega_\Lambda = 0.6911$, $\Omega_{\rm b} = 0.0486$, $\sigma_8 = 0.8159$, $n_s = 0.9667$, and $h = 0.6774$. FIREbox has a particle mass $m_{\rm dm} = 5 \times 10^4\,M_\odot$ with a Plummer softening length of $\epsilon_{\rm dm} = 40$ pc.

The cosmological box is able to resolve down to halo mass of $\approx 10^8\,M_\odot$ that contain ~ 1000 dark matter particles, which allows us to resolve the internal structure. In post-processing, dark matter halos are identified using the Amiga halo finder (AHF; Knollmann and Knebe 2009). The halo finder uses a recursively refined grid that determines the local overdensities found within the density field and identifies the density peaks of this field as the center of these halos. The AHF algorithm is known to be fully recursive in identifying host halos and there substructure (Gill et al. 2004, Onions et al. 2012). Halos are primarily identified as spherical overdensities using the Bryan and Norman (1998) definition, which is specified more in the next in Section 1.2.2. Figure 4.1 presents the halo mass function for all of the virial masses (in units of h) ranging from redshifts $z = 0$ to 3. The post-processing results are compared to the analytical predictions (dashed curves) of Sheth and Tormen (2002). The simulations are in good agreement with predictions, though the $z = 3$ FIREbox curve

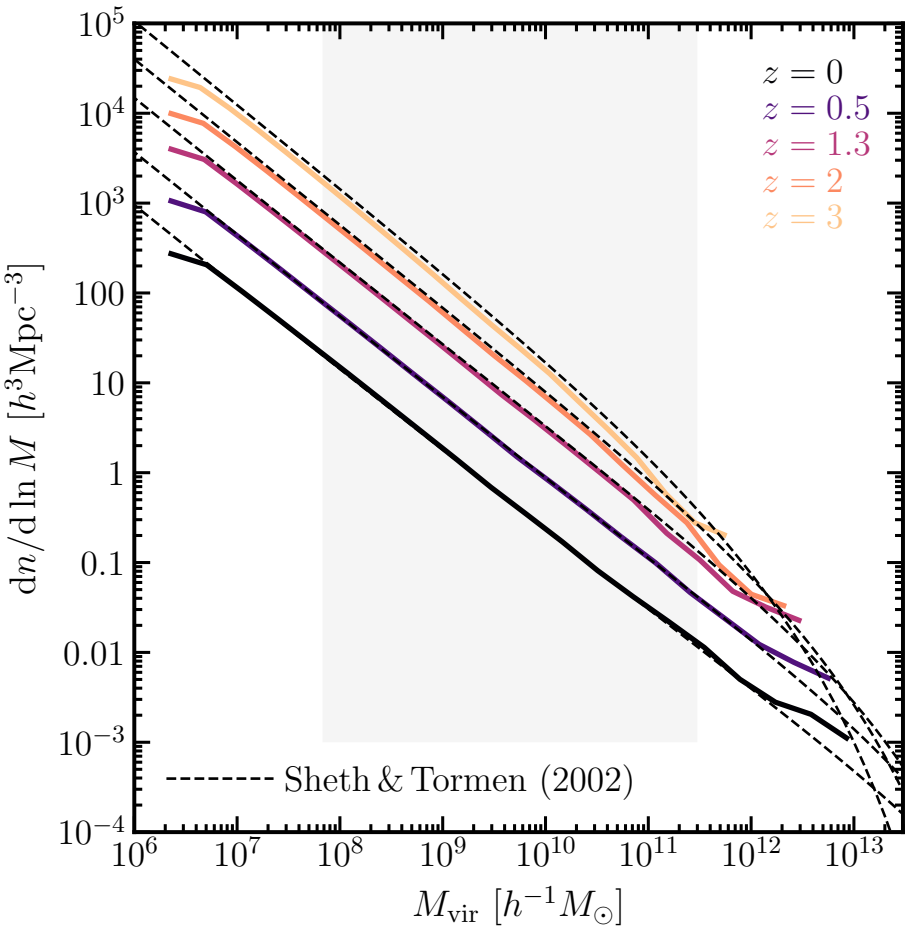

Figure 4.1: The abundance of resolved low-mass, dark matter halos. Shown are the halo mass functions FIREbox for the redshifts explored in this paper. Results at these snapshots are in agreements analytical predictions of Sheth and Tormen (2002), shown as the dashed curves. The gray band encapsulates the structurally resolved masses we model here.

has a lower amplitude than what is theoretically predicted. The gray band encapsulates the range of halos we are model here: $M_{\mathrm{vir}} \simeq 10^{8-11}\ M_\odot$, or equivalently, $M_{\mathrm{vir}} \simeq 0.6774 \times 10^{8-11}\ h^{-1}M_\odot$. The colored curves compared to the dashed curves within the gray band indicates that most of halo masses of interest are well resolved. Though at $z = 3$, halos with $M_{\mathrm{vir}} \gtrsim 10^{10}\ h^{-1}M_\odot$ are rare. At this redshift, we restrict the analysis of these halos to $M_{\mathrm{vir}} = 10^{10}\ h^{-1}M_\odot$.

4.2.2 Chapter nomenclature

This section provides definitions of the global and physical quantities of dark matter halos that are relevant for this work. Herein and so forth, lower case r is denoted as the physical, (de-projected) three-dimensional radius. In two-dimensions, the projected physical radius is denoted by an upper case R.

Isolated halo definition

Dark matter halos are defined to be a spherical overdensities with mass, M_{Δ}, contained within a radius, r_{Δ}, that encloses some density contrast, Δ, relative to a reference background density at a particular redshift, $\rho_{\rm ref}(z)$, such that the interior density for the halo is, $\rho_{\Delta} = \Delta\,\rho_{\rm ref}(z)$ (Equation 1.1). Throughout this chapter, we primarily define the dark matter halos by their virial mass, $M_{\rm vir}$, which are spherical systems with virial radius, $r_{\rm vir}$, inside of which the average density is equal to the virial density, $\rho_{\rm vir}(z)$ (Equation 1.3). Here, the virial density is redshift evolving and is defined from Bryan and Norman (1998), where $\rho_{\rm c}$ is the critical density of the universe at redshift z. The Bryan and Norman (1998) definition is used for the AHF halo finding, but as noted within Section 1.2.2, dark matter halos are also commonly defined with overdensity $\Delta = 200$ with either a critical or mean-matter background densities. We also explore halo masses with the commonly adopted spherical overdensity $\Delta = 200$ (Equation 1.8). A benefit of this halo definition, compared to virial overdensity definition, is that it is less dependent on the underlying cosmology. Note that while post-processing identifies dark matter halos using the Bryan and Norman (1998) definition with AHF, we do not use these results. With the centers of the spherical overdensities determined, the masses $M_{\rm vir}$ and $M_{\rm 200c}$, along with their radii, are recomputed using *all* of the dark matter particles, i.e., bound and unbound particles. This is detailed more in Section 4.2.3.

Three-dimensional structure of dark matter halos

The three-dimensional density profiles of dark matter halos in ΛCDM historically are modeled by the Navarro et al. (1996) (NFW) profile (Equation 1.12. For higher-resolution, dark matter only simulations, dark matter halos have been demonstrated to be well described by the Einasto profile (Navarro et al. 2004, 2010) for 20 decades of halo masses (Equation 1.14). The scale radius is denoted as r_{-2}, which is the radius where the log-slope profile is equal to -2, the scale density is $\rho_{-2} := \rho(r_{-2})$, and the shape parameter is α_ϵ. Usually α_ϵ is fixed to eliminate its dependencies on values of r_{-2}, but could be expressed in terms of peak height (e.g. Prada et al. 2012, Dutton and Macciò 2014, Child et al. 2018). We fix $\alpha_\epsilon = 0.17$ for this analysis, which is close to fitting well for the range of halo masses we explore here (Wang et al. 2020). The internal structure is parameterized by the dimensionless concentration parameter for the two mass definitions explored:

$$c_{\rm vir} := \frac{r_{\rm vir}}{r_{-2}}; \qquad c_{\rm 200c} := \frac{r_{\rm 200c}}{r_{-2}}\,. \tag{4.1}$$

Two-dimensional structure of dark matter halos

It was established in Chapter 3 that high-resolution dark matter halos in projection are more robustly modeled by the generalized profile:

$$\Sigma_\beta(R) = \Sigma_{-1} \exp\left\{ -\frac{1}{\beta}\left[\left(\frac{R}{R_{-1}}\right)^\beta - 1\right]\right\}, \tag{4.2}$$

where $\Sigma_{-1} := \Sigma(R_{-1})$ and R_{-1} are the scale surface-mass density and scale radius where the log-slope is equal to -1. Here, we once again fix $\beta = 0.3$ and refer to this specific profile shape as $\Sigma_{0.3}$. Once the dependence of the shape parameters is resolved, the *projective concentration* seen from

the dark matter halo in projection is:

$$C_{\rm vir} := r_{\rm vir}/R_{-1}; \qquad C_{\rm 200c} := r_{\rm 200c}/R_{-1}\,. \tag{4.3}$$

Note that C_Δ also depends on the orientation of the dark matter halo in projection, due to the dependence of R_{-1} (see main results presented in Chapter 3).

4.2.3 Radial profiling and halo concentrations

Construction of the dark matter halo density profiles in three dimensions and two dimensions is done the same way as described previously in Section 3.2.3. One of the key components of our analysis focuses on the spherically averaged mass profiles. As an initial procedure for each halo, radial bins are constructed and the dark matter particles are first shifted relative to the halo center determined by AHF. The innermost regions of cosmological N-body simulated dark matter halos, to some extent, are impacted by numerical relaxation. The region of convergence $r_{\rm conv}$, is quantified using the method specified in Power et al. (2003), where the effective resolution of the simulations dictates the location of the radius where the two-body relaxation timescale, $t_{\rm relax}$, becomes shorter than the age of the universe, t_0, set by the criterion:

$$\frac{t_{\rm relax}(r)}{t_0} = \frac{\sqrt{200}}{8}\frac{N(<r)}{\ln N(<r)}\left[\frac{\bar{\rho}(<r)}{\rho_{\rm c}(z)}\right]^{-1/2}, \tag{4.4}$$

where $N(<r)$ is the cumulative number of particles within radius r and the cumulative density profile, $\bar{\rho}(<r) = 3M(<r)/4\pi r^3$, with $M(<r)$ being the cumulative mass. For N-body simulations of our resolution, convergence is shown to be well resolved to the radius at which the criterion satisfies $t_{\rm relax} > 0.6\,t_0$ with <1% resolution level deviations for isolated zoom runs (see Hopkins et al. 2018). This convergence criterion should also be consistent with the resolution of the FIREbox simulation.

Three-dimensional profiles

With the centers of each spherical overdensity identified with AHF, all particles are counted in radial shells construct 35 radial bins logarithmic spaced by r from $r_{\rm conv}$ to $r_{\rm vir}$ of each halo. The mass and radius $M_{\rm vir}$ and $r_{\rm vir}$ are calculated using the Bryan and Norman (1998) overdensity define previosly. Additionally, $M_{\rm 200c}$ and $r_{\rm 200c}$ are also calculated. No unbound particles are removed because we are interested in underlying the density profile as measured. We are fully aware that our sample contains relaxed and unrelaxed halos, where the concentration for some halos are ill-defined.

For each halo, we fit the Einasto profile to their local density profile using all of the dark matter particles found within $r_{\rm vir}$. The local density profile, $\rho(r)$,is defined as the total dark matter mass found in each bin divided by the spherical shell. The best-fit parameters are determined by the following minimizing the figure-of-merit in a non-linear least-squares optimization:[1]

$$Q^2_\rho = \frac{1}{N_{\rm bins}} \sum_i^{N_{\rm bins}} \left[\log\left(r_i^2 \rho_i\right) - \log\left(r_i^2 \rho_i^{\rm model}\right) \right]^2 . \tag{4.5}$$

Like we have done in Chapter 3, the $r^2\rho(r)$ merit provides a more balanced indicator of goodness-of-fit throughout the entire radial range. Each individual fit records the best-fit parameters for the Einasto profile with fixed $\alpha_\epsilon = 0.17$. From each fit, we obtain r_{-2} and then quantify $c_{\rm vir}$ and $c_{\rm 200c}$.

Two-dimensional profiles

Detailed previously in Chapter 3, we consider the projection of a dark matter halo to a be a cylinder looked face-on, in which it has a radius $\mathcal{R}$ and length (or depth in this orientation), $\mathcal{L} = L_{\rm depth}$. For a given orientation of projection, we have the cylinder radius to be the size of the halo $\mathcal{R} = r_\Delta$ while the cylinder depth is a factor (ξ) of the halo radius, $L_{\rm depth} = 2\,\xi\, r_\Delta$. Within this volume contains all of the bound and unbound dark matter particles of the halo. We construct the projected local

[1]The convention used here in this chapter is $\log \equiv \log_e \equiv \ln$.

surface-density profile using circular bins from $r_{\rm conv}$ to $r_{\rm vir}$ using 35 radial bins that logarithmicly spaced by R. The convergence radius $r_{\rm conv}$ is chosen as a minimum radius to remain conservative. This is done in ten random orientations from halo-to-halo to capture the statistics based on the shape. In Chapter 3, we considered a one-to-one relation to the halo's virial radius; since we are interested in the underlying projected surface density profile as a product of a cosmological environment, we set $\xi = 1.5$, as this nicely captures the shapes of the accretion and splashback particles otherwise not incorporated to a depth out to "halo boundary" r_{Δ} while also minimizing the Poisson noise within circular shells for the lower-mass halos. For context, *this analysis is done in the setting of substructure lensing*, where the total matter content in a line-of-sight projection greatly influences the lensing signal. This entire procedure is repeated for both definitions we explore for out halo sample: $r_{\rm vir}$ and $r_{\rm 200c}$.

Each constructed surface-density profile is fitted to Equation 4.2 within $R < r_{\Delta}/2$, as we interested in the shapes in the inner-most regions. The best-fit parameters are determined by the following minimizing the figure-of-merit in a non-linear least-squares optimization:

$$Q_{\Sigma}^{2} = \frac{1}{N_{\rm bins}} \sum_{i}^{N_{\rm bins}} \left[\log\left(R_i \Sigma_i\right) \; - \log\left(R_i \Sigma_i^{\rm model}\right) \right]^2 . \tag{4.6}$$

From each fit in given a orientation, we obtain R_{-1}, which we use to recover the respective projected concentrations.

4.3 The concentration-mass relation of low-mass halos

This section presents a brief analysis of the halo concentrations inferred from best-fit Einasto profiles of the FIREbox sample.

4.3.1 A physically mass-motivating concentration model

The Diemer and Joyce (2019) the halo concentration model is of the analytical form:

$$c = C(\alpha_{\rm eff}) \times \widetilde{G}\left(\frac{A(n_{\rm eff})}{\nu}\left[1 + \frac{\nu^2}{B(n_{\rm eff})}\right]\right) . \tag{4.7}$$

Here, the *peak height*, ν, is quantified from the halo mass and associated redshift, and is a universal variable characterized by the cosmology:

$$\nu := \frac{\delta_{\rm c}}{\sigma(M,z)} = \frac{\delta_{\rm c}}{\sigma(M,0) \times D_+(z)} , \tag{4.8}$$

where $\delta_{\rm c} = 1.686$ is the critical overdensity for top-hat collapse in an Einstein-de Sitter universe, the normalized linear growth factor is expressed as

$$D_+(z) = \frac{5}{2}\Omega_{\rm m} E(z) \int_z^\infty dz' \frac{1+z'}{E(z')^3} \tag{4.9}$$

for a ΛCDM cosmology (Heath 1977, Peebles 1980), such that $E(z)$ encodes the evolution of the cosmological parameters. The rms variance of the density field, σ, is quantified in a sphere of the Lagrangian radius of a given mass, $R(M)$, i.e.,

$$\sigma^2(R,z) = \frac{1}{2\pi^2}\int_0^\infty dk\, k^2 P(k,z) |\widetilde{W}(kR)|^2 , \tag{4.10}$$

where the linear power spectrum, $P(k)$, that assumes a transfer function that follows Eisenstein and Hu (1998) and $\widetilde{W}$ is a window filter function in the form of a top-hat in real space.

The function $\widetilde{G}$ is the inverse function of

$$G(x) = \frac{x}{[g(x)]^{(5+n_{\rm eff})/6}} , \tag{4.11}$$

which is dependent on, $g(x)$, the characteristic density function derived by the enclosed mass of the density profile, i.e.,

$$M(< r) = 4\pi\rho_s r_s^3 g(x)\,. \tag{4.12}$$

Diemer and Joyce (2019) and Ishiyama et al. (2021) explored this functional model by halos described by as a NFW, which has the characteristic density structure of

$$g(x) = \log(1+x) - \frac{x}{1+x}\,, \tag{4.13}$$

with $x = r/r_s$. Analogous to the NFW, the characteristic density for the Einasto profile is (Klypin et al. 2016):

$$g(x) = e^{\frac{2}{\alpha\epsilon}} \int_0^x \mathrm{d}x' x'^2 e^{-\frac{2}{\alpha\epsilon}x'^{\alpha}}\,, \tag{4.14}$$

now with $x = r/r_{-2}$. Again we impose that fact that $r_s \simeq r_{-2}$.

The other variables in Equation 4.7, $\alpha_{\rm eff}$ and $n_{\rm eff}$, encode the cosmology for this relation, and are defined as follows:

$$\alpha_{\rm eff}(z) = -\frac{\mathrm{d}\ln D_+(z)}{\mathrm{d}\ln(1+z)}\,, \tag{4.15}$$

which is the effective slope of linear growth factor, $D_+(z)$, and

$$n_{\rm eff}(M) = -2\,\frac{\mathrm{d}\ln\sigma(r)}{\mathrm{d}\ln r}\bigg|_{r=\kappa\,R_{\rm L}} - 3\,, \tag{4.16}$$

which is the effective slope of the power spectrum via $\sigma(r)$ with spheres the size of the Lagrangian

radius,

$$M = \frac{4\pi}{3}\rho_{\rm m}(z=0)\, R_{\rm L}^3\,, \tag{4.17}$$

that is calibrated to r using the free parameter, κ. The other expressions are assumed to have the following form

$$\begin{aligned} A(n_{\rm eff}) &= a_0\,[1 + a_1(n_{\rm eff}+3)]\ , \\ B(n_{\rm eff}) &= b_0\,[1 + b_1(n_{\rm eff}+3)]\ , \\ C(\alpha_{\rm eff}) &= 1 - c_\alpha(1-\alpha_{\rm eff})\,. \end{aligned} \tag{4.18}$$

where a_0, a_1, b_0, b_1, and c_α are free parameters. In total, Equation 4.7 has six free parameters in the fit.

4.3.2 The concentration-mass relation of low-mass halos

The relationship between the halo mass and concentration parameter for isolated field halos have been exhaustively studied throughout the literature. We do not provide more of an extensive analysis on it other than what has already been done, but unlike most works, we have uniquely modeled our high-resolution dark matter halos using the Einasto profile, which has not been modeled as extensively in a cosmological simulation compared to the typical NFW halos.

Figure 4.2 presents the low-mass halo concentrations for the Einasto profile (with fixed $\alpha_\epsilon = 0.17$) for redshifts up to $z = 3$. The left panel shows the median $c_{\rm vir}$ compared to $M_{\rm vir}$ given by the data points while the right panel shows the median $c_{\rm 200c}$ compared to $M_{\rm 200c}$ extrapolated from the profile fits. The error bars encapsulates 68% of the concentration distribution found in each mass bin. The values of $c_{\rm vir}$, compared to values of $c_{\rm 200c}$, evolves strongly with redshift. While not shown here, the analytical concentration relation matches well with the median $c_{\rm vir}$, though their $c_{\rm 200c}$ predictions

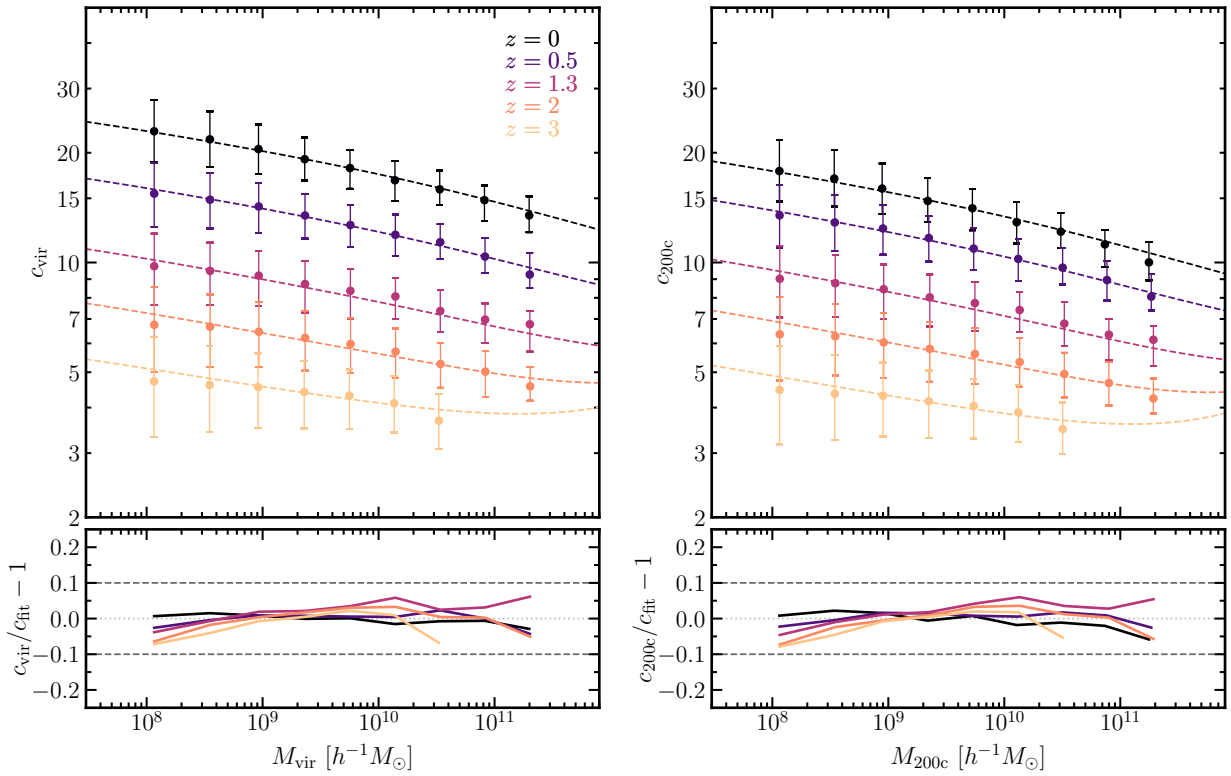

Figure 4.2: The concentration-mass relations for low-mass, line-of-sight dark matter halos from $z = 0 - 3$. *Top panels:* The points give the median concentration found within the binned values of mass for both mass definitions ("virial" and "200c" in left and right panels, respectively). The error bars encompass 68% of the concentrations as measured in the simulation. The dashed curves model the median values using Equation 4.7 for each mass definition. *Bottom panels:* The quality of the analytical fit over our redshift sample. The analytical functions are accurate to ∼5% and better over our explored mass ranges.

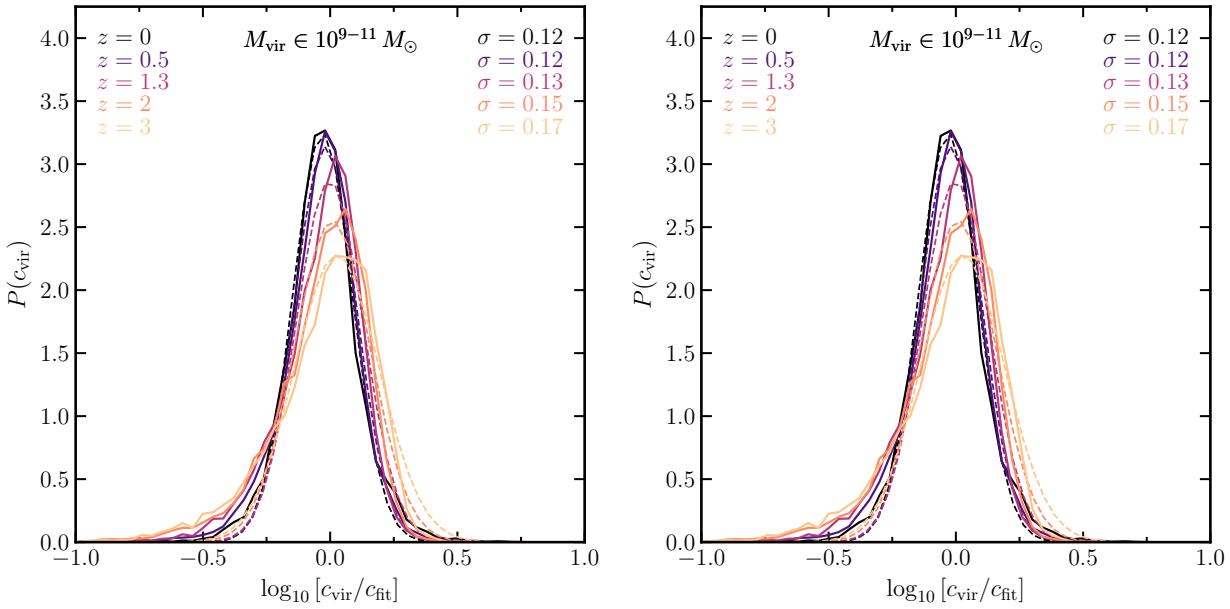

Figure 4.3: The scatter in the halo concentrations as a function of redshift for halos within the mass range $M \in 10^{9-11}\ M_\odot$. We detail the reason for this limited mass range in the next section. The scatter (solid curves) at each redshift are well described by a log-normal distribution (dashed curves).

Table 4.1: Best-fitting parameters of the concentration-mass relation for the Diemer and Joyce (2019) model (Equation 4.7) using the Einasto density profile with the shape parameter fixed to $\alpha_\epsilon = 0.17$.

c	κ	a_0	a_1	b_0	b_1	c_α
$c_{\rm vir}$	0.059	0.611	9.754	14.848	−0.627	−0.245
$c_{\rm 200c}$	0.061	0.711	7.687	20.573	−1.041	0.237

are different. Differences could arise from based on profile fitting of all of the dark matter particles within $r_{\rm vir}$ to extrapolate the 200c parameters. We do not go into more detail in this analysis since these are beyond the scope of this chapter, though we wish to capture the concentration relations for our Einasto parameterization. Our complete implementation of Equation 4.7 using the density form of the Einasto profile is shown here.

The results of the best-fit parameters of Equation 4.7 are presented as the dashed curves in Figure 4.2 and are listed in Table 4.1. The best-fit parameters for the FIREbox halos are determined by fitting Equation 4.7 with the Einasto density structure to all of the median data points using a non-linear

least squares minimization. The analytical curves on the low-mass end matches well with the data to at least $\sim 5\%$, as indicated by the lower panels, though the behaviour from $M > 10^{11}\ h^{-1}M_{\odot}$ is questionable given the lack of more massive objects in our sample to calibrate the equation fit to properly accommodate the upturn.

Extending the results of Figure 4.2, the implied scatter is presented in Figure 4.3, were the solid lines is the simulated scatter based on median fit in Figure 4.2. The solid curves are well described by a log-normal distribution, and the best-fit distributions are presented as the dashed curves of corresponding color. Note that excess in the left tail is due to included dynamically "unrelaxed" halos in our sample, which would have comparably worse fits to begin with, but do not make up a significant portion of our halo sample in impact the underlying distribution. The curves here are limited to the mass bin of $10^{9-11}\ M_{\odot}$, as it will be comparable to the next section of best-fit projected concentrations of our sample.

It should be noted that our results are intended to be in the context of substructure lensing, where we wish to model low-mass dark matter halos below $\sim 10^{10}\ h^{-1}M_{\odot}$. We do not investigate further the behavior of concentrations higher than $\sim 10^{10}\ h^{-1}M_{\odot}$ and will move on to characterizing the projected concentration of the FIREbox halos.

4.4 The projected concentration-mass relation of low-mass halos

4.4.1 Mass convergence for two-dimensional projections

Although our high-resolution sample of halos contains halo masses to as low as $10^{8}\ M_{\odot}$, it is not obvious if we can trust the physical results for the best-fit values of R_{-1} at this low mass scale (see Chapter 3 for first disucssion). Figure 4.4 alleviates this issue by comparing the best-fit R_{-1} to the

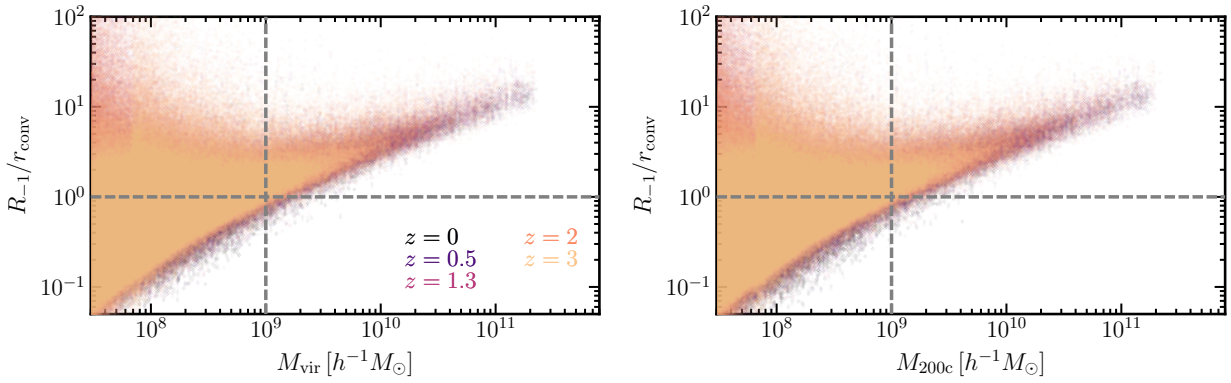

Figure 4.4: The mass resolution cutoff used for the entire analysis in two-projections. This is determine between the ratio between the convergence radius $r_{\rm conv}$ and the best-fit R_{-1} in the entire simulation box at all redshift ranges. The selected convergence mass is indicated by the intersecting dashed lines at $M \sim 10^9\ h^{-1}M_\odot$.

convergence radius, $r_{\rm conv}$, of each halo. At one-to-one on the y-axis (the horizontal dashed line), the mass resolution converges nicely at $\sim 2 \times 10^9\ h^{-1}M_\odot$, for both mass definitions at all of the redshifts considered here, but we push it down to $\sim 10^9\ h^{-1}M_\odot$ for a more quotable mass range.

4.4.2 Key results

The three-dimensional halo concentration was previously demonstrated to having unique relationship with the halo mass. We follow this tradition by plotting the projected concentration as a function of halo mass in Figure 4.5 using our two halo definitions from redshifts $z = 0 - 3$. The solid median lines depicts the trusted median within each mass bin, while the bands encapsulates 68% of the distribution found within each mass bin. The solid line cuts off at $10^9\ h^{-1}M_\odot$ and becomes a dashed line down to $10^8\ h^{-1}M_\odot$ to highlight the mass region at as which the best-fit R_{-1} becomes "unphysical", i.e., $R_{-1} < r_{\rm conv}$ (see Figure 4.4).

Like the the standard concentration-mass relation in CDM, the projected concentration also evolves strongly as a function of halo mass and has a anti-correlated relation. Additionally, the projected concentration evolves strongly with redshift. The $C_{\rm vir}$ relation evolves greatly with redshift given its stronger dependence on the cosmological parameters within the background density and over-

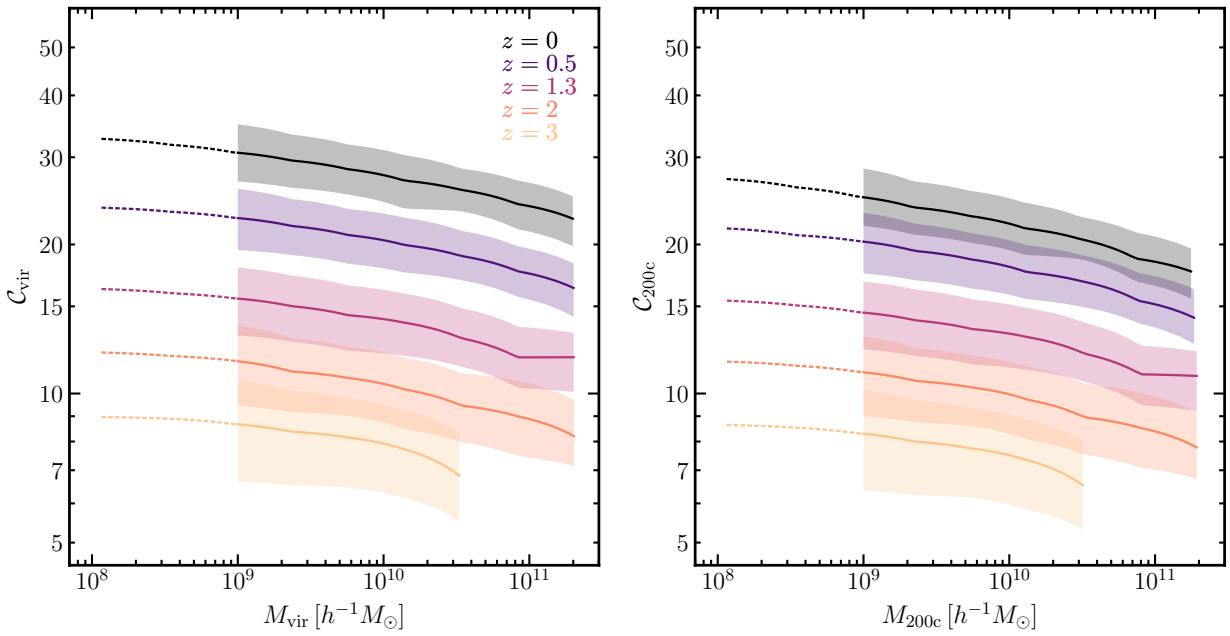

Figure 4.5: The evolution of the median projected concentration parameters, $C_\Delta := R_\Delta / R_{-1}$ as a function of the halo mass, based on our lens-mass model fit for both halo mass definitions. The solid lines depict the median while the bands encapsulate the 1σ distribution within each mass bin. The dashed portions depict the region at which the physical value of C_Δ becomes elusive. The projected concentration shows a strong dependence in halo mass as it evolves through time, though the effects of the redshift evolution is more suppressed for '200c' halo definition (bottom panel) compared to the virial definition (top panel).

density, while C_{200c} evolves more weakly in comparison with just a constant overdenisty. The forthcoming section provides analytical fits a more physically motivating model that would allow one to confidently extrapolate to lower halo masses beyond without the restriction of numerical resolution here.

Similar to the previous figure, Figure 4.6 shows the redshift evolution of the projected concentration as a function of peak height, ν (Equation 4.8), within this redshift range. The standard halo concentration tends to evolve weakly in comparison as a function of peak height based on previous work (e.g., Prada et al. 2012, Ludlow et al. 2014, Dutton and Macciò 2014, Child et al. 2018, Diemer and Kravtsov 2015). While not necessarily redshift independent, the projected concentration as a function of peak height in Figure 4.6 appears to evolve with redshift much more weakly compared as a function of halo mass, $M_{\rm vir}$. Additionally, like the case seen for the halo mass, M_{200c}, the "200c" halo definition evolves little to no evolution than the virial definition (compare the bottom panel to the top panel).

4.4.3 Modeling the redshift evolution

An important quantity to model within a statistical population of dark matter halos is to accurately describe the the evolution of the projected concentration as a function of LOS halo mass, especially in way that allows us to extrapolate to lower halo masses crucial to detect in substructure lensing studies ($M_{\rm halo} \sim 10^6\ M_\odot$). Indeed, since our mass range is limit to $M = 10^{9-11}\ M_\odot$ due to the particle resolution of cosmological box. It would be straightforward implement tool set to use is to model the projected concentration-mass relation as a power-law relation that evolves with redshift. However, these models tend to be valid within the range they are fitted in; their extrapolations to lower halo masses would give varying results in projected concentration.

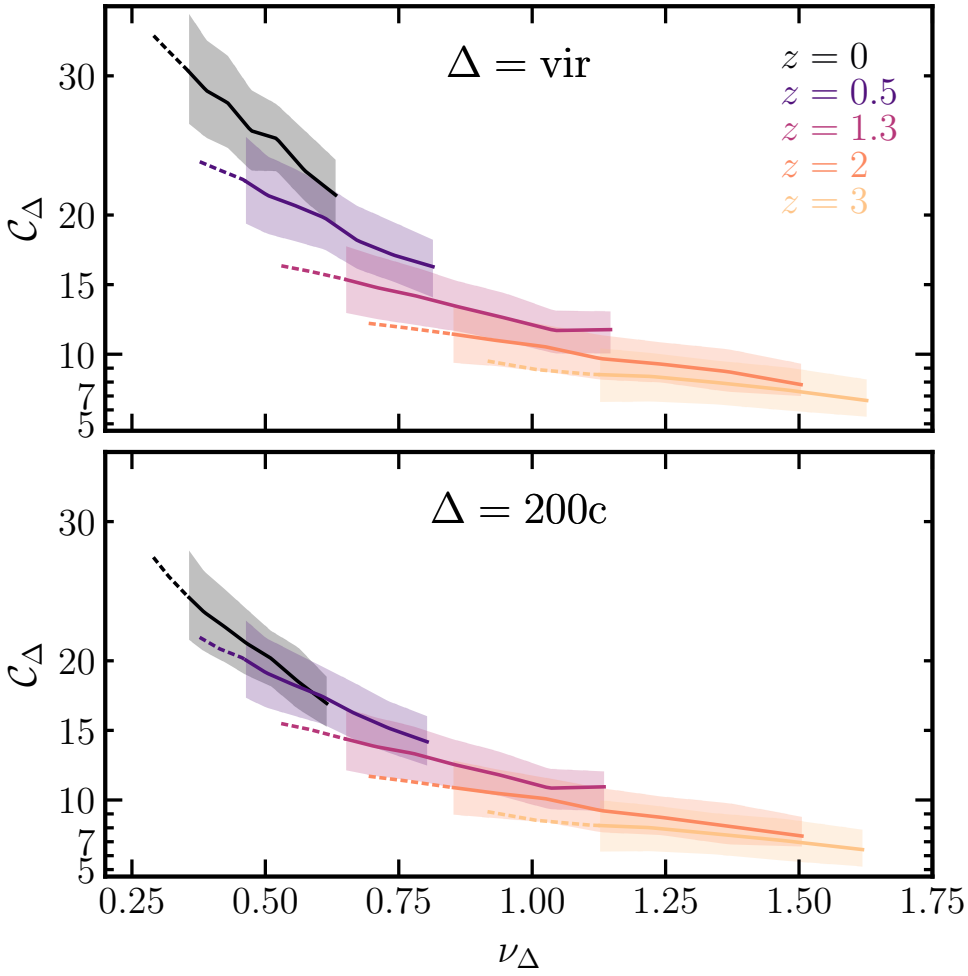

Figure 4.6: Similar in presentation to Figure 4.5, the evolution of the median projected concentration parameters, $C_\Delta := r_\Delta / R_{-1}$ as a function of the dimensionless peak height parameter, ν_Δ (Equation 4.8), based on our lens-mass model fit for both halo mass definitions. The peak height relation weakly evolves with redshift in contrast to the mass relation, though it is not entirely removed. Similarly to the halo mass relation, the projected concentration of the "200c" definition (bottom panel) is less impacted by redshift compared to the virial definition (top panel).

Physical motivation for of the projected structure?

The halo concentration equation from Section 4.3.1 is motivated by the form of the spherically averaged density. Could this formalism hold for surface densities? To resolve this conjecture, we repeat the derivation done by Diemer and Joyce (2019) for our lens-mass profile, Σ_β. To begin, the more generalized form of the spherical overdensity definition is

$$M_\Delta = \frac{4\pi}{3} r_\Delta^3 \, \rho_\Delta(z) \, . \tag{4.19}$$

Our surface-density model for Σ_β has an analogous form of the enclosed mass (see derivation in Section 3.4) and follows

$$\mathcal{M}(R) = 2\pi\Sigma_{-1} R_{-1}^2 \, \mathscr{g}(x) \, , \tag{4.20}$$

where Σ_{-1} is the scale surface density, $x := R/R_{-1}$, and

$$\mathscr{g}(x) = e^{\frac{1}{\beta}} \int_0^x \mathrm{d}x' x' \exp\left(-\frac{x'^\beta}{\beta}\right) \, . \tag{4.21}$$

From Chapter 3, we retrieve the projected effective mass, $\mathcal{M}_{\rm eff}$, when $R = r_\Delta$, since its likely $\mathcal{M}_{\rm eff} \neq M_\Delta$, as the depth of the projection plays a role. For our prescription with the cylinder depth set to $L_{\rm depth} = 3\, r_\Delta$, we do find that $\mathcal{M}_{\rm eff} \simeq M_\Delta$ for mass ranging by the decades. Combining the above equations at $R = r_\Delta$ gives us the following relation:

$$\frac{C_\Delta}{\left[\mathscr{g}\left(C_\Delta\right)\right]^{1/3}} = \left(\frac{3\Sigma_{-1}}{2\rho_\Delta(z) R_{-1}} (1+z)^3\right)^{1/3} \frac{1}{1+z} \, , \tag{4.22}$$

where $\rho_\Delta(z)$, R_{-1}, and Σ_{-1} have been converted to physical coordinates with factors of $(1+z)$.

Similar to the three-dimensional description, low-mass halos are expected to change as a result of "pseudo-evolution" since projected halos are defined by a background evolving radius. In other

words, we adopt the same definition of pseudo-evolution, where, similar to the halo profile in three dimensions, the scale projected radius and scale surface density, R_{-1} and Σ_{-1}, respectively, are assumed to be constant in physical coordinates and the halo evolves through the growth of the outer boundary, r_Δ. Assume now that at any redshift z, halos less than some enclosed mass, $M_{\rm pe}(z)$, are pseudo-evolving (denoted by subscript "pe"), such that each halo enters this phase at a redshift $z_{\rm pe} \geq z$. It follows that at $z_{\rm pe}$, we arrive at a similar form to the above:

$$\frac{C_{\rm pe}}{\left[g\left(C_{\rm pe}\right)\right]^{1/3}} = \left(\frac{3\Sigma_{-1}}{2\rho_\Delta(z_{\rm pe})R_{-1}}(1+z_{\rm pe})^3\right)^{1/3}\frac{1}{1+z_{\rm pe}}\,, \tag{4.23}$$

where we again converted all values on the right-hand side into physical coordinates. It follows that Σ_{-1} and R_{-1} are constant in physical coordinates, leaving us with the following relation:

$$\frac{C_\Delta}{\left[g\left(C_\Delta\right)\right]^{1/3}} = \left(\frac{\rho_\Delta(z_{\rm pe})}{\rho_\Delta(z)}\frac{(1+z)^3}{(1+z_{\rm pe})^3}\right)^{1/3}\frac{1+z_{\rm pe}}{1+z}\frac{C_{\rm pe}}{\left[g\left(C_{\rm pe}\right)\right]^{1/3}}\,, \tag{4.24}$$

where, as a consequence,

$$\frac{M_\Delta}{g\left(C_\Delta\right)} = \frac{M_{\rm pe}}{g\left(C_{\rm pe}\right)}\,. \tag{4.25}$$

Finally, if we define

$$\mathcal{G}(x) := \frac{x}{\left[g(x)\right]^{1/3}}\,, \tag{4.26}$$

and

$$X_{\rm ref}(z) := \left(\frac{\rho_\Delta(z_{\rm pe})}{\rho_\Delta(z)}\frac{(1+z)^3}{(1+z_{\rm pe})^3}\right)^{1/3}\,, \tag{4.27}$$

we write Equation 4.24 into the compacting form:s

$$C_{\Delta} = \widetilde{\mathscr{G}}\left[X_{\rm ref}(z)\frac{1+z_{\rm pe}}{1+z}\mathscr{G}(c_{\rm pe})\right] \tag{4.28}$$

where now $\widetilde{\mathscr{G}}$ is the inverse function of $\mathscr{G}$. We recover the exact form of Equation 10 in Diemer and Joyce (2019), where the only difference is how the underlying density structure, $\mathscr{g}$, is defined.

An accurate model for the projected structure of low-mass halos

Although the projected density profile, Σ_{β}, can be generalized without any assumption of the evolution of halos, we assume that by following the arguments made in Diemer and Joyce (2019), we should arrive at the analogues form for the projected concentration:

$$\frac{C_{\Delta}}{[\mathscr{g}(C_{\Delta})]^{(5+n)/6}} = \frac{A}{\nu(M_{\Delta},z)}P'\left[C,\frac{\nu(M_{\Delta},z)}{\nu_{\rm pe}}\right], \tag{4.29}$$

where the function $P'(C,y)$ describes the evolution of the surface-density and projected mass of the halo core from z to $z_{\rm pe}$ for a halo mass $M_{\rm pe}$. P' is also expected to approach unity for $y \ll 1$ and is expected to monotonically increase. For the three dimensional concentrations of dark matter halos, Diemer and Joyce (2019) used a quadratic peak height,

$$P' = \left[1+\frac{\nu^2}{B}\right], \tag{4.30}$$

which models the upturn seen for higher halo-masses seen from mass-concentration relations. This worked extremely well for our sample of Einasto based halos previoulsy in Section 4.3.1. For our analysis of low-mass halos, we find a peak height increasing linearly better models our population of low-mass dark matter halos without having to bother modeling the upturn at higher masses:

$$P' = \left[1+\frac{\nu}{B}\right]. \tag{4.31}$$

Table 4.2: Best-fitting parameters of the effective concentration-mass relation using our modified Diemer and Joyce (2019) model with our projected-mass profile (Equation 4.34 with shape fixed to $\beta = 0.3$).

C	κ	a_0	a_1	b_0	b_1	c_α
$C_{\rm vir}$	0.34	1.15	4.79	0.46	19.0	−0.12
$C_{\rm 200c}$	0.35	1.57	2.99	1.61	4.79	0.30

The concentration model we propose in the scale-free cosmology follows

$$\frac{C_\Delta}{[\mathcal{G}(C_\Delta)]^{(5+n)/6}} = \frac{A(n)}{\nu}\left[1 + \frac{\nu}{B(n)}\right], \tag{4.32}$$

where functions $A(n)$ and $B(n)$ are functions of n (slope of the intial power spectrum) and parameterized as $A = a_0 + a_1(n+3)$ and $B = b_0 + b_1(n+3)$. In a ΛCDM cosmology, we borrow the machinery used previously in Section 4.3.1 and the the above equation is rewritten in terms of the inverse function $\tilde{\mathcal{G}}$, the inverse of

$$\mathcal{G}(x) = \frac{x}{[\mathcal{G}(x)]^{(5+n_{\rm eff})/6}}\,, \tag{4.33}$$

and multiply it by the $\alpha_{\rm eff}$-dependent term, $C(\alpha_{\rm eff})$, to obtain the projected concentration model for low-mass halos:

$$C = C(\alpha_{\rm eff}) \times \widetilde{\mathcal{G}}\left(\frac{A(n_{\rm eff})}{\nu}\left[1 + \frac{\nu}{B(n_{\rm eff})}\right]\right), \tag{4.34}$$

where we also use the other fitting functions from Equation 4.19. Including the factor of the RMS fluctuations (κ), Equation 4.34 ultimatly has the same number of free parameters as the Diemer and Joyce (2019) model.

The results of this modified model are presented in Figure 4.7. The simulated data is presented are the solid dots and error bars, which are the median and 68% encapsulation of the concentration found within each mass bin. The best-fit parameters are determined by non-linear least-squares

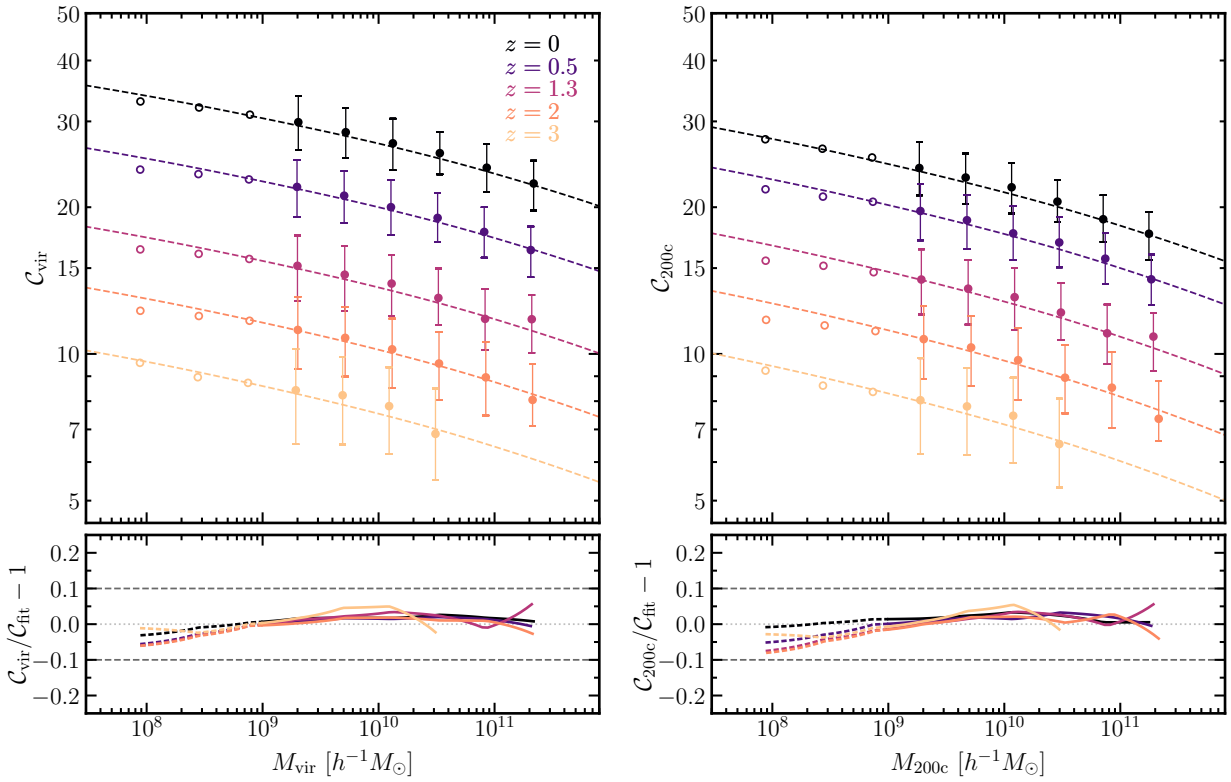

Figure 4.7: The projected concentration-mass relations for low-mass , line-of-sight dark matter halos within FIREbox from $z = 0 - 3$. *Top panel*: The solid points give the median projected concentration found within the binned values of mass for both mass definitions ("virial" and "200c" in left and right panels, respectively). The error bars encompass 68% of the concentrations as measured in the simulation. The open dots depict the bins of the mass resolution cutoff. The dashed curves model the median values using Equation 4.34 for each mass definition. *Bottom panel*: The quality of the fit. Each panel shows the relative difference between the simulated data and the model (using the parameters in Tables 4.2). The fitting functions mostly matches both definitions to 5% or better (indicated by dashed lines).

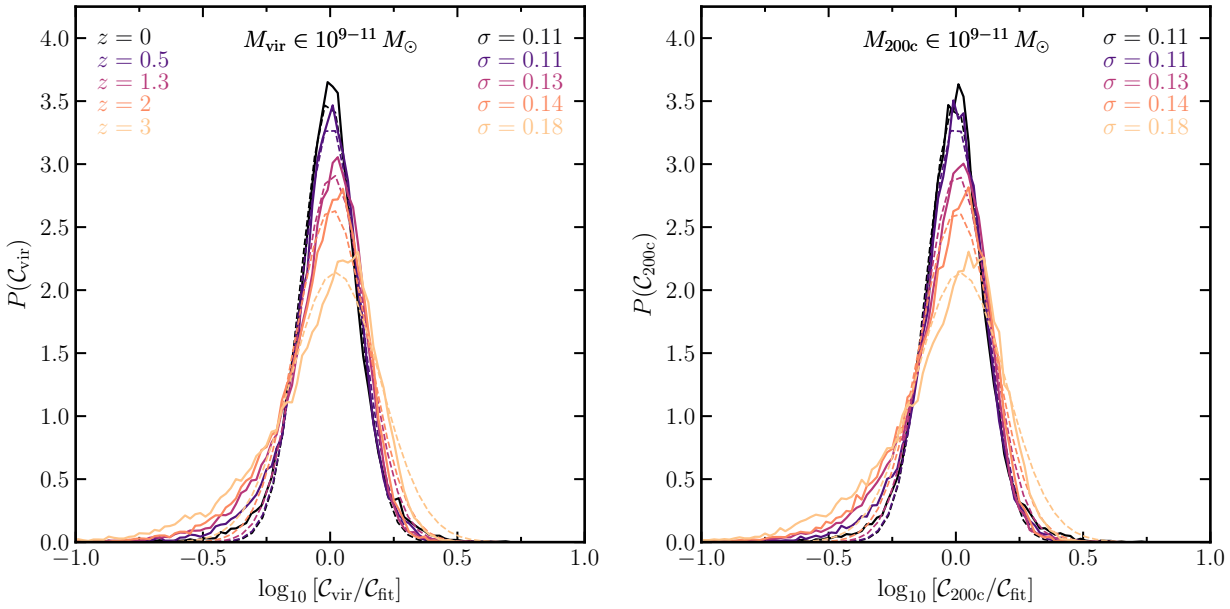

Figure 4.8: Scatter in the projected concentrations as a function of redshift for halos $M \in 10^{9-11}\,M_\odot$. The scatter (solid curves) at each redshift are well described by a log-normal distribution (dashed curves) with scatter of $\sim 0.12 - 14$ dex for both mass definitions.

minimization fit with the mass range $10^{9-11}\ h^{-1}M_\odot$ and are plotted as the dashed lines. The resulting best-fit parameters are listed in Table 4.2. The quality of the model to the simulation data are also shown in bottom panel of Figure 4.7, where both results for the definitions matches to $\sim 5\%$ or better for the solid lines. For even down to $10^8\ h^{-1}M_\odot$ (open circles), for which the fit was applied to, the extrapolate values are in fairly good agreement. The accuracy of the model, while also being physically motivating, should leave one confident with extrapolating to lower halo masses. The behavior of our concentration model above $M \simeq 10^{11}\ M_\odot$ is one of uncertainty given that upturn in concentration at higher redshifts. It should be made clear that the intended behavior of masses higher than what is explored here is questionable, but the intention of this work is to models halo masses $\lesssim 10^{10}\ M_\odot$.

4.4.4 Scatter in structural parameters

The spread in values for the projected concentration at fixed mass could be of significance for observations and models in substructure lensing. The distributions of $C(M)$ at each redshift for halo masses $M \in 10^{9-11}\ M_{\odot}$ are shown in Figure 4.8 for the two mass definitions. The distributions in the projected concentrations of the LOS halos are well described using a log-normal distribution:

$$P(C) = \frac{(C\ \log 10)^{-1}}{\sqrt{2\pi}\ \sigma_{\log_{10} C}} \exp\left[-\frac{\left(\log_{10} C - \log_{10} C_0\right)^2}{2\sigma^2_{\log_{10} C}}\right], \tag{4.35}$$

where $\sigma_{\log_{10} C}$ is the scatter and and $\log_{10} C_0$. The scatter in the distributions for redshifts $z = 0$ to 3 are well described using $\sigma_{\log_{10} C} \sim 0.12$. Each distribution shows a slight excess of lower projected concentration halos compared to the log-normal shape. This is due to the unrelaxed halos within out sample, which also in the case of halo concentrations (e.g. Klypin et al. 2016, Child et al. 2018), have much lower projected concentrations on average.

4.5 Summary and concluding remarks

This chapter studies the evolution and scatter of the surface density structure of LOS dark matter halos using FIREbox, a dark matter only cosmological simulation that for halos of mass $M_{\rm vir} = 10^{8-11}\ h^{-1} M_{\odot}$ within a ΛCDM. We begin by assessing the halo concentration-mass relation within FIREbox for Einasto density structures. The median relation is well described by the Diemer and Joyce (2019) model to within 5% accuracy (Figure 4.2). The scatter of these concentrations, based of the median best-fit parameters of the Diemer and Joyce (2019) model is also well described as a log-normal distribution (Figure 4.3).

Similar to the mass-concentration relation of cold dark matter halos, the median projected concentration, determined from best-fit values of R_{-1} of each halo, as a function of halo mass is shaped as

a simple power-law relation that evolves to lower projected concentrations, i.e., dark matter halos become less dense as redshift increases (Figure 4.5). Moreover, when parameterizing projected concentrations as peak height, ν, instead of mass (Figure 4.6), the projected concentrations are more robustly parameterize as a function of redshift.

We use the physical arguments of the Diemer and Joyce (2019) model to accurately calibrate the median relation of the projected concentration as a function of halo mass, redshift, and cosmology to within 5 % accuracy (Figure 4.7). In addition, the scatter is quantified and is robustly describe to have a log-normal distribution (Figure 4.8). Knowing the analytical functions will aid in future substructure lensing studies. The next appropriate steps of this chapter would be to utilize our analytical machinery in a more in-depth statistical lensing analysis in order to more stringently bound the differences seen from modeling the projected structure of dark matter halos.

Chapter Acknowledgements

Part of this research was carried out at the Jet Propulsion Laboratory, California Institute of Technology, under a contract with the National Aeronautics and Space Administration. The authors thank the FIRE collaboration for the use of the DMO FIREbox simulations for our analysis. Support came from the National Science Foundation (NSF) grant AST-1910965 and from the NASA grant 80NSSSC20K1469.

Bibliography

Allgood, B., Flores, R. A., Primack, J. R., Kravtsov, A. V., Wechsler, R. H., Faltenbacher, A., and Bullock, J. S. (2006). The shape of dark matter haloes: dependence on mass, redshift, radius and formation. *MNRAS*, 367(4):1781–1796.

Amorisco, N. C., Nightingale, J., He, Q., Amvrosiadis, A., Cao, X., Cole, S., Etherington, A., Frenk, C. S., Li, R., Massey, R., and Robertson, A. (2022). Halo concentration strengthens dark matter constraints in galaxy-galaxy strong lensing analyses. *MNRAS*, 510(2):2464–2479.

Angulo, R. E. and Hahn, O. (2022). Large-scale dark matter simulations. *Living Reviews in Computational Astrophysics*, 8(1):1.

Angulo, R. E. and White, S. D. M. (2010). One simulation to fit them all - changing the background parameters of a cosmological N-body simulation. *MNRAS*, 405(1):143–154.

Avila-Reese, V., Firmani, C., Klypin, A., and Kravtsov, A. V. (1999). Density profiles of dark matter haloes: diversity and dependence on environment. *MNRAS*, 310(2):527–539.

Bailin, J. and Steinmetz, M. (2005). Internal and External Alignment of the Shapes and Angular Momenta of ΛCDM Halos. *Apj*, 627(2):647–665.

Banik, N., Bovy, J., Bertone, G., Erkal, D., and de Boer, T. J. L. (2019). Novel constraints on the particle nature of dark matter from stellar streams. *arXiv e-prints*, page arXiv:1911.02663.

Behroozi, P. S., Wechsler, R. H., and Wu, H.-Y. (2013). The ROCKSTAR Phase-space Temporal Halo Finder and the Velocity Offsets of Cluster Cores. *Apj*, 762(2):109.

Benitez-Llambay, A. and Frenk, C. (2020). The detailed structure and the onset of galaxy formation in low-mass gaseous dark matter haloes. *MNRAS*, 498(4):4887–4900.

Bertone, G. and Tait, T. M. P. (2018). A new era in the search for dark matter. *Nature*, 562(7725):51–56.

Bett, P., Eke, V., Frenk, C. S., Jenkins, A., Helly, J., and Navarro, J. (2007). The spin and shape of dark matter haloes in the Millennium simulation of a Λ cold dark matter universe. *MNRAS*, 376(1):215–232.

Bhattacharya, S., Habib, S., Heitmann, K., and Vikhlinin, A. (2013). Dark Matter Halo Profiles of Massive Clusters: Theory versus Observations. *Apj*, 766(1):32.

Binney, J. and Tremaine, S. (2008). *Galactic Dynamics: Second Edition*.

Birrer, S. and Amara, A. (2018). lenstronomy: Multi-purpose gravitational lens modelling software package. *Physics of the Dark Universe*, 22:189–201.

Birrer, S., Shajib, A., Gilman, D., Galan, A., Aalbers, J., Millon, M., Morgan, R., Pagano, G., Park, J., Teodori, L., Tessore, N., Ueland, M., Van de Vyvere, L., Wagner-Carena, S., Wempe, E., Yang, L., Ding, X., Schmidt, T., Sluse, D., Zhang, M., and Amara, A. (2021). lenstronomy II: A gravitational lensing software ecosystem. *The Journal of Open Source Software*, 6(62):3283.

Blandford, R. and Narayan, R. (1986). Fermat's Principle, Caustics, and the Classification of Gravitational Lens Images. *Apj*, 310:568.

Blumenthal, G. R., Faber, S. M., Primack, J. R., and Rees, M. J. (1984). Formation of galaxies and large-scale structure with cold dark matter. *Nature*, 311:517–525.

Bode, P., Ostriker, J. P., and Turok, N. (2001). Halo Formation in Warm Dark Matter Models. *Apj*, 556(1):93–107.

Bolton, A. S., Burles, S., Koopmans, L. V. E., Treu, T., Gavazzi, R., Moustakas, L. A., Wayth, R., and Schlegel, D. J. (2008). The Sloan Lens ACS Survey. V. The Full ACS Strong-Lens Sample. *Apj*, 682(2):964–984.

Bond, J. R., Kofman, L., and Pogosyan, D. (1996). How filaments of galaxies are woven into the cosmic web. *Nature*, 380(6575):603–606.

Boyarsky, A., Ruchayskiy, O., Iakubovskyi, D., and Franse, J. (2014). Unidentified Line in X-Ray Spectra of the Andromeda Galaxy and Perseus Galaxy Cluster. *PRL*, 113(25):251301.

Bozek, B., Boylan-Kolchin, M., Horiuchi, S., Garrison-Kimmel, S., Abazajian, K., and Bullock, J. S. (2016). Resonant sterile neutrino dark matter in the local and high-z Universe. *MNRAS*, 459(2):1489–1504.

Bradač, M., Schneider, P., Steinmetz, M., Lombardi, M., King, L. J., and Porcas, R. (2002). B1422+231: The influence of mass substructure on strong lensing. *AAP*, 388:373–382.

Brooks, A. M. and Zolotov, A. (2014). Why Baryons Matter: The Kinematics of Dwarf Spheroidal Satellites. *Apj*, 786(2):87.

Brown, S. T., McCarthy, I. G., Stafford, S. G., and Font, A. S. (2022). Towards a universal model for the density profiles of dark matter haloes. *MNRAS*, 509(4):5685–5701.

Bryan, G. L. and Norman, M. L. (1998). Statistical Properties of X-Ray Clusters: Analytic and Numerical Comparisons. *Apj*, 495(1):80–99.

Bulbul, E., Markevitch, M., Foster, A., Smith, R. K., Loewenstein, M., and Randall, S. W. (2014). Detection of an Unidentified Emission Line in the Stacked X-Ray Spectrum of Galaxy Clusters. *APJ*, 789(1):13.

Bullock, J. S. and Boylan-Kolchin, M. (2017). Small-Scale Challenges to the ΛCDM Paradigm. *ARAA*, 55(1):343–387.

Bullock, J. S., Kolatt, T. S., Sigad, Y., Somerville, R. S., Kravtsov, A. V., Klypin, A. A., Primack, J. R., and Dekel, A. (2001). Profiles of dark haloes: evolution, scatter and environment. *MNRAS*, 321(3):559–575.

Bullock, J. S., Kravtsov, A. V., and Weinberg, D. H. (2000). Reionization and the Abundance of Galactic Satellites. *Apj*, 539(2):517–521.

Cardone, V. F. (2004). The lensing properties of the Sersic model. *AAP*, 415:839–848.

Carlberg, R. G. (2009). Star Stream Folding by Dark Galactic Subhalos. *Apjl*, 705(2):L223–L226.

Child, H. L., Habib, S., Heitmann, K., Frontiere, N., Finkel, H., Pope, A., and Morozov, V. (2018). Halo Profiles and the Concentration-Mass Relation for a ΛCDM Universe. *Apj*, 859(1):55.

Cole, S. and Lacey, C. (1996). The structure of dark matter haloes in hierarchical clustering models. *MNRAS*, 281:716.

Colín, P., Avila-Reese, V., and Valenzuela, O. (2000). Substructure and Halo Density Profiles in a Warm Dark Matter Cosmology. *Apj*, 542(2):622–630.

Collett, T. E. (2015). The Population of Galaxy-Galaxy Strong Lenses in Forthcoming Optical Imaging Surveys. *Apj*, 811(1):20.

Contreras, S., Angulo, R. E., Zennaro, M., Aricò, G., and Pellejero-Ibañez, M. (2020). 3 per cent-accurate predictions for the clustering of dark matter, haloes, and subhaloes, over a wide range of cosmologies and scales. *MNRAS*, 499(4):4905–4917.

Correa, C. A., Wyithe, J. S. B., Schaye, J., and Duffy, A. R. (2015). The accretion history of dark matter haloes - III. A physical model for the concentration-mass relation. *MNRAS*, 452(2):1217–1232.

Dalal, N. and Kochanek, C. S. (2002). Direct Detection of Cold Dark Matter Substructure. *Apj*, 572(1):25–33.

Dalal, N., Lithwick, Y., and Kuhlen, M. (2010). The Origin of Dark Matter Halo Profiles. *arXiv e-prints*, page arXiv:1010.2539.

D'Aloisio, A., Natarajan, P., and Shapiro, P. R. (2014). The effect of large-scale structure on the magnification of high-redshift sources by cluster lenses. *MNRAS*, 445(4):3581–3591.

Davis, M., Efstathiou, G., Frenk, C. S., and White, S. D. M. (1985). The evolution of large-scale structure in a universe dominated by cold dark matter. *Apj*, 292:371–394.

Despali, G., Giocoli, C., and Tormen, G. (2014). Some like it triaxial: the universality of dark matter halo shapes and their evolution along the cosmic time. *MNRAS*, 443(4):3208–3217.

Despali, G. and Vegetti, S. (2017). The impact of baryonic physics on the subhalo mass function and implications for gravitational lensing. *MNRAS*, 469(2):1997–2010.

Despali, G., Vegetti, S., White, S. D. M., Giocoli, C., and van den Bosch, F. C. (2018). Modelling the line-of-sight contribution in substructure lensing. *MNRAS*, 475(4):5424–5442.

Dhar, B. K. (2021). High-accuracy analytical solutions for the projected mass (counts) and surface density (brightness) of Einasto profiles. *MNRAS*, 504(3):4583–4588.

Dhar, B. K. and Williams, L. L. R. (2010). Surface mass density of the Einasto family of dark matter haloes: are they Sersic-like? *MNRAS*, 405(1):340–346.

Diemand, J., Kuhlen, M., and Madau, P. (2007). Formation and Evolution of Galaxy Dark Matter Halos and Their Substructure. *Apj*, 667(2):859–877.

Diemer, B. (2018). COLOSSUS: A Python Toolkit for Cosmology, Large-scale Structure, and Dark Matter Halos. *Apjs*, 239(2):35.

Diemer, B. and Joyce, M. (2019). An Accurate Physical Model for Halo Concentrations. *Apj*, 871(2):168.

Diemer, B. and Kravtsov, A. V. (2014). Dependence of the Outer Density Profiles of Halos on Their Mass Accretion Rate. *Apj*, 789(1):1.

Diemer, B. and Kravtsov, A. V. (2015). A Universal Model for Halo Concentrations. *Apj*, 799(1):108.

Dietrich, J. P., Zhang, Y., Song, J., Davis, C. P., McKay, T. A., Baruah, L., Becker, M., Benoist, C., Busha, M., da Costa, L. A. N., Hao, J., Maia, M. A. G., Miller, C. J., Ogando, R., Romer, A. K., Rozo, E., Rykoff, E., and Wechsler, R. (2014). Orientation bias of optically selected galaxy clusters and its impact on stacked weak-lensing analyses. *MNRAS*, 443(2):1713–1722.

Dolag, K., Bartelmann, M., Perrotta, F., Baccigalupi, C., Moscardini, L., Meneghetti, M., and Tormen, G. (2004). Numerical study of halo concentrations in dark-energy cosmologies. *AAPL*, 416:853–864.

Dolag, K., Komatsu, E., and Sunyaev, R. (2016). SZ effects in the Magneticum Pathfinder simulation: comparison with the Planck, SPT, and ACT results. *MNRAS*, 463(2):1797–1811.

Dubinski, J. and Carlberg, R. G. (1991). The Structure of Cold Dark Matter Halos. *Apj*, 378:496.

Dubois, Y., Peirani, S., Pichon, C., Devriendt, J., Gavazzi, R., Welker, C., and Volonteri, M. (2016). The HORIZON-AGN simulation: morphological diversity of galaxies promoted by AGN feedback. *MNRAS*, 463(4):3948–3964.

Duffy, A. R., Schaye, J., Kay, S. T., and Dalla Vecchia, C. (2008). Dark matter halo concentrations in the Wilkinson Microwave Anisotropy Probe year 5 cosmology. *MNRAS*, 390(1):L64–L68.

Dutton, A. A. and Macciò, A. V. (2014). Cold dark matter haloes in the Planck era: evolution of structural parameters for Einasto and NFW profiles. *MNRAS*, 441(4):3359–3374.

Efstathiou, G. (1992). Suppressing the formation of dwarf galaxies via photoionization. *MNRAS*, 256(2):43P–47P.

Eigenbrod, A., Courbin, F., Meylan, G., Vuissoz, C., and Magain, P. (2006). COSMOGRAIL: the COSmological MOnitoring of GRAvItational Lenses. III. Redshift of the lensing galaxy in eight gravitationally lensed quasars. *AAP*, 451(3):759–766.

Einasto, J. (1965). On the Construction of a Composite Model for the Galaxy and on the Determination of the System of Galactic Parameters. *Trudy Astrofizicheskogo Instituta Alma-Ata*, 5:87–100.

Eisenstein, D. J. and Hu, W. (1998). Baryonic Features in the Matter Transfer Function. *Apj*, 496(2):605–614.

Eke, V. R., Navarro, J. F., and Steinmetz, M. (2001). The Power Spectrum Dependence of Dark Matter Halo Concentrations. *Apj*, 554(1):114–125.

Elbert, O. D., Bullock, J. S., Garrison-Kimmel, S., Rocha, M., Oñorbe, J., and Peter, A. H. G. (2015). Core formation in dwarf haloes with self-interacting dark matter: no fine-tuning necessary. *MNRAS*, 453(1):29–37.

Fedeli, C., Bartelmann, M., Meneghetti, M., and Moscardini, L. (2007). Effects of the halo concentration distribution on strong-lensing optical depth and X-ray emission. *AAP*, 473(3):715–725.

Feldmann, R., Quataert, E., Faucher-Giguère, C.-A., Hopkins, P. F., Çatmabacak, O., Kereš, D., Bassini, L., Bernardini, M., Bullock, J. S., Cenci, E., Gensior, J., Liang, L., Moreno, J., and Wetzel, A. (2022). FIREbox: Simulating galaxies at high dynamic range in a cosmological volume. *arXiv e-prints*, page arXiv:2205.15325.

Feldmann, R. and Spolyar, D. (2015). Detecting dark matter substructures around the Milky Way with Gaia. *MNRAS*, 446(1):1000–1012.

Feng, J. L., Kaplinghat, M., Tu, H., and Yu, H.-B. (2009). Hidden charged dark matter. *JCAP*, 2009(7):004.

Feroz, F. and Hobson, M. P. (2012). Weak lensing by triaxial galaxy clusters. *MNRAS*, 420(1):596–603.

Fitts, A., Boylan-Kolchin, M., Elbert, O. D., Bullock, J. S., Hopkins, P. F., Oñorbe, J., Wetzel, A., Wheeler, C., Faucher-Giguère, C.-A., Kereš, D., Skillman, E. D., and Weisz, D. R. (2017). fire in the field: simulating the threshold of galaxy formation. *MNRAS*, 471(3):3547–3562.

Frenk, C. S. and White, S. D. M. (2012). Dark matter and cosmic structure. *Annalen der Physik*, 524(9-10):507–534.

Frenk, C. S., White, S. D. M., Davis, M., and Efstathiou, G. (1988). The Formation of Dark Halos in a Universe Dominated by Cold Dark Matter. *Apj*, 327:507.

Gao, L., Navarro, J. F., Cole, S., Frenk, C. S., White, S. D. M., Springel, V., Jenkins, A., and Neto, A. F. (2008). The redshift dependence of the structure of massive Λ cold dark matter haloes. *MNRAS*, 387(2):536–544.

Garrison-Kimmel, S., Boylan-Kolchin, M., Bullock, J. S., and Lee, K. (2014). ELVIS: Exploring the Local Volume in Simulations. *MNRAS*, 438(3):2578–2596.

Garrison-Kimmel, S., Wetzel, A., Bullock, J. S., Hopkins, P. F., Boylan-Kolchin, M., Faucher-Giguère, C.-A., Kereš, D., Quataert, E., Sanderson, R. E., Graus, A. S., and Kelley, T. (2017). Not so lumpy after all: modelling the depletion of dark matter subhaloes by Milky Way-like galaxies. *MNRAS*, 471(2):1709–1727.

Geller, M. J. and Huchra, J. P. (1989). Mapping the Universe. *Science*, 246(4932):897–903.

Genel, S., Vogelsberger, M., Springel, V., Sijacki, D., Nelson, D., Snyder, G., Rodriguez-Gomez, V., Torrey, P., and Hernquist, L. (2014). Introducing the Illustris project: the evolution of galaxy populations across cosmic time. *MNRAS*, 445(1):175–200.

Gill, S. P. D., Knebe, A., and Gibson, B. K. (2004). The evolution of substructure - I. A new identification method. *MNRAS*, 351(2):399–409.

Gill, S. P. D., Knebe, A., and Gibson, B. K. (2005). The evolution of substructure - III. The outskirts of clusters. *MNRAS*, 356(4):1327–1332.

Gilman, D., Agnello, A., Treu, T., Keeton, C. R., and Nierenberg, A. M. (2017). Strong lensing signatures of luminous structure and substructure in early-type galaxies. *MNRAS*, 467(4):3970–3992.

Gilman, D., Benson, A., Bovy, J., Birrer, S., Treu, T., and Nierenberg, A. (2022). The primordial matter power spectrum on sub-galactic scales. *MNRAS*, 512(3):3163–3188.

Gilman, D., Birrer, S., Nierenberg, A., Treu, T., Du, X., and Benson, A. (2020a). Warm dark matter chills out: constraints on the halo mass function and the free-streaming length of dark matter with eight quadruple-image strong gravitational lenses. *MNRAS*, 491(4):6077–6101.

Gilman, D., Birrer, S., Treu, T., Keeton, C. R., and Nierenberg, A. (2018). Probing the nature of dark matter by forward modelling flux ratios in strong gravitational lenses. *MNRAS*, 481(1):819–834.

Gilman, D., Birrer, S., Treu, T., Nierenberg, A., and Benson, A. (2019). Probing dark matter structure down to 10^7 solar masses: flux ratio statistics in gravitational lenses with line-of-sight haloes. *MNRAS*, 487(4):5721–5738.

Gilman, D., Bovy, J., Treu, T., Nierenberg, A., Birrer, S., Benson, A., and Sameie, O. (2021). Strong lensing signatures of self-interacting dark matter in low-mass haloes. *MNRAS*, 507(2):2432–2447.

Gilman, D., Du, X., Benson, A., Birrer, S., Nierenberg, A., and Treu, T. (2020b). Constraints on the mass-concentration relation of cold dark matter halos with 11 strong gravitational lenses. *MNRAS*, 492(1):L12–L16.

Gradshteyn, I. S. and Ryzhik, I. M. (1980). *Table of integrals, series and products*.

Graus, A. S., Bullock, J. S., Boylan-Kolchin, M., and Nierenberg, A. M. (2018). Through a Smoother Lens: An expected absence of LCDM substructure detections from hydrodynamic and dark matter only simulations. *Monthly Notices of the Royal Astronomical Society*, 480(1):1322–1332.

Green, A. M., Hofmann, S., and Schwarz, D. J. (2004). The power spectrum of SUSY-CDM on subgalactic scales. *MNRAS*, 353(3):L23–L27.

Green, A. M., Hofmann, S., and Schwarz, D. J. (2005). The first WIMPy halos. *JCAP*, 2005(8):003.

Groener, A. M. and Goldberg, D. M. (2014). Shape Profiles and Orientation Bias for Weak and Strong Lensing Cluster Halos. *Apj*, 795(2):153.

Hahn, O. and Abel, T. (2011). Multi-scale initial conditions for cosmological simulations. *MNRAS*, 415(3):2101–2121.

He, Q., Li, R., Frenk, C. S., Nightingale, J., Cole, S., Amorisco, N. C., Massey, R., Robertson, A., Etherington, A., Amvrosiadis, A., and Cao, X. (2022). Galaxy-galaxy strong lens perturbations: line-of-sight haloes versus lens subhaloes. *MNRAS*, 512(4):5862–5873.

He, Q., Li, R., Lim, S., Frenk, C. S., Cole, S., Peng, E. W., and Wang, Q. (2018). Globular clusters versus dark matter haloes in strong lensing observations. *MNRAS*, 480(4):5084–5091.

He, Q., Robertson, A., Nightingale, J., Cole, S., Frenk, C. S., Massey, R., Amvrosiadis, A., Li, R., Cao, X., and Etherington, A. (2020). A forward-modelling method to infer the dark matter particle mass from strong gravitational lenses. *arXiv e-prints*, page arXiv:2010.13221.

Heath, D. J. (1977). The growth of density perturbations in zero pressure Friedmann-Lemaître universes. *MNRAS*, 179:351–358.

Hezaveh, Y. D., Dalal, N., Marrone, D. P., Mao, Y.-Y., Morningstar, W., Wen, D., Bland ford, R. D., Carlstrom, J. E., Fassnacht, C. D., Holder, G. P., Kemball, A., Marshall, P. J., Murray, N., Perreault Levasseur, L., Vieira, J. D., and Wechsler, R. H. (2016). Detection of Lensing Substructure Using ALMA Observations of the Dusty Galaxy SDP.81. *Apj*, 823(1):37.

Hopkins, P. F. (2015). A new class of accurate, mesh-free hydrodynamic simulation methods. *MNRAS*, 450(1):53–110.

Hopkins, P. F., Wetzel, A., Kereš, D., Faucher-Giguère, C.-A., Quataert, E., Boylan-Kolchin, M., Murray, N., Hayward, C. C., Garrison-Kimmel, S., Hummels, C., Feldmann, R., Torrey, P., Ma, X., Anglés-Alcázar, D., Su, K.-Y., Orr, M., Schmitz, D., Escala, I., Sanderson, R., Grudić, M. Y., Hafen, Z., Kim, J.-H., Fitts, A., Bullock, J. S., Wheeler, C., Chan, T. K., Elbert, O. D., and Narayanan, D. (2018). FIRE-2 simulations: physics versus numerics in galaxy formation. *MNRAS*, 480(1):800–863.

Horiuchi, S., Bozek, B., Abazajian, K. N., Boylan-Kolchin, M., Bullock, J. S., Garrison-Kimmel, S., and Onorbe, J. (2016). Properties of resonantly produced sterile neutrino dark matter subhaloes. *MNRAS*, 456(4):4346–4353.

Hsueh, J.-W., Despali, G., Vegetti, S., Xu, D. a., Fassnacht, C. D., and Metcalf, R. B. (2018). Flux-ratio anomalies from discs and other baryonic structures in the Illustris simulation. *MNRAS*, 475(2):2438–2451.

Hsueh, J. W., Enzi, W., Vegetti, S., Auger, M. W., Fassnacht, C. D., Despali, G., Koopmans, L. V. E., and McKean, J. P. (2020). SHARP - VII. New constraints on the dark matter free-streaming properties and substructure abundance from gravitationally lensed quasars. *MNRAS*, 492(2):3047–3059.

Hsueh, J. W., Oldham, L., Spingola, C., Vegetti, S., Fassnacht, C. D., Auger, M. W., Koopmans, L. V. E., McKean, J. P., and Lagattuta, D. J. (2017). SHARP - IV. An apparent flux-ratio anomaly resolved by the edge-on disc in B0712+472. *MNRAS*, 469(3):3713–3721.

Huss, A., Jain, B., and Steinmetz, M. (1999). How Universal Are the Density Profiles of Dark Halos? *Apj*, 517(1):64–69.

Ibata, R. A., Lewis, G. F., Irwin, M. J., and Quinn, T. (2002). Uncovering cold dark matter halo substructure with tidal streams. *MNRAS*, 332(4):915–920.

Inoue, K. T. (2016). On the origin of the flux ratio anomaly in quadruple lens systems. *MNRAS*, 461(1):164–175.

Inoue, K. T. and Takahashi, R. (2012). Weak lensing by line-of-sight haloes as the origin of flux-ratio anomalies in quadruply lensed QSOs. *MNRAS*, 426(4):2978–2993.

Inoue, K. T., Takahashi, R., Takahashi, T., and Ishiyama, T. (2015). Constraints on warm dark matter from weak lensing in anomalous quadruple lenses. *MNRAS*, 448(3):2704–2716.

Ishiyama, T., Prada, F., Klypin, A. A., Sinha, M., Metcalf, R. B., Jullo, E., Altieri, B., Cora, S. A., Croton, D., de la Torre, S., Millán-Calero, D. E., Oogi, T., Ruedas, J., and Vega-Martínez, C. A. (2021). The Uchuu simulations: Data Release 1 and dark matter halo concentrations. *MNRAS*, 506(3):4210–4231.

Jing, Y. P. and Suto, Y. (2002). Triaxial Modeling of Halo Density Profiles with High-Resolution N-Body Simulations. *Apj*, 574(2):538–553.

Kasun, S. F. and Evrard, A. E. (2005). Shapes and Alignments of Galaxy Cluster Halos. *Apj*, 629(2):781–790.

Kelley, T., Bullock, J. S., Garrison-Kimmel, S., Boylan-Kolchin, M., Pawlowski, M. S., and Graus, A. S. (2019). Phat ELVIS: The inevitable effect of the Milky Way's disc on its dark matter subhaloes. *MNRAS*, 487(3):4409–4423.

Khandai, N., Di Matteo, T., Croft, R., Wilkins, S., Feng, Y., Tucker, E., DeGraf, C., and Liu, M.-S. (2015). The MassiveBlack-II simulation: the evolution of haloes and galaxies to z $\sim$ 0. *MNRAS*, 450(2):1349–1374.

Klypin, A., Yepes, G., Gottlöber, S., Prada, F., and Heß, S. (2016). MultiDark simulations: the story of dark matter halo concentrations and density profiles. *MNRAS*, 457(4):4340–4359.

Klypin, A. A., Trujillo-Gomez, S., and Primack, J. (2011). Dark Matter Halos in the Standard Cosmological Model: Results from the Bolshoi Simulation. *Apj*, 740(2):102.

Knollmann, S. R. and Knebe, A. (2009). AHF: Amiga's Halo Finder. *ApjS*, 182(2):608–624.

Knollmann, S. R., Power, C., and Knebe, A. (2008). Dark matter halo profiles in scale-free cosmologies. *MNRAS*, 385(2):545–552.

Koopmans, L. V. E. (2005). Gravitational imaging of cold dark matter substructures. *MNRAS*, 363(4):1136–1144.

Lau, E. T., Hearin, A. P., Nagai, D., and Cappelluti, N. (2020). Correlations between Triaxial Shapes and Formation History of Dark Matter haloes. *MNRAS*.

Lazar, A., Bullock, J. S., Boylan-Kolchin, M., Chan, T. K., Hopkins, P. F., Graus, A. S., Wetzel, A., El-Badry, K., Wheeler, C., Straight, M. C., Kereš, D., Faucher-Giguère, C.-A., Fitts, A., and Garrison-Kimmel, S. (2020). A dark matter profile to model diverse feedback-induced core sizes of ΛCDM haloes. *MNRAS*, 497(2):2393–2417.

Lazar, A., Bullock, J. S., Boylan-Kolchin, M., Feldmann, R., Çatmabacak, O., and Moustakas, L. (2021). Out of sight, out of mind? The impact of correlated clustering in substructure lensing. *MNRAS*, 502(4):6064–6079.

Li, R., Frenk, C. S., Cole, S., Gao, L., Bose, S., and Hellwing, W. A. (2016). Constraints on the identity of the dark matter from strong gravitational lenses. *MNRAS*, 460(1):363–372.

Li, R., Frenk, C. S., Cole, S., Wang, Q., and Gao, L. (2017). Projection effects in the strong lensing study of subhaloes. *MNRAS*, 468(2):1426–1432.

López-Cano, D., Angulo, R. E., Ludlow, A. D., Zennaro, M., Contreras, S., Chaves-Montero, J., and Aricò, G. (2022). The cosmology dependence of the concentration-mass-redshift relation. *MNRAS*, 517(2):2000–2011.

Lovell, M. R., Eke, V., Frenk, C. S., Gao, L., Jenkins, A., Theuns, T., Wang, J., White, S. D. M., Boyarsky, A., and Ruchayskiy, O. (2012). The haloes of bright satellite galaxies in a warm dark matter universe. *MNRAS*, 420(3):2318–2324.

Lovell, M. R., Frenk, C. S., Eke, V. R., Jenkins, A., Gao, L., and Theuns, T. (2014). The properties of warm dark matter haloes. *MNRAS*, 439(1):300–317.

Lu, Y., Mo, H. J., Katz, N., and Weinberg, M. D. (2006). On the origin of cold dark matter halo density profiles. *MNRAS*, 368(4):1931–1940.

Ludlow, A. D. and Angulo, R. E. (2017). Einasto profiles and the dark matter power spectrum. *MNRAS*, 465(1):L84–L88.

Ludlow, A. D., Navarro, J. F., Angulo, R. E., Boylan-Kolchin, M., Springel, V., Frenk, C., and White, S. D. M. (2014). The mass-concentration-redshift relation of cold dark matter haloes. *MNRAS*, 441(1):378–388.

Ma, C.-P. and Fry, J. N. (2000). What Does It Take to Stabilize Gravitational Clustering? *Apjl*, 538(2):L107–L111.

MacLeod, C. L., Jones, R., Agol, E., and Kochanek, C. S. (2013). Detection of Substructure in the Gravitationally Lensed Quasar MG0414+0534 Using Mid-infrared and Radio VLBI Observations. *Apj*, 773(1):35.

Mandelbaum, R., van de Ven, G., and Keeton, C. R. (2009). Galaxy density profiles and shapes - II. Selection biases in strong lensing surveys. *MNRAS*, 398(2):635–657.

Mandic, V., Bird, S., and Cholis, I. (2016). Stochastic Gravitational-Wave Background due to Primordial Binary Black Hole Mergers. *PRL*, 117(20):201102.

Mao, S. and Schneider, P. (1998). Evidence for substructure in lens galaxies? *MNRAS*, 295(3):587–594.

Marinacci, F., Vogelsberger, M., Pakmor, R., Torrey, P., Springel, V., Hernquist, L., Nelson, D., Weinberger, R., Pillepich, A., Naiman, J., and Genel, S. (2018). First results from the IllustrisTNG simulations: radio haloes and magnetic fields. *MNRAS*, 480(4):5113–5139.

Meneghetti, M., Davoli, G., Bergamini, P., Rosati, P., Natarajan, P., Giocoli, C., Caminha, G. B., Metcalf, R. B., Rasia, E., Borgani, S., Calura, F., Grillo, C., Mercurio, A., and Vanzella, E. (2020). An excess of small-scale gravitational lenses observed in galaxy clusters. *Science*, 369(6509):1347–1351.

Metcalf, R. B. (2005). The Importance of Intergalactic Structure to Gravitationally Lensed Quasars. *Apj*, 629(2):673–679.

Metcalf, R. B. and Amara, A. (2012). Small-scale structures of dark matter and flux anomalies in quasar gravitational lenses. *MNRAS*, 419(4):3414–3425.

Metcalf, R. B. and Madau, P. (2001). Compound Gravitational Lensing as a Probe of Dark Matter Substructure within Galaxy Halos. *ApjLet*, 563(1):9–20.

Minor, Q., Gad-Nasr, S., Kaplinghat, M., and Vegetti, S. (2021a). An unexpected high concentration for the dark substructure in the gravitational lens SDSSJ0946+1006. *MNRAS*, 507(2):1662–1683.

Minor, Q., Kaplinghat, M., Chan, T. H., and Simon, E. (2021b). Inferring the concentration of dark matter subhaloes perturbing strongly lensed images. *MNRAS*, 507(1):1202–1215.

Minor, Q. E., Kaplinghat, M., and Li, N. (2017). A Robust Mass Estimator for Dark Matter Subhalo Perturbations in Strong Gravitational Lenses. *Apj*, 845(2):118.

Mo, H., van den Bosch, F. C., and White, S. (2010). *Galaxy Formation and Evolution*.

Moore, B., Ghigna, S., Governato, F., Lake, G., Quinn, T., Stadel, J., and Tozzi, P. (1999). Dark Matter Substructure within Galactic Halos. *ApjL*, 524(1):L19–L22.

More, S., Diemer, B., and Kravtsov, A. V. (2015). The Splashback Radius as a Physical Halo Boundary and the Growth of Halo Mass. *Apj*, 810(1):36.

Morgan, N. D., Caldwell, J. A. R., Schechter, P. L., Dressler, A., Egami, E., and Rix, H.-W. (2004). WFI J2026-4536 and WFI J2033-4723: Two New Quadruple Gravitational Lenses. *Apj*, 127(5):2617–2630.

Moustakas, L. A. and Metcalf, R. B. (2003). Detecting dark matter substructure spectroscopically in strong gravitational lenses. *MNRAS*, 339(3):607–615.

Muñoz-Cuartas, J. C., Macciò, A. V., Gottlöber, S., and Dutton, A. A. (2011). The redshift evolution of Λ cold dark matter halo parameters: concentration, spin and shape. *MNRAS*, 411(1):584–594.

Müller-Sánchez, F., Prieto, M. A., Hicks, E. K. S., Vives-Arias, H., Davies, R. I., Malkan, M., Tacconi, L. J., and Genzel, R. (2011). Outflows from Active Galactic Nuclei: Kinematics of the Narrow-line and Coronal-line Regions in Seyfert Galaxies. *Apj*, 739(2):69.

Nadler, E. O., Birrer, S., Gilman, D., Wechsler, R. H., Du, X., Benson, A., Nierenberg, A. M., and Treu, T. (2021). Dark Matter Constraints from a Unified Analysis of Strong Gravitational Lenses and Milky Way Satellite Galaxies. *arXiv e-prints*, page arXiv:2101.07810.

Naiman, J. P., Pillepich, A., Springel, V., Ramirez-Ruiz, E., Torrey, P., Vogelsberger, M., Pakmor, R., Nelson, D., Marinacci, F., Hernquist, L., Weinberger, R., and Genel, S. (2018). First results from the IllustrisTNG simulations: a tale of two elements - chemical evolution of magnesium and europium. *MNRAS*, 477(1):1206–1224.

Navarro, J. F., Frenk, C. S., and White, S. D. M. (1996). The Structure of Cold Dark Matter Halos. *Apj*, 462:563.

Navarro, J. F., Frenk, C. S., and White, S. D. M. (1997). A Universal Density Profile from Hierarchical Clustering. *Apj*, 490(2):493–508.

Navarro, J. F., Hayashi, E., Power, C., Jenkins, A. R., Frenk, C. S., White, S. D. M., Springel, V., Stadel, J., and Quinn, T. R. (2004). The inner structure of ΛCDM haloes - III. Universality and asymptotic slopes. *MNRAS*, 349(3):1039–1051.

Navarro, J. F., Ludlow, A., Springel, V., Wang, J., Vogelsberger, M., White, S. D. M., Jenkins, A., Frenk, C. S., and Helmi, A. (2010). The diversity and similarity of simulated cold dark matter haloes. *MNRAS*, 402(1):21–34.

Nelson, D., Pillepich, A., Springel, V., Weinberger, R., Hernquist, L., Pakmor, R., Genel, S., Torrey, P., Vogelsberger, M., Kauffmann, G., Marinacci, F., and Naiman, J. (2018). First results from the IllustrisTNG simulations: the galaxy colour bimodality. *MNRAS*, 475(1):624–647.

Neto, A. F., Gao, L., Bett, P., Cole, S., Navarro, J. F., Frenk, C. S., White, S. D. M., Springel, V., and Jenkins, A. (2007). The statistics of Λ CDM halo concentrations. *MNRAS*, 381(4):1450–1462.

Nierenberg, A. M., Gilman, D., Treu, T., Brammer, G., Birrer, S., Moustakas, L., Agnello, A., Anguita, T., Fassnacht, C. D., Motta, V., Peter, A. H. G., and Sluse, D. (2020). Double dark matter vision: twice the number of compact-source lenses with narrow-line lensing and the WFC3 grism. *MNRAS*, 492(4):5314–5335.

Nierenberg, A. M., Treu, T., Brammer, G., Peter, A. H. G., Fassnacht, C. D., Keeton, C. R., Kochanek, C. S., Schmidt, K. B., Sluse, D., and Wright, S. A. (2017). Probing dark matter substructure in the gravitational lens HE 0435-1223 with the WFC3 grism. *MNRAS*, 471(2):2224–2236.

Nierenberg, A. M., Treu, T., Wright, S. A., Fassnacht, C. D., and Auger, M. W. (2014). Detection of substructure with adaptive optics integral field spectroscopy of the gravitational lens B1422+231. *LettMNRAS*, 442(3):2434–2445.

Oñorbe, J., Garrison-Kimmel, S., Maller, A. H., Bullock, J. S., Rocha, M., and Hahn, O. (2014). How to zoom: bias, contamination and Lagrange volumes in multimass cosmological simulations. *MNRAS*, 437(2):1894–1908.

Okoli, C., Taylor, J. E., and Afshordi, N. (2018). Searching for dark matter annihilation from individual halos: uncertainties, scatter and signal-to-noise ratios. *JCAP*, 2018(8):019.

Oliphant, T. E. (2007). Python for Scientific Computing. *Computing in Science and Engineering*, 9(3):10–20.

Onions, J., Knebe, A., Pearce, F. R., Muldrew, S. I., Lux, H., Knollmann, S. R., Ascasibar, Y., Behroozi, P., Elahi, P., Han, J., Maciejewski, M., Merchán, M. E., Neyrinck, M., Ruiz, A. N., Sgró, M. A., Springel, V., and Tweed, D. (2012). Subhaloes going Notts: the subhalo-finder comparison project. *MNRAS*, 423(2):1200–1214.

Osato, K., Nishimichi, T., Oguri, M., Takada, M., and Okumura, T. (2018). Strong orientation dependence of surface mass density profiles of dark haloes at large scales. *MNRAS*, 477(2):2141–2153.

Paz, D. J., Lambas, D. G., Padilla, N., and Merchán, M. (2006). Shapes of clusters and groups of galaxies: comparison of model predictions with observations. *MNRAS*, 366(4):1503–1510.

Peebles, P. J. E. (1980). *The large-scale structure of the universe*.

Pillepich, A., Nelson, D., Hernquist, L., Springel, V., Pakmor, R., Torrey, P., Weinberger, R., Genel, S., Naiman, J. P., Marinacci, F., and Vogelsberger, M. (2018). First results from the IllustrisTNG simulations: the stellar mass content of groups and clusters of galaxies. *MNRAS*, 475(1):648–675.

Planck Collaboration, Ade, P. A. R., Aghanim, N., Arnaud, M., Ashdown, M., Aumont, J., Baccigalupi, C., Banday, A. J., Barreiro, R. B., Bartlett, J. G., and et al. (2016a). Planck 2015 results. XIII. Cosmological parameters. *AAP*, 594:A13.

Planck Collaboration, Ade, P. A. R., Aghanim, N., Arnaud, M., Ashdown, M., Aumont, J., Baccigalupi, C., Banday, A. J., Barreiro, R. B., Bartlett, J. G., and et al. (2016b). Planck 2015 results. XIII. Cosmological parameters. *AAP*, 594:A13.

Power, C., Navarro, J. F., Jenkins, A., Frenk, C. S., White, S. D. M., Springel, V., Stadel, J., and Quinn, T. (2003). The inner structure of ΛCDM haloes - I. A numerical convergence study. *MNRAS*, 338(1):14–34.

Prada, F., Klypin, A. A., Cuesta, A. J., Betancort-Rijo, J. E., and Primack, J. (2012). Halo concentrations in the standard Λ cold dark matter cosmology. *MNRASas*, 423(4):3018–3030.

Press, W. H. and Schechter, P. (1974). Formation of Galaxies and Clusters of Galaxies by Self-Similar Gravitational Condensation. *Apj*, 187:425–438.

Retana-Montenegro, E., van Hese, E., Gentile, G., Baes, M., and Frutos-Alfaro, F. (2012). Analytical properties of Einasto dark matter haloes. *AAP*, 540:A70.

Richings, J., Frenk, C., Jenkins, A., Robertson, A., and Schaller, M. (2021). A high-resolution cosmological simulation of a strong gravitational lens. *MNRAS*, 501(3):4657–4668.

Rocha, M., Peter, A. H. G., Bullock, J. S., Kaplinghat, M., Garrison-Kimmel, S., Oñorbe, J., and Moustakas, L. A. (2013). Cosmological simulations with self-interacting dark matter - I. Constant-density cores and substructure. *MNRAS*, 430(1):81–104.

Sánchez, A. G., Baugh, C. M., Percival, W. J., Peacock, J. A., Padilla, N. D., Cole, S., Frenk, C. S., and Norberg, P. (2006). Cosmological parameters from cosmic microwave background measurements and the final 2dF Galaxy Redshift Survey power spectrum. *MNRAS*, 366(1):189–207.

Sánchez-Conde, M. A. and Prada, F. (2014). The flattening of the concentration-mass relation towards low halo masses and its implications for the annihilation signal boost. *MNRAS*, 442(3):2271–2277.

Sawala, T., Frenk, C. S., Fattahi, A., Navarro, J. F., Theuns, T., Bower, R. G., Crain, R. A., Furlong, M., Jenkins, A., Schaller, M., and Schaye, J. (2016). The chosen few: the low-mass haloes that host faint galaxies. *MNRASL*, 456(1):85–97.

Schaye, J., Crain, R. A., Bower, R. G., Furlong, M., Schaller, M., Theuns, T., Dalla Vecchia, C., Frenk, C. S., McCarthy, I. G., Helly, J. C., Jenkins, A., Rosas-Guevara, Y. M., White, S. D. M., Baes, M., Booth, C. M., Camps, P., Navarro, J. F., Qu, Y., Rahmati, A., Sawala, T., Thomas, P. A., and Trayford, J. (2015). The EAGLE project: simulating the evolution and assembly of galaxies and their environments. *MNRAS*, 446(1):521–554.

Schneider, A., Smith, R. E., Macciò, A. V., and Moore, B. (2012). Non-linear evolution of cosmological structures in warm dark matter models. *MNRAS*, 424(1):684–698.

Schneider, A., Smith, R. E., and Reed, D. (2013). Halo mass function and the free streaming scale. *MNRAS*, 433(2):1573–1587.

Schneider, P., Ehlers, J., and Falco, E. E. (1992). *Gravitational Lenses*.

Seljak, U. (2000). Analytic model for galaxy and dark matter clustering. *MNRAS*, 318(1):203–213.

Sersic, J. L. (1968). *Atlas de Galaxias Australes*.

Sheth, R. K. and Tormen, G. (1999). Large-scale bias and the peak background split. *MNRAS*, 308(1):119–126.

Sheth, R. K. and Tormen, G. (2002). An excursion set model of hierarchical clustering: ellipsoidal collapse and the moving barrier. *MNRAS*, 329(1):61–75.

Smith, R. E., Peacock, J. A., Jenkins, A., White, S. D. M., Frenk, C. S., Pearce, F. R., Thomas, P. A., Efstathiou, G., and Couchman, H. M. P. (2003). Stable clustering, the halo model and non-linear cosmological power spectra. *MNRAS*, 341(4):1311–1332.

Springel, V. (2005). The cosmological simulation code GADGET-2. *MNRAS*, 364(4):1105–1134.

Springel, V. (2010). E pur si muove: Galilean-invariant cosmological hydrodynamical simulations on a moving mesh. *MNRAS*, 401(2):791–851.

Springel, V., Pakmor, R., Pillepich, A., Weinberger, R., Nelson, D., Hernquist, L., Vogelsberger, M., Genel, S., Torrey, P., Marinacci, F., and Naiman, J. (2018). First results from the IllustrisTNG simulations: matter and galaxy clustering. *MNRAS*, 475(1):676–698.

Springel, V., Wang, J., Vogelsberger, M., Ludlow, A., Jenkins, A., Helmi, A., Navarro, J. F., Frenk, C. S., and White, S. D. M. (2008). The Aquarius Project: the subhaloes of galactic haloes. *MNRAS*, 391(4):1685–1711.

Springel, V., White, S. D. M., Tormen, G., and Kauffmann, G. (2001). Populating a cluster of galaxies - I. Results at [formmu2]z=0. *MNRAS*, 328(3):726–750.

Tegmark, M., Blanton, M. R., Strauss, M. A., Hoyle, F., Schlegel, D., Scoccimarro, R., Vogeley, M. S., Weinberg, D. H., Zehavi, I., Berlind, A., Budavari, T., Connolly, A., Eisenstein, D. J., Finkbeiner, D., Frieman, J. A., Gunn, J. E., Hamilton, A. J. S., Hui, L., Jain, B., Johnston, D., Kent, S., Lin, H., Nakajima, R., Nichol, R. C., Ostriker, J. P., Pope, A., Scranton, R., Seljak, U., Sheth, R. K., Stebbins, A., Szalay, A. S., Szapudi, I., Verde, L., Xu, Y., Annis, J., Bahcall, N. A., Brinkmann, J., Burles, S., Castander, F. J., Csabai, I., Loveday, J., Doi, M., Fukugita, M., Gott, J. Richard, I., Hennessy, G., Hogg, D. W., Ivezić, Ž., Knapp, G. R., Lamb, D. Q., Lee, B. C., Lupton, R. H., McKay, T. A., Kunszt, P., Munn, J. A., O'Connell, L., Peoples, J., Pier, J. R., Richmond, M., Rockosi, C., Schneider, D. P., Stoughton, C., Tucker, D. L., Vand en Berk, D. E., Yanny, B., York, D. G., and SDSS Collaboration (2004). The Three-Dimensional Power Spectrum of Galaxies from the Sloan Digital Sky Survey. *Apj*, 606(2):702–740.

Tinker, J., Kravtsov, A. V., Klypin, A., Abazajian, K., Warren, M., Yepes, G., Gottlöber, S., and Holz, D. E. (2008). Toward a Halo Mass Function for Precision Cosmology: The Limits of Universality. *Apj*, 688(2):709–728.

Tisserand, P., Le Guillou, L., Afonso, C., Albert, J. N., Andersen, J., Ansari, R., Aubourg, É., Bareyre, P., Beaulieu, J. P., Charlot, X., Coutures, C., Ferlet, R., Fouqué, P., Glicenstein, J. F., Goldman, B., Gould, A., Graff, D., Gros, M., Haissinski, J., Hamadache, C., de Kat, J., Lasserre, T., Lesquoy, É., Loup, C., Magneville, C., Marquette, J. B., Maurice, É., Maury, A., Milsztajn, A., Moniez, M., Palanque-Delabrouille, N., Perdereau, O., Rahal, Y. R., Rich, J., Spiro, M., Vidal-Madjar, A., Vigroux, L., Zylberajch, S., and EROS-2 Collaboration (2007). Limits on the Macho content of the Galactic Halo from the EROS-2 Survey of the Magellanic Clouds. *AAP*, 469(2):387–404.

Tulin, S. and Yu, H.-B. (2018). Dark matter self-interactions and small scale structure. *Physical Reports*, 730:1–57.

van den Bosch, F. C., Jiang, F., Hearin, A., Campbell, D., Watson, D., and Padmanabhan, N. (2014). Coming of age in the dark sector: how dark matter haloes grow their gravitational potential wells. *MNRAS*, 445(2):1713–1730.

van der Walt, S., Colbert, S. C., and Varoquaux, G. (2011). The NumPy Array: A Structure for Efficient Numerical Computation. *Computing in Science and Engineering*, 13(2):22–30.

Vega-Ferrero, J., Yepes, G., and Gottlöber, S. (2017). On the shape of dark matter haloes from MultiDark Planck simulations. *MNRAS*, 467(3):3226–3238.

Vegetti, S. and Koopmans, L. V. E. (2009a). Bayesian strong gravitational-lens modelling on adaptive grids: objective detection of mass substructure in Galaxies. *MNRAS*, 392(3):945–963.

Vegetti, S. and Koopmans, L. V. E. (2009b). Statistics of mass substructure from strong gravitational lensing: quantifying the mass fraction and mass function. *MNRAS*, 400(3):1583–1592.

Vegetti, S., Koopmans, L. V. E., Auger, M. W., Treu, T., and Bolton, A. S. (2014). Inference of the cold dark matter substructure mass function at z = 0.2 using strong gravitational lenses. *MNRAS*, 442(3):2017–2035.

Vegetti, S., Koopmans, L. V. E., Bolton, A., Treu, T., and Gavazzi, R. (2010). Detection of a dark substructure through gravitational imaging. *MNRAS*, 408(4):1969–1981.

Vegetti, S., Lagattuta, D. J., McKean, J. P., Auger, M. W., Fassnacht, C. D., and Koopmans, L. V. E. (2012). Gravitational detection of a low-mass dark satellite galaxy at cosmological distance. *Nature*, 481(7381):341–343.

Vogelsberger, M., Genel, S., Springel, V., Torrey, P., Sijacki, D., Xu, D., Snyder, G., Bird, S., Nelson, D., and Hernquist, L. (2014a). Properties of galaxies reproduced by a hydrodynamic simulation. *Nature*, 509(7499):177–182.

Vogelsberger, M., Genel, S., Springel, V., Torrey, P., Sijacki, D., Xu, D., Snyder, G., Nelson, D., and Hernquist, L. (2014b). Introducing the Illustris Project: simulating the coevolution of dark and visible matter in the Universe. *MNRAS*, 444(2):1518–1547.

Vogelsberger, M., Marinacci, F., Torrey, P., and Puchwein, E. (2020). Cosmological simulations of galaxy formation. *Nature Reviews Physics*, 2(1):42–66.

Vuissoz, C., Courbin, F., Sluse, D., Meylan, G., Chantry, V., Eulaers, E., Morgan, C., Eyler, M. E., Kochanek, C. S., Coles, J., Saha, P., Magain, P., and Falco, E. E. (2008). COSMOGRAIL: the COSmological MOnitoring of GRAvItational Lenses. VII. Time delays and the Hubble constant from WFI J2033-4723. *AAP*, 488(2):481–490.

Wang, J., Bose, S., Frenk, C. S., Gao, L., Jenkins, A., Springel, V., and White, S. D. M. (2020). Universal structure of dark matter haloes over a mass range of 20 orders of magnitude. *Nature*, 585(7823):39–42.

Wang, J. and White, S. D. M. (2009). Are mergers responsible for universal halo properties? *MNRAS*, 396(2):709–717.

Warren, M. S., Quinn, P. J., Salmon, J. K., and Zurek, W. H. (1992). Dark Halos Formed via Dissipationless Collapse. I. Shapes and Alignment of Angular Momentum. *Apj*, 399:405.

Wechsler, R. H., Bullock, J. S., Primack, J. R., Kravtsov, A. V., and Dekel, A. (2002). Concentrations of Dark Halos from Their Assembly Histories. *Apj*, 568(1):52–70.

Weinberg, D. H., Mortonson, M. J., Eisenstein, D. J., Hirata, C., Riess, A. G., and Rozo, E. (2013). Observational probes of cosmic acceleration. *Physical Reports*, 530(2):87–255.

Weinberger, R., Springel, V., Hernquist, L., Pillepich, A., Marinacci, F., Pakmor, R., Nelson, D., Genel, S., Vogelsberger, M., Naiman, J., and Torrey, P. (2017). Simulating galaxy formation with black hole driven thermal and kinetic feedback. *MNRAS*, 465(3):3291–3308.

Weiner, C., Serjeant, S., and Sedgwick, C. (2020). Predictions for Strong-lens Detections with the Nancy Grace Roman Space Telescope. *Research Notes of the American Astronomical Society*, 4(10):190.

Wetzel, A. R., Hopkins, P. F., Kim, J.-h., Faucher-Giguère, C.-A., Kereš, D., and Quataert, E. (2016). Reconciling Dwarf Galaxies with ΛCDM Cosmology: Simulating a Realistic Population of Satellites around a Milky Way-mass Galaxy. *Apjl*, 827(2):L23.

White, S. D. M. and Rees, M. J. (1978). Core condensation in heavy halos: a two-stage theory for galaxy formation and clustering. *MNRAS*, 183:341–358.

Wright, C. O. and Brainerd, T. G. (2000). Gravitational Lensing by NFW Halos. *Apj*, 534(1):34–40.

Xu, D., Sluse, D., Gao, L., Wang, J., Frenk, C., Mao, S., Schneider, P., and Springel, V. (2015). How well can cold dark matter substructures account for the observed radio flux-ratio anomalies. *MNRAS*, 447(4):3189–3206.

Xu, D. D., Mao, S., Cooper, A. P., Gao, L., Frenk, C. S., Angulo, R. E., and Helly, J. (2012). On the effects of line-of-sight structures on lensing flux-ratio anomalies in a ΛCDM universe. *MNRAS*, 421(3):2553–2567.

Xu, D. D., Mao, S., Wang, J., Springel, V., Gao, L., White, S. D. M., Frenk, C. S., Jenkins, A., Li, G., and Navarro, J. F. (2009). Effects of dark matter substructures on gravitational lensing: results from the Aquarius simulations. *MNRAS*, 398(3):1235–1253.

Yoon, J. H., Johnston, K. V., and Hogg, D. W. (2011). Clumpy Streams from Clumpy Halos: Detecting Missing Satellites with Cold Stellar Structures. *Apj*, 731(1):58.

Zavala, J. and Frenk, C. S. (2019). Dark Matter Haloes and Subhaloes. *Galaxies*, 7(4):81.

Zentner, A. R., Kravtsov, A. V., Gnedin, O. Y., and Klypin, A. A. (2005). The Anisotropic Distribution of Galactic Satellites. *Apj*, 629(1):219–232.

Zhao, D. H., Jing, Y. P., Mo, H. J., and Börner, G. (2003). Mass and Redshift Dependence of Dark Halo Structure. *ApjL*, 597(1):L9–L12.

Zhao, D. H., Jing, Y. P., Mo, H. J., and Börner, G. (2009). Accurate Universal Models for the Mass Accretion Histories and Concentrations of Dark Matter Halos. *Apj*, 707(1):354–369.

Zhu, Q., Marinacci, F., Maji, M., Li, Y., Springel, V., and Hernquist, L. (2016). Baryonic impact on the dark matter distribution in Milky Way-sized galaxies and their satellites. *MNRAS*, 458(2):1559–1580.